UCRL-18902

cy. 2

IN-BEAM PROTON-GAMMA RAY COINCIDENCE STUDIES USING A LARGE COAXIAL Ge(Li) DETECTOR

Joel M. Moss
(Ph.D. Thesis)

April 1969

AEC Contract No. W-7405-eng-48

TWO-WEEK LOAN COPY

This is a Library Circulating Copy
which may be borrowed for two weeks.
For a personal retention copy, call
Tech. Info. Division, Ext. 5545

LAWRENCE RADIATION LABORATORY
UNIVERSITY of CALIFORNIA BERKELEY

UCRL-18902

DISCLAIMER

This document was prepared as an account of work sponsored by the United States Government. While this document is believed to contain correct information, neither the United States Government nor any agency thereof, nor the Regents of the University of California, nor any of their employees, makes any warranty, express or implied, or assumes any legal responsibility for the accuracy, completeness, or usefulness of any information, apparatus, product, or process disclosed, or represents that its use would not infringe privately owned rights. Reference herein to any specific commercial product, process, or service by its trade name, trademark, manufacturer, or otherwise, does not necessarily constitute or imply its endorsement, recommendation, or favoring by the United States Government or any agency thereof, or the Regents of the University of California. The views and opinions of authors expressed herein do not necessarily state or reflect those of the United States Government or any agency thereof or the Regents of the University of California.

IN-BEAM PROTON-GAMMA-RAY COINCIDENCE STUDIES USING A LARGE COAXIAL Ge(Li) DETECTOR

Contents

Abstract vii

I. Introduction 1

A. General 1

B. ^{54}Fe Spectroscopy 2

1. General 2

2. Angular Correlation Analysis 4

3. Lifetime Measurements 8

C. Spin-Flip Experiment 11

II. Experimental Equipment 17

A. Cyclotron and Beam Line 17

1. General 17

2. Beam Stability 18

B. Scattering Chamber. 20

1. General 20

2. Configuration for ^{54}Fe Spectroscopy 22

3. Configuration for Spin-Flip Experiment . . 22

C. Background and Shielding 24

1. Geometrical Definition of the Beam 24

2. Background from Scattering Chamber 24

3. Background from Faraday Cup 25

D. Particle Detectors 26

1. General 26

2. Annular Detector 26

3. Detectors for Spin-Flip Experiment 28

E. Germanium Detector 29

F. Electronics System 32

1. General 32

2. High-Rate Amplifier Systems 33

3. Fast Electronics 36

4. Data Storage and Logic 37

5. Subsidiary Systems 43

G. High Resolution System 44

H. Targets 44

III. Experimental Techniques 45

A. General 45

B. Analysis of the True-to-Chance Ratio 46

1. Evaluation of the Chance Rate 46

2. Factors Affecting the True-to-Chance Ratio 49

C. Detector and Electronics System 53

1. High-Rate Counting Systems 53

2. Fast Timing Characteristics of the Detectors 54

D. Coincidence Evaluation 59

1. Spectrum Summation 59

2. Chance Coincidence Evaluation 61

3. Pile-Up Rejection and Dead-Time Losses . . 62

IV. ^{54}Fe Spectroscopy: Experiment and Results 64

A. Excitation Function 64

B. Coincidence Experiment 64

C. Analysis 66

1. Angular Correlations 66

2. Doppler Shift Attenuation Method 73

3. Observed States 77

D. Results 81

1. Detailed Spectroscopic Information 81

2. Summary of Electromagnetic Transition Data 111

E. Conclusion 118

V. Spin-Flip: Experiment and Results 127

A. Data Collection 127

B. Data Reduction and Results 129

C. Analysis 135

1. Optical Model 135

2. Collective Model 148

3. Microscopic Model 152

D. Summary 162

Acknowledgments 164

Appendices 166

A. Derivation of the Correlation Function for Collinar Geometry 166

B. Attenuation Coefficients 176

References 180

IN-BEAM PROTON-GAMMA RAY COINCIDENCE STUDIES USING A LARGE COAXIAL Ge(Li) DETECTOR

Joel M. Moss*

Department of Chemistry and
Lawrence Radiation Laboratory
University of California
Berkeley, California 94720

April 1969

ABSTRACT

Two different applications were made of particle-gamma ray coincidence techniques: first, in the $^{54}Fe(p,p')^{54}Fe$ reaction at 10 MeV and then, in the reactions $^{54,56}Fe(p,p')^{54,56}Fe$ at 19.6 MeV. In both experiments a large coaxial Ge(Li) counter was used to detect the gamma rays.

In the $^{54}Fe(p,p')^{54}Fe$ reaction at 10 MeV, the angular correlation of gamma rays coincident with protons detected near 180° was measured. On the basis of this information, unambiguous spin assignments were made to the 3.345(3), 4.074(3), 4.579(2), 4.781(3), and 4.949(4) MeV states. Model-dependent assignments and spin limitations were made for several other states. The angular correlation analysis also yielded multipole mixing ratios for several transitions and branching ratios for the decay of all states of ^{54}Fe below 5 MeV. From an analysis of the observed Doppler shifts of the coincident gamma rays, mean lifetimes were derived for the 1.409, 2.959, 3.164, 3.836, 4.048, 4.074, 4.265, 4.287, 4.781, and 4.949 MeV states.

Coincident gamma rays perpendicular to the reaction plane, as a function of proton scattering angle, were observed in the reactions $^{54,56}Fe(p,p')^{54,56}Fe$ at 19.6 MeV. Analysis of these data yielded angular distributions of the spin-flip probability in the inelastic excitation of the first 2^+ states in both nuclei. The spin-flip probabilities were compared to the predictions of both the collective and microscopic models of inelastic proton scattering. Also included in the theoretical analysis were high precision differential cross section measurements made here, and inelastic asymmetry data from Saclay.[1]

I. INTRODUCTION

A. General

The study of coincidences between outgoing particles from a nuclear reaction and de-excitation gamma rays has several desirable features. These may be summarized as follows: 1) The spectra obtained are quite simple. For example, from the viewpoint of gamma spectra, one sees all of the transitions involved in the decay of the initial state or states to the ground state. The background from other reactions is eliminated to a large extent on the basis of timing criteria. 2) The residual nuclei produced are either aligned[2] or polarized, resulting in an anisotropic angular correlation of the de-excitation gamma rays. Studies of the particle-gamma ray angular correlation can yield useful information either on the excited nuclear states and subsequent gamma ray transitions or on the mechanism of the reaction producing the states. 3) In a reaction having a two-body final state, specification of the angle of emission of the observed particle uniquely defines the velocity vector of the recoiling residual nucleus. Then, if gamma decay occurs while the nucleus is moving, the transition energy will be Doppler shifted; the magnitude of the shift is determined by the recoil velocity and the angle of detection of the gamma ray with respect to the recoil direction. In certain cases (see Section I.B-3), such an observation may lead to the determination of the lifetime of the decaying state.

We report here on two different applications of particle gamma-ray coincidence techniques. The first was a spectroscopic study of the levels of ^{54}Fe, using the reaction ^{54}Fe(p,p')^{54}Fe at 10 MeV. This experiment utilized all three features of coincidence studies outlined previously.

Secondly, we have investigated the spin-flip probability in the reactions $^{54,56}Fe(p,p')^{54,56}Fe$ at 19.6 MeV, exciting the first 2^+ states in these nuclei. Here the problem of interest was one of reaction mechanism.

The two experiments, although having one target nucleus in common, yielded quite disparate types of information. We have not emphasized the rather meager overlap in the interpretation of each. Thus, the format of presentation is that of two distinct experiments having a great deal in common experimentally. The two experiments are introduced separately in the remainder of Section I. Then, in Sections II and III, a unified presentation of the experimental details is given--noting when necessary the modifications appropriate to each experiment. Finally, Sections IV and V give the analyses and interpretations for ^{54}Fe spectroscopy and spin-flip experiments, respectively.

B. ^{54}Fe Spectroscopy

1. General

In the simple shell model picture, ^{54}Fe is considered to have two $1f_{7/2}$ proton holes, coupled to zero, inside the ^{56}Ni doubly closed shell. The low-energy spectrum of ^{54}Fe, then, should consist of three states of the configuration $(f_{7/2})^{-2}_J$, where J can have the values 2, 4, and 6. A similar situation is encountered in ^{50}Ti, which has the proton configuration $(f_{7/2})^2_J$ outside the ^{48}Ca doubly closed shell. In reality the low-energy spectra of these two nuclei show striking differences. Titanium-50 conforms well to the $(f_{7/2})^2_J$ picture; it exhibits the expected 2^+, 4^+, 6^+ sequence and has no additional states below 4.16 MeV.

In contrast, ^{54}Fe, while having three excited states identifiable as $(f_{7/2})^{-2}_J$, also has several other states in the same energy region. Thus the situation is similar to that found in some of the lighter mass nuclei of the $f_{7/2}$ shell, where assumed $(f_{7/2})^n$ configurations do not accurately account for the observed low-energy spectra.[3] Of particular note is ^{42}Ca: here analogously to ^{54}Fe, one expects low lying states of $J^\pi = 2^+$, 4^+, and 6^+ from the $(f_{7/2})^2$ neutron configuration outside the ^{40}Ca doubly closed shell. It has been found, in this case, that deformed states intrude into the $(f_{7/2})^2_J$ neutron spectrum.[4] Calcium-42 has been extensively investigated both theoretically[4-7] and experimentally[8-10] and, as a result, a fairly satisfactory explanation of the additional states has emerged. On the other hand, the levels of ^{54}Fe are not well understood.

Experimentally ^{54}Fe is a rather difficult nucleus to investigate. It is not accessible to single nucleon transfer reactions. Furthermore, inelastic scattering experiments[11-15] have been hampered by the fact that many of the levels are quite closely spaced and hence are unresolvable. Indeed, even the reliable assignment of spins to the levels of ^{54}Fe has been rather difficult; in the (p,p'γ) angular correlation work of Thomas et al.,[16] several low-lying levels of ^{54}Fe could not be resolved and therefore could not be assigned spins. The purpose of this work, then, was the further elucidation of the character of the excited states in ^{54}Fe, with the hope that some insight might be gained into the larger problem of nuclear structure in the region of the ^{56}Ni doubly closed shell. To this objective we have used the (p,p'γ) angular

correlation method in the investigation; this technique was extended in the present work by the use of a large volume, high resolution Ge(Li) gamma detector. The information obtained on the levels of ^{54}Fe includes several new spin assignments, several excited state lifetimes, and information on the decay modes of all known levels below 5 MeV.

2. Angular Correlation Analysis

General. The application of angular correlation theory to the interpretation of coincidence data has been utilized as a powerful nuclear spectroscopic tool for many years. Among the more desirable features of the angular correlation method is the fact that the theory is exact. This does not imply that the analysis is always unambiguous, since some of the parameters of the correlation function may not be known. However, it does imply that the confidence levels of quantities derived from such an analysis (e.g., spins and multipole mixing ratios) can be directly related to the experimental errors.

The term "angular correlation" in the present usage implies a function which depends upon the coordinates of two or more nuclear radiations. Experimentally, a coincidence may not be required--for example, it is certainly appropriate to describe a resonance reaction in terms of the angular function which includes the coordinates of both incoming and outgoing particles. It is often useful to view the problem of correlation as one in which an ensemble of aligned nuclei is produced by an initial radiation (either by emission or absorption of particles or gamma rays) whose coordinates are fixed. The correlation function,

then, describes the emission of a second radiation. We will use the terms "angular correlation" and "angular distribution" interchangeably in describing the decay of aligned nuclei.

A very useful method for producing nuclear alignment is the bombardment of target nuclei with a high-energy particle beam. If the outgoing particles are not detected, the alignment of the residual nuclei is usually described by too many arbitrary parameters to allow unambiguous spin information to be derived from the angular distribution of gamma rays (this problem viewed as a correlation would require specification of the particle coordinates). This is true either in the case of a direct reaction or a compound nuclear reaction in which several overlapping resonant states are involved. As an example, the unknown parameters in the case of an aligned 4^+ are the populations of four substates[17] and the multipole mixing ratio. Singles gamma-ray angular distributions have yielded spectroscopic information in some cases involving reactions of the type (particle,xn), especially in the cases where heavy ions are used as the incoming projectiles. In these cases, arguments may be given which show that the alignment in high spin states greatly favors small m projections (z-axis in the beam direction).[18]

Studies of particle-gamma ray coincidences in a variety of geometrical configurations have yielded useful spectroscopic information. In the simple case of a particle detector at a fixed angle, a measurement of the angular distribution of gamma rays in the reaction plane is usually not sufficient to allow unambiguous spin assignments. It is necessary either to measure the out-of-plane correlation[19] or to use a

reaction model to provide arguments about the substate population. The latter method has been applied with some success; an example is the use of either plane wave or distorted wave stripping theory to predict substate population for the (d,pγ) reaction.[20]

Collinear Geometry. Litherland and Ferguson[21] have discussed two geometries for "in-beam" experiments where a study of coincident radiations can lead to unambiguous spectroscopic information. In Method I, the outgoing particle is not observed and the angular correlation between two cascade gamma rays is measured. This method has had comparatively limited application and will not be discussed further here. In Method II, the angular distribution of gamma rays in coincidence with particles scattered at 0° or at 180° is observed (collinear geometry); this procedure has become a standard tool for in-beam nuclear spectroscopy during the last five years and forms the basis for the present study of the levels of ^{54}Fe.

The great utility of collinear geometry resides in the fact that the substate population of the nuclei produced is quite restricted. It is shown in Ref. 21 and in Appendix A that, when the outgoing particles are detected along the z-axis, the maximum possible angular momentum projection of the residual nucleus is given by:

$$m_{max} = S_i + S_o + J_N$$

where S_i and S_o are the spins of the incoming and outgoing particles, respectively, and J_N is the initial nuclear spin. In the present case of the (p,p') reaction on spin zero nuclei, only the m = 0, ±1 substates

of the residual nucleus may be populated. The axial symmetry of the system implies equal population of the $m = \pm 1$ substates ($P(1) = P(-1)$). Therefore, the unknown parameters of the angular correlation are $P(0)$, $P(1)$, and δ, where δ is the multipole mixing ratio of the gamma transition.

The general angular correlation function for the reaction may be written:[22]

$$W(\theta_\gamma) = \sum_k A_k P_k(\cos\theta_\gamma) = \sum_k \rho_k(a)\, F_k(ab)\, P_k(\cos\theta_\gamma) \qquad \text{(I-1)}$$

The derivation of this expression is given in Appendix A; we mention here only that the measured parameters A_0, A_2, and A_4 [23] may be directly related to the unknowns previously discussed. Thus, in favorable situations, the spins and multipole mixing ratios may be unambiguously determined from a theoretical fit to the angular correlation. It should be noted that the mixing ratio, δ, enters in the A's quadratically and may, therefore, produce two solutions.

The angular distribution of a gamma ray, which has been preceded by an unobserved gamma ray, may also lead to useful spin information. As an example, for a transition $a \xrightarrow{\gamma_1} b \xrightarrow{\gamma_2} c$, the correlation function is:

$$W(\theta_{\gamma_2}) = \sum_k \rho_k(a)\, U_k(ab)\, F_k(bc)\, P_k(\cos\theta_{\gamma_2}) \qquad \text{(I-2)}$$

The re-alignment of state b is described by the coefficients $U_k(ab)$.[22]

In the foregoing discussion, it was assumed that the outgoing particle is detected along the z-axis. In practice, of course, the

particle detector has a finite size. The effect of this is to allow a contribution to the angular correlation from the $m_{max} + 1$ substate ($m = 2$ for (p,p') on $J = 0$ targets). The contribution should be quite small if the detectors are close to the z-axis[21] (see Section IV.C-1). In the present experiment, an annular particle detector was used to detect protons scattered from 168° to 172°.

Application of Ge(Li) Detectors. In previous experiments employing collinear geometry, NaI(Tl) detectors have been used to detect the de-excitation gamma rays. These detectors are characterized by high detection efficiency and rather poor energy resolution. The best resolution obtainable in such an experiment is that of the particle counter and is usually limited to ∿50 keV. Thus the usefulness of this powerful spectroscopic technique has been restricted to levels which could be cleanly resolved in the particle spectrum.

A major goal of this work was the extension of the spectroscopic method, previously described, by the use of a high-resolution Ge(Li) counter for detection of the gamma rays. This extension was made possible by two recent advances in gamma-ray counting technology. These are: 1) The advent of large-volume germanium detectors, and 2) the development of a high count-rate amplifier system. The implications of these advances are discussed in detail in Section III.

3. Lifetime Measurements

The measurement of lifetimes of nuclear states can yield valuable nuclear structure information. In the case of gamma decay, the operator

for the transition is presumably well known and thus the lifetime, or equivalently the reduced transition probability, provides a sensitive test of the structure of the states involved. (This equivalence implies that the multipole mixing and branching ratios are known.)

An important class of methods for measuring nuclear lifetimes utilizes the Doppler shift observed when gamma decay occurs from a nucleus' traveling with a velocity, v. The Doppler shift, ΔE_o, is then:

$$\Delta E_o = E - E_o = E_o(v_o/c) \cos \theta \qquad \text{(I-3)}$$

where E_o and E are the unshifted and shifted gamma-ray energies, respectively, and θ is the angle of observation of the gamma ray with respect to the velocity vector, v_o, of the recoiling nucleus. The particular technique utilized in the present experiment was the Doppler Shift Attenuation Method (DSAM); various modifications of the DSAM have been described by several authors.[24-27]

The optimum condition for the application of the DSAM is that the average recoil velocity, v_o, be a well defined and calculable quantity. This implies a coincidence with the detected particle from the reaction producing the recoil. Fortunately, the geometry which has been used in past experiments of this type is identical to that required for the present angular correlation experiment. With this geometry, gamma rays are detected only from nuclei which recoil in the beam direction (to a good approximation), and thus have the maximum possible recoil energy. The velocity vector, v_o, may be calculated simply from the kinematics of the reaction.

To utilize the Doppler shift information, the lifetime (τ) of the state must be of the order of the stopping time (τ_s) of the recoil nucleus in the target. In such a case, the maximum Doppler shift as given by Eq. (I-3) will be attenuated by a factor $F(\tau)$, where:

$$F(\tau) = \frac{\Delta E_{obs}}{\Delta E_o} = 1/\tau \int_0^\infty \frac{v(t)}{v_o} e^{-t/\tau} dt$$

In order to obtain $v(t)$, we use the relation $dE/dx = mv \frac{dv}{dx} = m \frac{dv}{dt}$, where dE/dx is the stopping power of the recoil ion in the stopping medium. Since there is little experimental data available on stopping powers of low energy ($v/c < 137$) heavy ions, it is necessary to rely on theoretical estimates of dE/dx. For the present analysis, the theory of Lindhard, Scharf, and Schiøtt[28] (LSS) was used. LSS, using the Thomas-Fermi model of the atom, consider separately the electronic and the nuclear energy loss. The former arises from collisions in which atomic electrons are excited (including ionization) and is characterized by a dE/dx which is proportional to v. The latter, which is important at low velocities, arises from elastic collisions with the ions in the target. LSS have derived a universal curve for the nuclear stopping power.

Because nuclear collisions are capable of producing large-angle scattering of the recoils, it is important to include this effect in the analysis. An expression for the mean scattering angle, $\cos \phi(t)$, has been derived by Blaugrund,[25] using the theory of LSS. Thus, given the total dE/dx over the entire velocity range of interest, it is possible to calculate for comparison to experiment:

$$F(\tau) = 1/\tau \int_0^\infty \frac{v(t)}{v_o} \cos \phi(t)\, e^{-t/\tau}\, dt \quad .$$

C. Spin-Flip Experiment

Spin dependent forces in the inelastic scattering of nucleons are not well understood, even in a phenomenological sense. Cross sections $\sigma(\theta)$, asymmetries $A(\theta)$, polarizations $P(\theta)$,[29] and spin-flip probabilities $S(\theta)$, are sensitive to these forces in different ways. They can be written:

$$\sigma(\theta) = \sigma_{++} + \sigma_{--} + \sigma_{+-} + \sigma_{-+}$$
$$A(\theta)\sigma(\theta) = \sigma_{++} + \sigma_{+-} - \sigma_{-+} - \sigma_{--}$$
$$P(\theta)\sigma(\theta) = \sigma_{++} + \sigma_{-+} - \sigma_{+-} - \sigma_{--}$$
$$S(\theta)\sigma(\theta) = \sigma_{+-} + \sigma_{-+}$$

where σ_{+-}, e.g., is the differential cross section for scattering from an initial state with incident nucleon spin projection +1/2 to a final state with outgoing nucleon spin projection -1/2 on the z-axis. All these quantities involve independent combinations of the σ_{ij} components.

Until recently, the bulk of inelastic scattering data has been cross section measurements. With the advent of high-intensity polarized proton beams, however, it has become possible to obtain high precision asymmetry data. An initial survey of asymmetries in inelastic proton scattering has been made by the Saclay group,[30] which studied the excitation of low-lying states in several isotopes of Ti, Cr, Fe, Ni, and Cu with 18.6-MeV protons. More recently, high precision asymmetries have been measured at Saclay for states in ^{54,56}Fe at 19.6 MeV[1] and for

several isotopes in the Zr and Mg regions at 20.2 MeV.[31] Among the more striking features of these data are the differences between the asymmetries for 2^+ states which are primarily proton configurations and those which include neutron configurations. An example of each, respectively, is the first 2^+ state in ^{54}Fe and ^{56}Fe.

With the objective of better understanding the differences between the ^{54}Fe and ^{56}Fe 2_1^+ asymmetries and the role that spin-dependent forces play in producing them, we have measured the spin-flip probabilities for the first 2^+ states in these two nuclei at 19.6-MeV incident proton energy. In a separate experiment at the same energy, $\sigma(\theta)$ has also been measured for these states.

The relative spin-flip probability for ^{54}Fe has been measured before at 11 MeV;[32] several isotopes of Cr, Ni, and Zn have also been measured at that energy.[33] The University of Washington group has obtained absolute probabilities for ^{12}C and ^{24}Mg,[33] and they have made an extensive series of measurements on the Ni isotopes at energies from 10-15 MeV.[35] A measurement on ^{58}Ni at 20 MeV has recently been reported.[36] The experiments at energies below 20 MeV do reveal rather large differences among the nuclei studied, but their interpretation in terms of a direct reaction model seems questionable, since compound nuclear contributions are apparently important. This is particularly true of the ^{54}Fe work where, on the basis of the evidence given in Section IV.A, the compound nucleus mechanism is dominant in the region of 11 MeV.

In the present experiment, the spin-flip probabilities were measured using the $(p,p'\gamma)$ angular correlation technique first explored by

Schmidt et al.;[34] all previous $S(\theta)$ experiments have also used this method. When the gamma detector is placed along the normal to the reaction plane defined by the incoming and outgoing protons (this defines the z-axis), coincident protons and gamma rays of the appropriate energy define excitation of only the $m = \pm 1$ magnetic substates of the 2^+ state; this is apparent from Fig. 1. To relate the substates of the residual nucleus to those of the incident and outgoing particles, we use Bohr's Theorem,[37] which states:

$$P_i \, e^{i\pi M_i} = P_f \, e^{i\pi M_f} \qquad \text{with} \quad M = m_p + m_N$$

where P is the parity and M is the sum of nuclear (m_N) and nucleon (m_p) spin projections for the initial (i) and final (f) states. Now in the excitation $0^+(p,p')2^+$, we have

$$e^{i\pi m_{ip}} = e^{i\pi(m_{fp}+m_{fN})}$$

and with the previous coincidence criterion, we obtain:

$$m_{ip} - m_{fp} = \pm 1$$

Thus, for such a process, spin flip must have occurred.

<u>Spin Flip: Collective Model</u>. To date, all analyses of spin-flip data have been in terms of the collective (i.e., macroscopic) model of the reaction. In the simplest form of this model, there is no explicit spin dependent term in the interaction, and the spin flip is due entirely to the presence of the spin-orbit ($\underset{\sim}{l} \cdot \underset{\sim}{s}$) term of the optical model potential. That there can be spin flip in such a case may be understood from

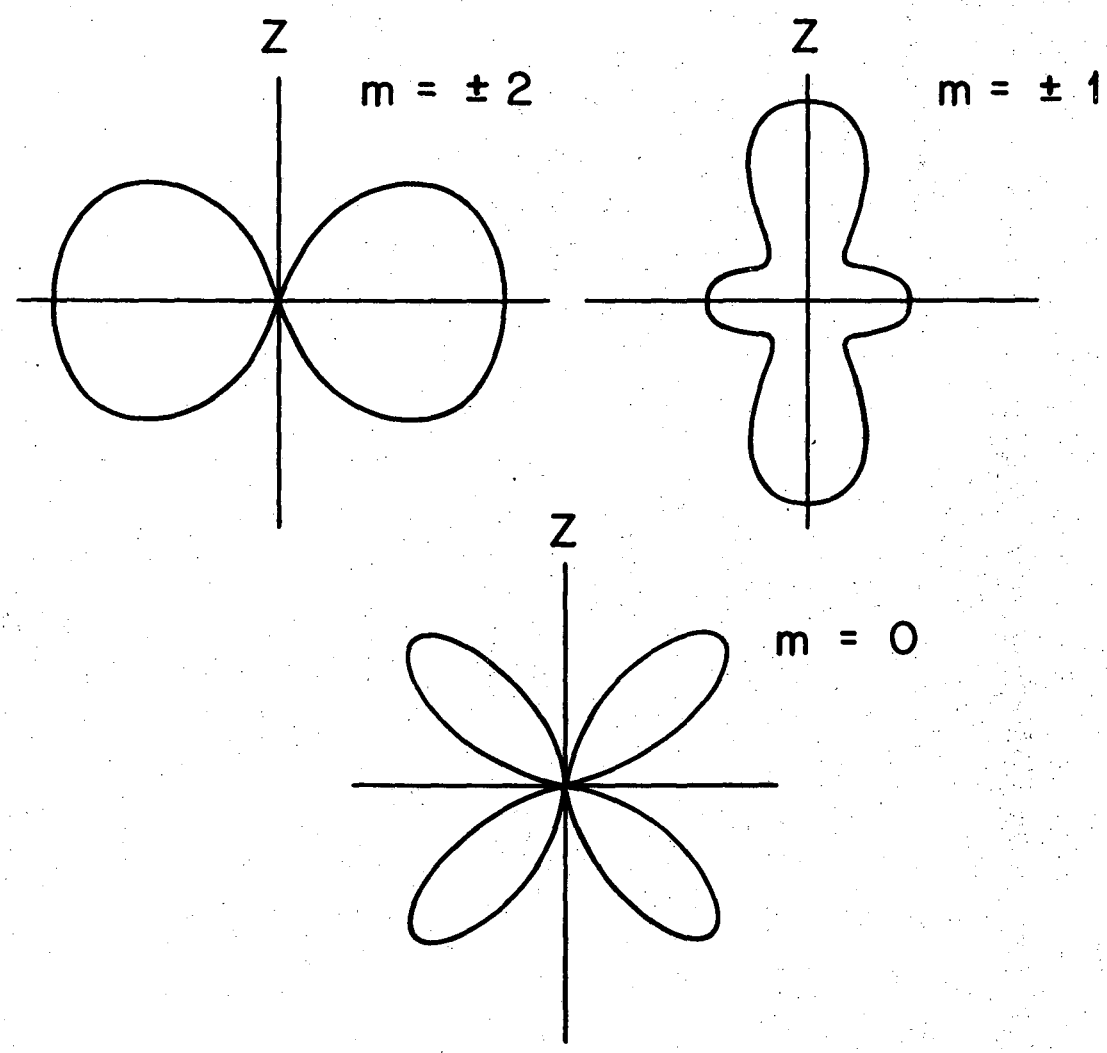

XBL693-2239

Fig. 1. Radiation intensity patterns for an aligned quadrupole.

the fact that, in the presence of a spin-orbit potential, m_s(proton) is not a good quantum number and hence need not be conserved. In more sophisticated calculations,[30,38,39] the spin-orbit potential is also included explicitly in the interaction producing the excitation; there are still only $\Sigma = 0$ (i.e., no spin transfer) excitations in this model.

A collective model analysis of the present spin-flip and cross section data and the 19.6-MeV asymmetry data from Saclay is given in Section V.C-2.

Spin Flip: Microscopic Model. A potentially more informative description of the inelastic scattering process is in terms of a microscopic model of the nucleus.[40] In such a model, the nuclear particles undergoing excitation are explicitly described in terms of initial and final nuclear wave functions; the operator inducing the transition is usually written as:

$$V(\underset{\sim}{r}_{ij}) = -(V_o + V_1 \underset{\sim}{\sigma}_i \cdot \underset{\sim}{\sigma}_j)\, g(\underset{\sim}{r}_{ij})$$

where $\underset{\sim}{\sigma}$ is the spin operator, respectively, for the projectile (i) and nucleons in the target (j), and $\underset{\sim}{r}_{ij}$ is the vector distance between them. The V_o term causes $\Sigma = 0$ transitions and gives spin-flip contributions only through the spin-orbit potential, while the V_1 term induces $\Sigma = 1$ transitions and thus can produce additional spin flip. In general, the σ_{+-}, etc., terms will have interfering contributions from $\Sigma = 0$ and $\Sigma = 1$ terms.

For an explanation of the differences between the ^{54}Fe and ^{56}Fe asymmetries, a microscopic view of the reaction is most logical. It offers the possibility of producing such differences via differences in

nuclear wave functions, whereas the collective model predicts similar inelastic quantities for neighboring nuclei. Section V.C-3 is devoted to a microscopic analysis of the present data.

II. EXPERIMENTAL

A. Cyclotron and External Beam Line

1. General

Proton beams of 10 and 19.6 MeV were provided by the Berkeley 88" variable-energy cyclotron. The cyclotron and external beam facilities are shown in Fig. 2. The extracted beam was focused by a quadruple doublet and bent 56° by a switching magnet onto a set of vertical and horizontal slits (analyzing slits) in the cyclotron vault area. The beam then passed through an eight foot concrete and iron shielding wall, was bent another 12° and finally was focused to a 0.06" wide and 0.12" high spot at the target area.

The horizontal divergence of the beam was limited by the "x" collimator located near the point of extraction. Subsequently, only the analyzing slits were used to define the beam. These were typically set at 0.040", which resulted in a beam resolution of about 0.08%.

After passing through the scattering chamber, the beam was stopped in a Faraday cup, which was split vertically along the center line. Charge from each half of the Faraday cup was separately integrated and used to monitor both the beam current and alignment. Equal currents were maintained in each half to insure a constant position of the beam spot. Periodically, the beam position on the target was checked with the aid of a thin scintillating target and a closed-circuit T.V. system.

The Faraday cup was initially aligned with the known optic axis (which passed through the target position) with the aid of a transit. During a run, slight adjustments in the beam axis could be made, using

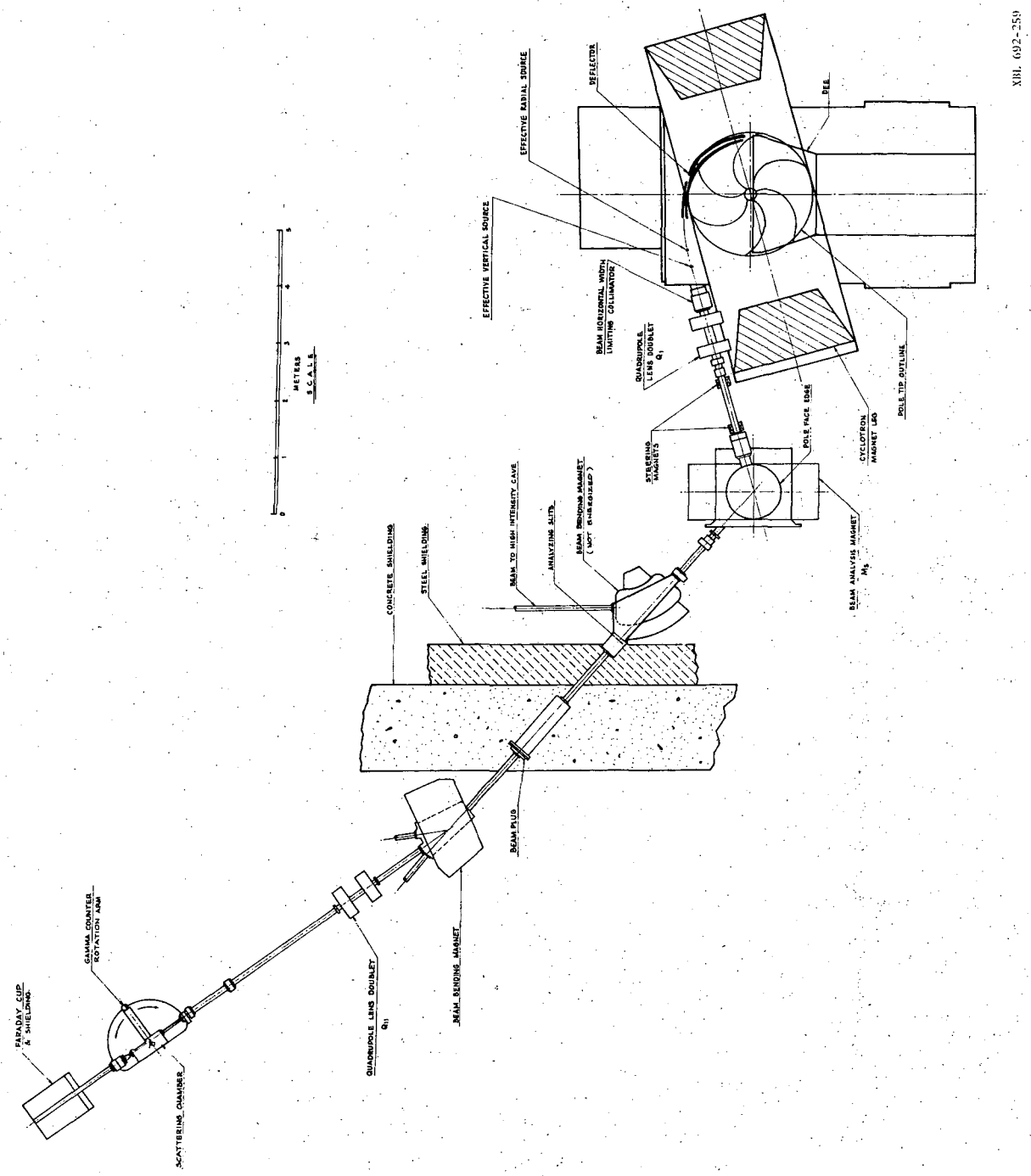

Fig. 2. Layout of the 88" cyclotron and the Cave-1 gamma scattering chamber.

the horizontal and vertical motion of the analyzing slits and two small steering magnets located near the cyclotron. The beam could thus be required to go through the target position and to be centered in the Faraday cup.

2. Beam Stability

In one of the experiments (^{54}Fe spectroscopy), it was essential to have no beam-energy variations during the run. The variations could arise from either a change in the switching magnet current or a change in cyclotron parameters. The former was easily controlled by means of an NMR probe monitor. Control of the latter, however, was more difficult. Changes in a number of parameters, e.g. deflector voltage and dee voltage, are capable of producing small (∿0.2%) energy shifts. In addition, the resonance condition could change due to shifts in the oscillator frequency and magnetic field. Fortunately, the reasonably low-intensity beams of low-energy particles (20 MeV H_2^+) allowed the deflector to be operated quite stably at low voltage and with very little heating. It sufficed, therefore, to maintain the frequency constant within ∿200 cycles, in order to insure stability with respect to both intensity and energy. Occasional minor adjustments were made in the main coil current to regain the resonance condition. Dee voltage variations were not large enough to cause difficulties. During 72 hours of operation, the beam energy was stable to within 10 keV (limit of our sensitivity). The beam energy was monitored by observing the position of the elastic peak in a fixed position monitor detector spectrum.

B. Scattering Chamber

1. General

The scattering chamber (see Fig. 3) was a rectangular box about 24" long, 8" wide, and 8" deep. In addition to a removable lid, the two sides parallel to the beam could be removed and replaced with other inserts, depending on the desired experimental configuration. The side nearer the beam included a 2" high slot running the entire length of the side, which was covered with a 0.003" tantalum foil. This allowed the gamma detector, which was outside the chamber, to view the target position with very little absorption of gamma rays. The opposite side contained four circular ports. They were covered with 1) a lucite window, 2) a plate containing coaxial cable connectors, 3) an attachment for a liquid nitrogen dewar, and 4) a plate containing two rotatable shafts (only for the spin-flip experiment).

Two concentric rotatable shafts were located in the bottom of the chamber; coaxial with them was a movable arm, located outside the chamber, on which the gamma detector was placed. This arm could be rotated 180° on one side of the beam line. The target position was chosen to coincide with the intersection of the beam axis and the axis of rotation of the shafts. Prior to each run, both particle and gamma detectors were precisely aligned with respect to the beam axis with transits. This was possible for the gamma detector because its position inside the housing was well determined during the mounting operation.

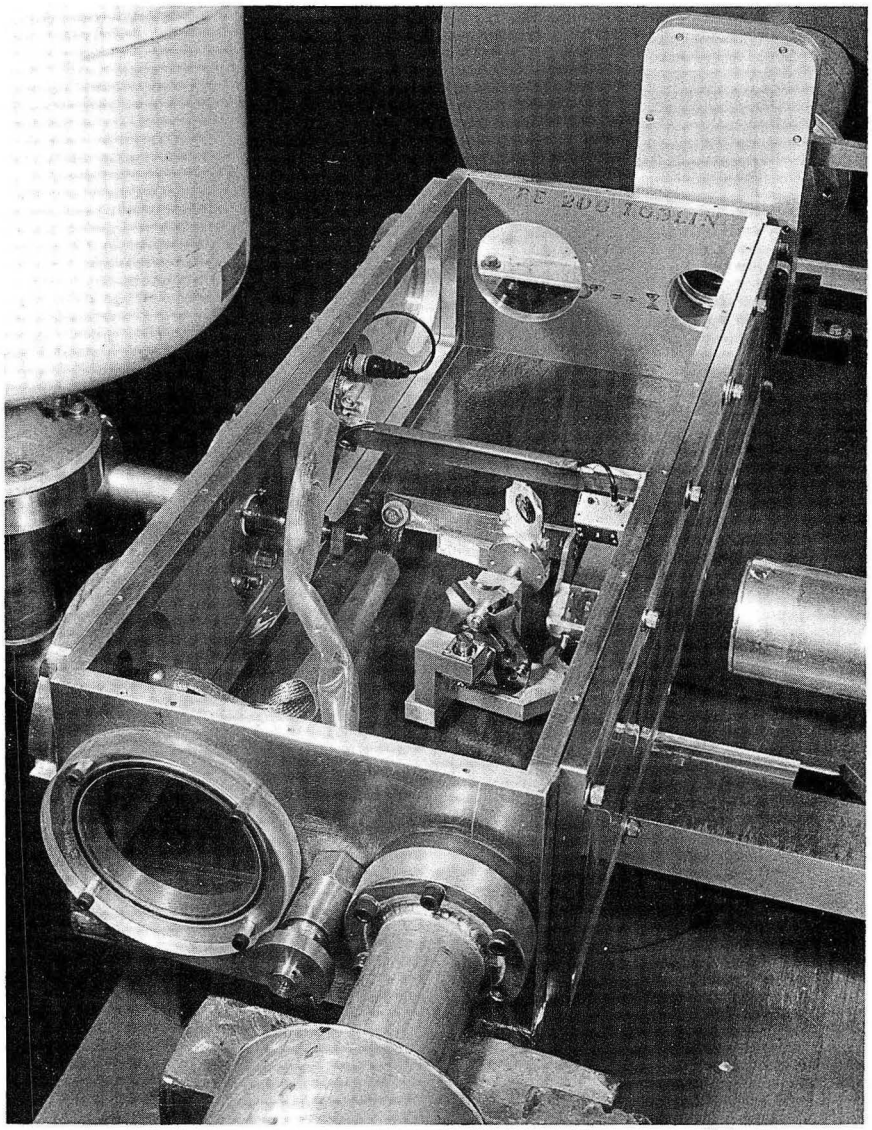

XBB 6810-6270

Fig. 3. Close-up view of the scattering chamber in the configuration for the spin-flip experiment. The gamma detector (extreme right) views the target position through a 0.003" Ta foil.

2. Configuration for ^{54}Fe Spectroscopy

Figure 4 shows the geometry used for the ^{54}Fe spectroscopy run. The indented side allowed access to small angles for the gamma detector.[41] When the counter was placed 4 22/32" from the target, it could be rotated in to 25°. This distance represented a compromise between detection efficiency and fullness of angular range.

The slot covered with tantalum foil ran the entire length of the chamber wall so that the beam passed close to the foil and not to the aluminum wall. This was quite important since copious amounts of background radiation are produced when even a low-energy proton beam strikes aluminum, because of the low Coulomb barrier. The foil-to-beam distance could be set at 0.25", 0.5", or 0.75" by insertion of spacer rings between the chamber frame and the insert; background considerations indicated at least a 0.5" separation was required.

The annular counter assembly (described in Section II.D-2) was fixed on an arm which, during the experiment, positioned the counter at 180°; the counter arm could be rotated to smaller angles during the initial beam focusing.

3. Configuration for Spin-Flip Experiment

The geometry required for the spin-flip experiment was that the gamma detector be perpendicular to the plane defined by the particle detector and the beam axis. To accomplish this, a plate containing two concentric shafts was attached to the side of the chamber opposite the gamma detector (see Fig. 3). Two particle detectors, mounted on arms

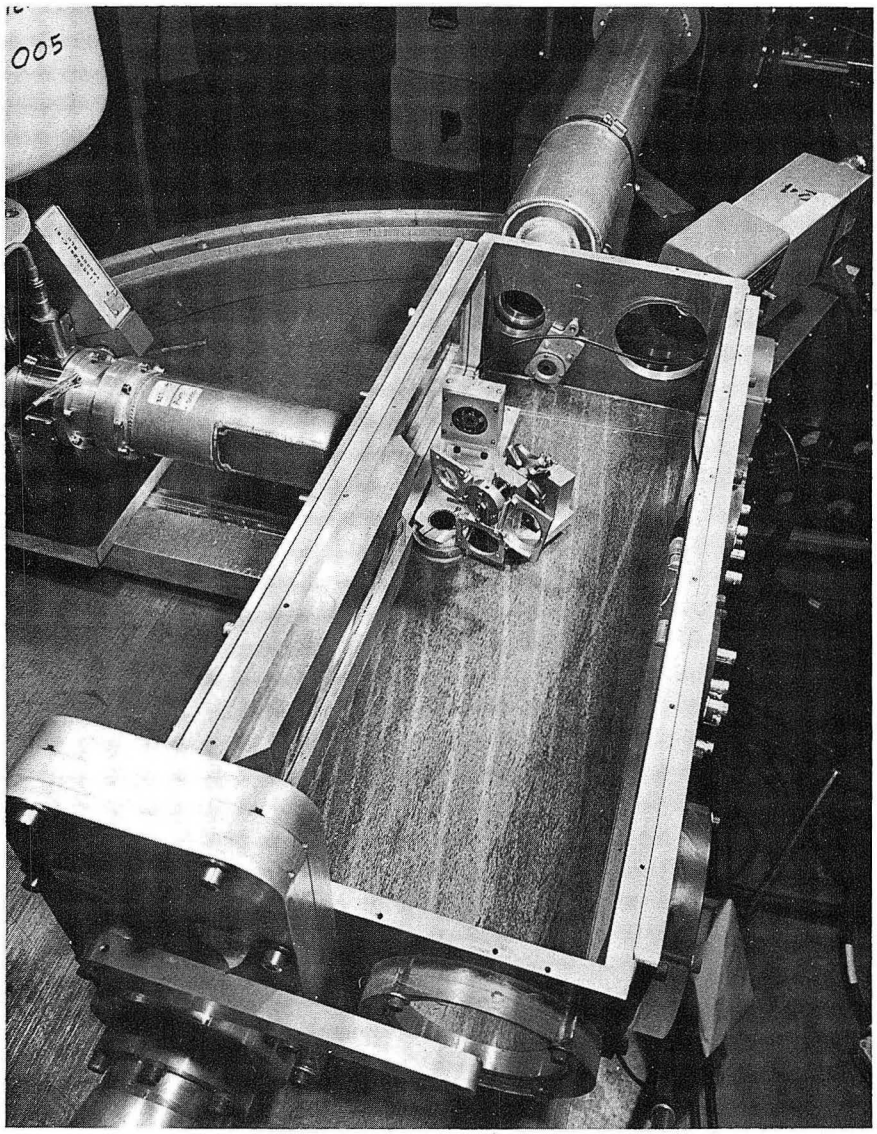

XBB 693-1912

Fig. 4. Close-up view of the scattering chamber in the configuration for the ^{54}Fe spectroscopy experiment. Shown inside the chamber are the target holder and rotation mechanism and the annular counter.

connected to the shafts, could be rotated independently in the vertical plane, thus defining it as the reaction plane. Space limitation inside the chamber required that one detector be used at forward angles and the other at backward angles, with the range 90° to 95° accessible to both, for the purpose of checking efficiencies.

C. Background and Shielding

1. Geometrical Definition of the Beam

Among the most universal problems in gamma-ray experiments is background radiation; its reduction for in-beam experiments is particularly difficult. The following procedures have been found to apply to beams of 10 and 20 MeV protons.

The external beam system discussed previously had the important feature that the beam could be analyzed and defined geometrically at a large and well shielded distance from the target area. In addition, H_2^+ beams were used so that slit scattered particles which became fully ionized would be deflected out of the beam by the second bending magnet. Thus, a very clean beam could be obtained in the scattering chamber.

2. Background from Components in the Scattering Chamber

During the ^{54}Fe spectroscopy experiment it was, of course, necessary for the beam to pass through a 6 mm diameter hole in the annular counter. In addition, after going through the target, the beam passed within about 0.5" of the side of the chamber (see Fig.). By using only tantalum, which has a coulomb barrier of 15.5 MeV, the background

from the beam "halo" striking these critical areas could be reduced to tolerable levels for a 10-MeV proton beam. The difference in background levels with and without the annular detector at 180° was barely detectable (<5%).

3. Background from the Faraday Cup

The beam was stopped by a graphite Faraday cup located 84 inches from the target. Carbon is commonly chosen as the stopping material because of its (^{12}C) low neutron yield under charged particle bombardment.

The Faraday cup was shielded by a 30" by 36" aluminum cylinder, lined with a cadmium sheet and filled with boreated paraffin. The end of the shield near the scattering chamber was faced with 4" of lead. This arrangement was very effective in reducing the background due to both neutrons and gamma rays. It had the additional advantage of protecting the Ge(Li) detector from high neutron fluxes which cause radiation damage.

A further reduction of Faraday cup radiation may be obtained by fast timing criteria. If the gamma rays from the target and from the Faraday cup are separated by more than the fast coincidence resolving time, such background can be eliminated (see Section III.B-1).

In both experiments, it was necessary to protect the gamma detector from charged particles passing through to the tantalum foil. To meet this requirement and also to further reduce the low-energy background (<511 keV) in preference to the generally higher energy gamma rays from the target, the detector was covered with a 0.040" tantalum

plate. The overall background rates in both experiments were usually around 5% of the total count rates during runs.

Finally, the background in the annular counter due to particles backscattered from the Faraday cup was quite small and confined to energies below 3 MeV. In both experiments, thin aliminum foils covered the particle detectors to stop knock-on electrons from the target.

D. Particle Detectors

1. General

The protons were detected with Si(Li) counters fabricated at the LRL counter laboratory. Considerable experience at this laboratory and elsewhere has shown that substantial improvement in both energy resolution and rise time can be obtained by cooling Si(Li) detectors to the range from -20°C to -40°C. To implement this advantage into the present system, a liquid nitrogen dewar was attached to the chamber, though thermally insulated from it. Approximately 8" to 12" copper braids were used to connect the cold finger of the dewar to the detector housings. This resulted in a temperature of about -35°C for the detectors, which remained quite constant (±1°); thermocouples were used to monitor the temperature.

2. Annular Detector

An annular Si(Li) detector 1.5 mm thick was used to detect protons from the reaction $^{54}Fe(p,p')^{54}Fe$ at 10 MeV. Figure 5 shows the counter holder. The collimators were made of 0.040" tantalum. The inside

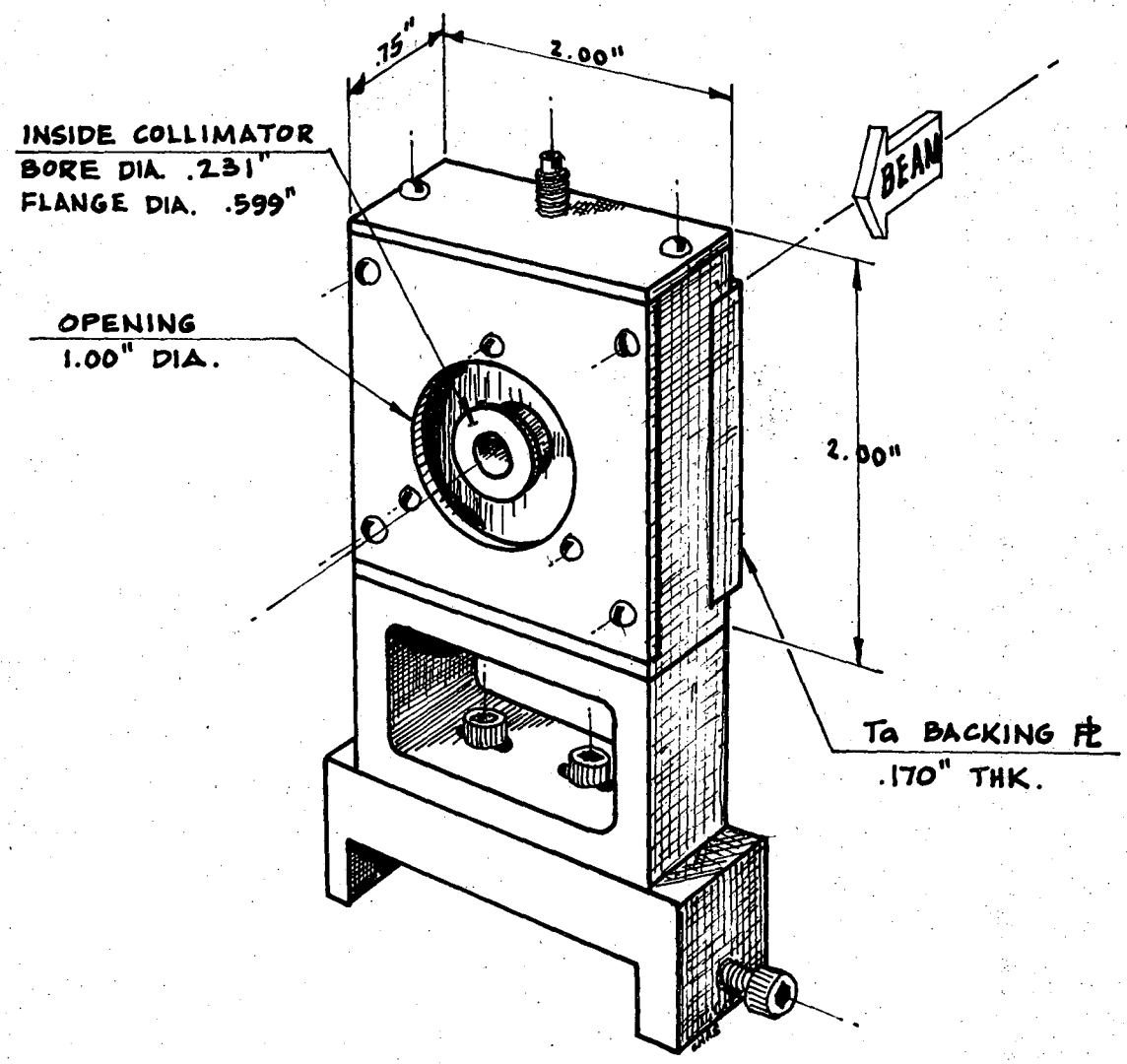

XBL 693-356

Fig. 5. The annular Si(Li) particle counter and counter holder.

collimator was held in place by a tube (0.020" surface thickness) which was precisely milled to fit snugly into the hole in the back protective plate. The tube was essential for protecting the counter from radiation (electron and x-ray) produced by beam particles striking the backing plate. The detector was held in place against the aluminum ground electrode by a wire clip, which also served as the other electrode.

When the counter was positioned 2.5" from the target, it covered the angular range from 168.4° to 172.8° and subtended a solid angle of 0.078 sr.[42]

At the operating temperature of -35°C and with a bias of 250 V, this detector gave 40-keV resolution on a pulser. The best resolution observed with 10-MeV protons was 55 keV.

During the run, an additional cooled Si(Li) detector was placed at 140° for monitoring purposes.

2. Particle Detectors for the Spin-Flip Experiment

For the $^{54,56}Fe(p,p')^{54,56}Fe$ reactions at 19.6 MeV, two 3 mm Si(Li) detectors were used to stop the protons. Counter collimators of dimension 0.118" by 0.239" were located 1.2" from the center of the target. The dimensions correspond to solid angles of 0.025 sr and acceptance angles of 11.4° in the scattering plane and 5.6° perpendicular to it. The gamma detector subtended a half angle of 8° (the relation of these angles to substate population is described later).

At the operating temperature of -35°C and at a bias of 400 V, these detectors gave pulser resolutions of 25 keV. Under running

conditions, however, resolutions of 150 to 200 keV were observed; the width was almost entirely due to kinematic broadening.

E. Germanium Detector

The gamma rays were detected by a lithium-drifted germanium counter of 40-cm^3 intrinsic volume. It was made from a cylindrical pulled crystal by drifting lithium radially toward the center and also axially from one end, to a depth of 13 mm; thus, it was a close-ended coaxial ("5-sided" coaxial) detector. Fabrication was done at the LRL counter laboratory by R. H. Pehl and co-workers. The detector holder and cooling apparatus were of the standard type and have been described elsewhere.[43]

The measured capacity of the detector was 34 pF.[44] At the usual operating bias of 2000 V, it was capable of 2.4-keV resolution for ^{60}Co (1.33-MeV gamma). Figure 6 shows such a spectrum. The full energy (FE) peak height to Compton edge height is ∿20 to 1. When the detector was placed in the experimental cave, the best resolution obtained was 4 keV. The increase was believed to be due to pick-up, primarily from the cyclotron oscillator. During both experiments, the observed resolution was ∿6 keV for 1-MeV gamma rays; the additional increase was due to high counting rates (∿20 kc/sec) and small gain drifts encountered during runs. No gain shifts as large as 1 keV were observed. The timing properties of the detector are discussed in Section III.C-2.

Figure 7 shows the absolute (i.e., without the solid angle factor) efficiency of the 40-cm^3 counter. Calibration was accomplished using a

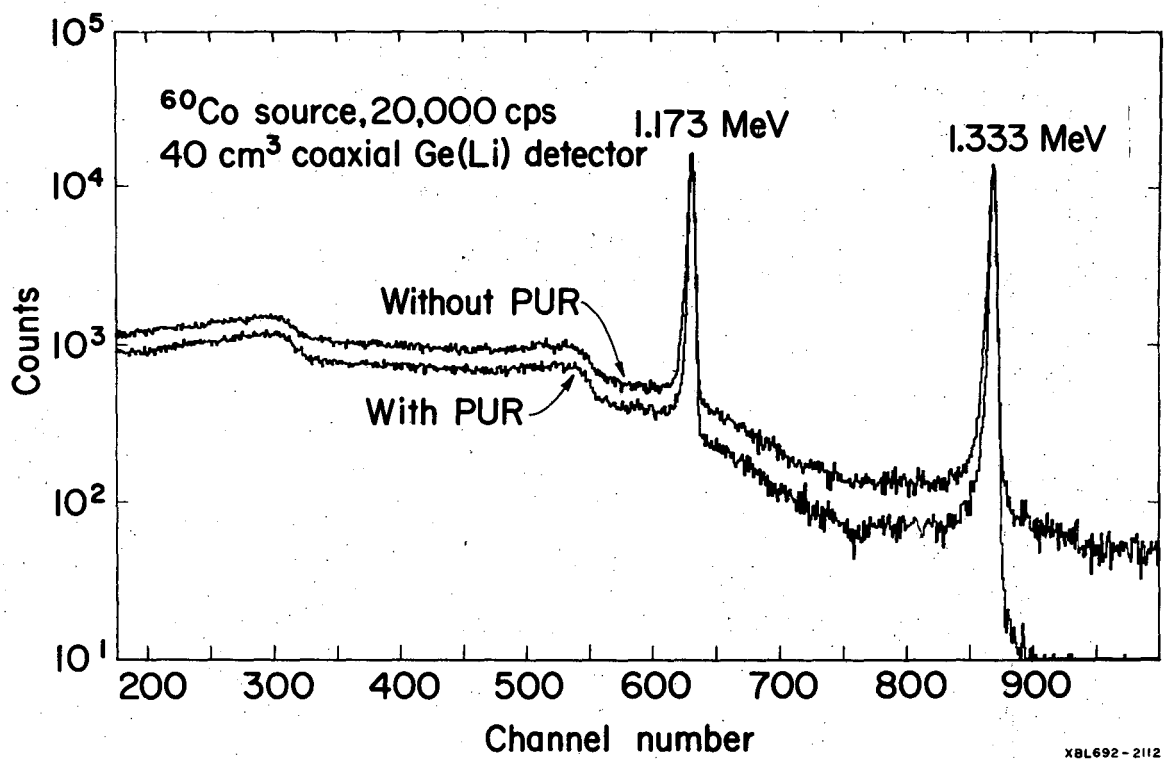

Fig. 6. Gamma-ray spectrum of a ^{60}Co source using the high-rate amplifier system with and without pile-up rejector.

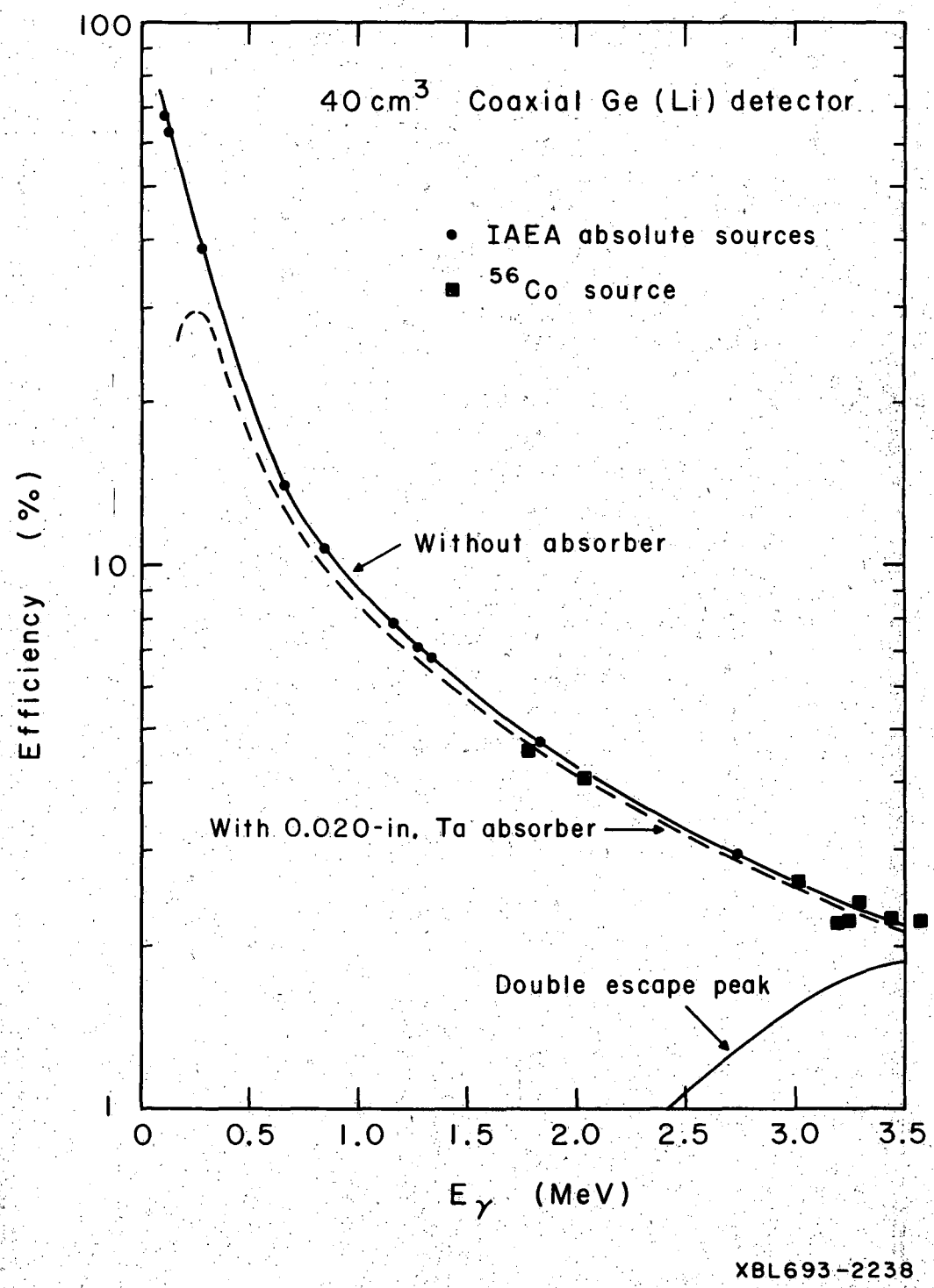

Fig. 7. Absolute efficiency curves for the 40-cm^3 coaxial Ge(Li) detector.

set of IEAE[45] calibrated sources; the relative efficiency above 1.8 MeV was obtained using a ^{56}Co source.

Definition of the source-to-counter distance presents an ambiguity for gamma rays. For example, low energy gamma rays interact almost entirely in the front of the counter, while for very high energy gamma rays, the center of the counter is the average interaction position. We chose to define the counter position as the point at which the ^{65}Zn (1.115-MeV gamma) exhibited a $1/r^2$ intensity-distance relation. During the ^{54}Fe spectroscopy run, the gamma detector was positioned at 4 22/32" from the target; the half-angle subtended was 8 degrees. The position was identical during the spin-flip run, although some data were taken at distances larger and smaller by a factor of $\sqrt{2}$.

F. Electronics System

1. General

The basic requirements to establish the coincidence of two or more nuclear radiations are simple. It is necessary to determine that the events (two or more) have occurred within a small time interval, Δt, and to allow storage of the energy signals only when this criterion is met. Random (i.e., uncorrelated) events can also occur within the required finite resolving time, Δt, and it is usually necessary to correct the measured spectrum for them. Determination of the chance rate and optimization of the true-to-chance ratio is discussed in Section III.B.

In practice, of course, the tools required are much more complicated than indicated previously. A common procedure is to initially

separate the functions of timing and energy analysis; the coordination of the two is then accomplished at some later stage of the system with logic and gating circuitry. This convenient separation has been adopted for the discussion of the present system.

We have considered individually the gamma, particle, and time (fast timing) systems; the discussion has included the generation of a logic signal for each which fed a triple-slow coincidence. The latter opened the linear gates in each of the systems. Finally, we have considered individually the additional logic requirements for the ^{54}Fe spectroscopy and spin-flip experiments.

2. High-Rate Amplifier Systems

The central features of the electronic systems for both experiments were the high-rate amplifier systems designed by Goulding, Landis, and Pehl.[46] Each system consisted of a high-rate pre-amplifier, a high-rate linear amplifier employing pole-zero cancellation, a pile-up rejector, and a linear gate. Figure 8(a) shows the system in the configuration used for the present experiments. Minor modifications of the systems which were designed for gamma-ray counting, were made for use with Si(Li) particle detectors. The details of the high-rate system are discussed in Ref. 46; only the features required for a unified presentation of the present electronics system have been given here.

Ge(Li) Detector System. Pulses from the Ge(Li) detector were fed into the charge sensitive FET pre-amplifier shown schematically in Fig. 8(b). Note that the detector is DC coupled to the FET; this

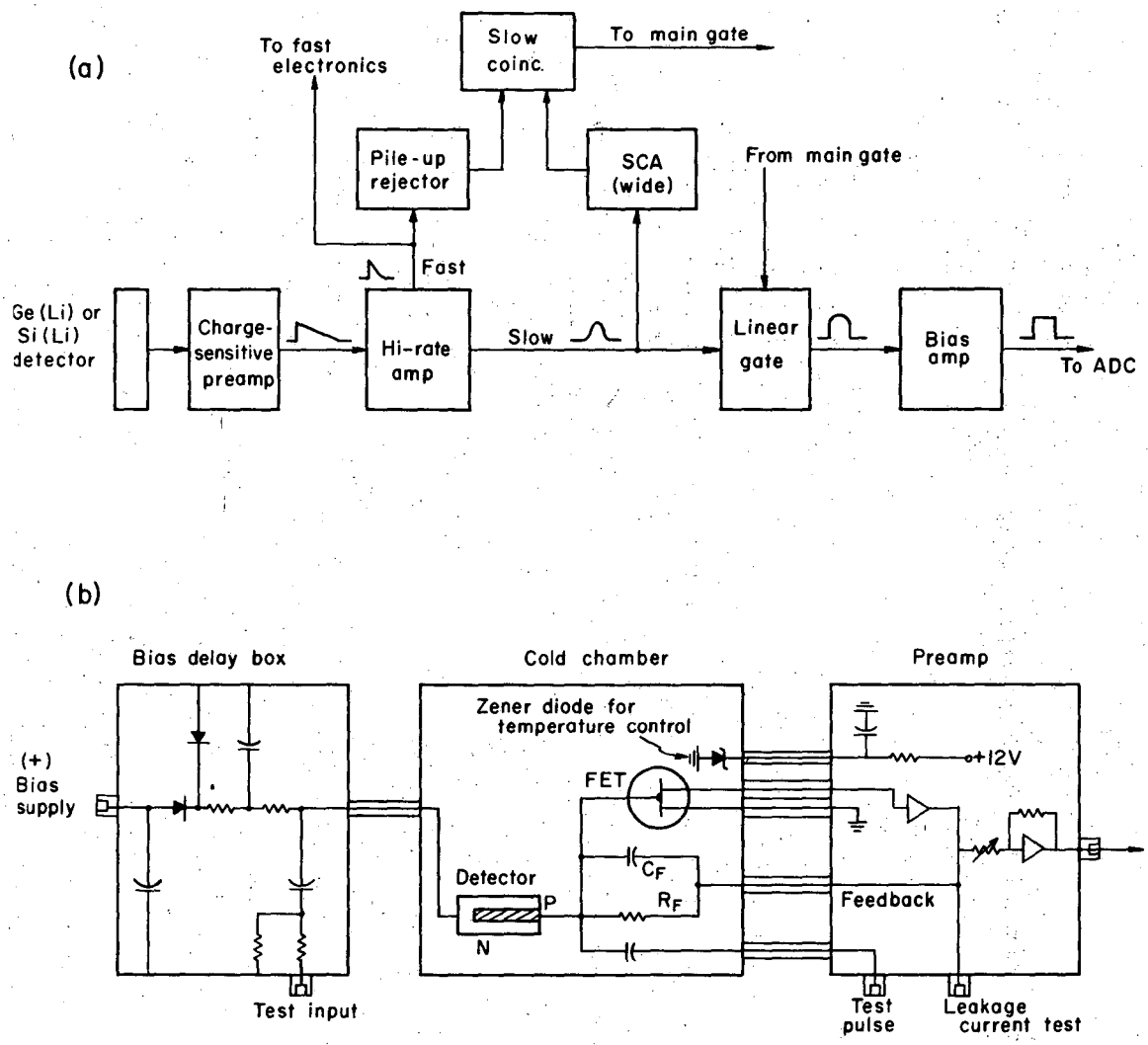

Fig. 8. (a) Simplified block diagram showing the components of the high-rate amplifier system as applied in the present experiments.
(b) Details of the bias-delay box and preamplifier components for the Ge(Li) detector.

allowed use of the feedback voltage to monitor the detector leakage current. It also had the advantages of reducing capacities to ground between the detector and FET as compared to AC coupling, and elimination of FET damage due to high voltage transients from the bias supply. The FET, which was located in the detector cold chamber, was maintained at the optimum operating temperature by a high thermal resistance Zener diode.

The pre-amplifier output was fed directly into the high-rate linear amplifier. The pole-zero cancellation feature of the amplifier was adjusted to correct for the baseline undershoot which resulted from the pre-amplifier feedback time constant R_fC_f. This gave a considerable improvement in resolution at high count rates compared with conventional amplifier systems.

The linear amplifier produced two outputs. For fast timing and pile-up rejection, there was a fast output (50 nsec rise time) which had bypassed the integrating stage of the system and therefore contained the fast rise components of the signals. For purposes of energy analysis the pulse was integrated by a fixed time constant "active integrator"; the output (subsequently referred to as the slow output) was almost Gaussian in shape, with a rise time of 3 μsec. This pulse shape, in addition to optimizing the signal-to-noise ratio, had the advantage of minimum sensitivity to the rise-time variations encountered in thick detectors.

The pile-up rejector (PUR) performed logic on the linear amplifier fast output to insure that 1) a given pulse was not preceded by another, within the inspection time (variable from 5 to 25 μsec), and

2) no pulse had occurred during the rise time and for 0.5 μsec after the peak of a given pulse. If these criteria were met, the PUR produced a valid output signal, which was combined in a slow coincidence with the output of an SCA (set to encompass the full energy range of interest) to provide an input for the main gate. The slow output of the linear amplifier was gated by the main gate and then fed into a biased amplifier.

Si(Li) Detector Systems. The high-rate systems, modified for use with Si(Li) particle detectors,[47] were quite similar to the gamma detector systems. We note the following essential differences. 1) The detector was AC coupled to the FET input stage of a charge sensitive pre-amplifier (not the one shown in Fig. 8(b)). 2) The amplifier integration time constant was changed to produce an output pulse whose FWHM was 1 μsec. 3) The pile-up rejection inspect time was variable from 3 to 10 μsec.

The particle input to the main gate was generated in the same manner as for the gamma system. Likewise, the gated energy signal was fed into a biased amplifier.

3. Fast Electronics

The fast outputs from the high-rate amplifiers for both particle and gamma systems were fed into gain-10 DC-coupled amplifiers (1 nsec rise time) and then into fast discriminators. The amplification was needed to bring the signals into the required voltage range for an optimum setting of the discriminators. The discriminator levels were set

as closely as possible to the noise level in order to obtain good time resolution.

The outputs of the particle and gamma discriminators provided, respectively, the start and stop pulses for a time-to-amplitude converter (TAC). The TAC produced an output whose pulse height was proportional to the time difference between the start and stop pulses. The use of a TAC allowed the detailed time correlation between events (true and chance) to be obtained; thus it was much more versatile than the "fast coincidence" circuit which has been commonly used. Figure 9 shows the TAC spectrum for the reaction $^{54}Fe(p,p'\gamma)^{54}Fe$ at 19.6 MeV; events due to gamma rays from 0.3 to 4 MeV and protons from 10 to 19.6 MeV were included.

Generation of the time input for the main gate is more clearly understood with the aid of Figure 10. The outputs of SCA's set to encompass four chance peaks of the TAC spectrum were combined in a logical "OR"; the output of an additional SCA, set to encompass the "true" time peak, was combined with previous signal in a second "OR" to produce the time logic signal. The "true" time signal was also fed into a logic unit whose function is discussed in the next section.

4. Data Storage and Logic

Two requirements were felt to be essential in recording the two parameter coincidence information. 1) For maximum versatility, it was desirable to store the entire coincidence array, since it was not usually obvious, a priori, what sections of it would be most interesting. This required on the order of 500 × 2000 channels to cover the energy ranges

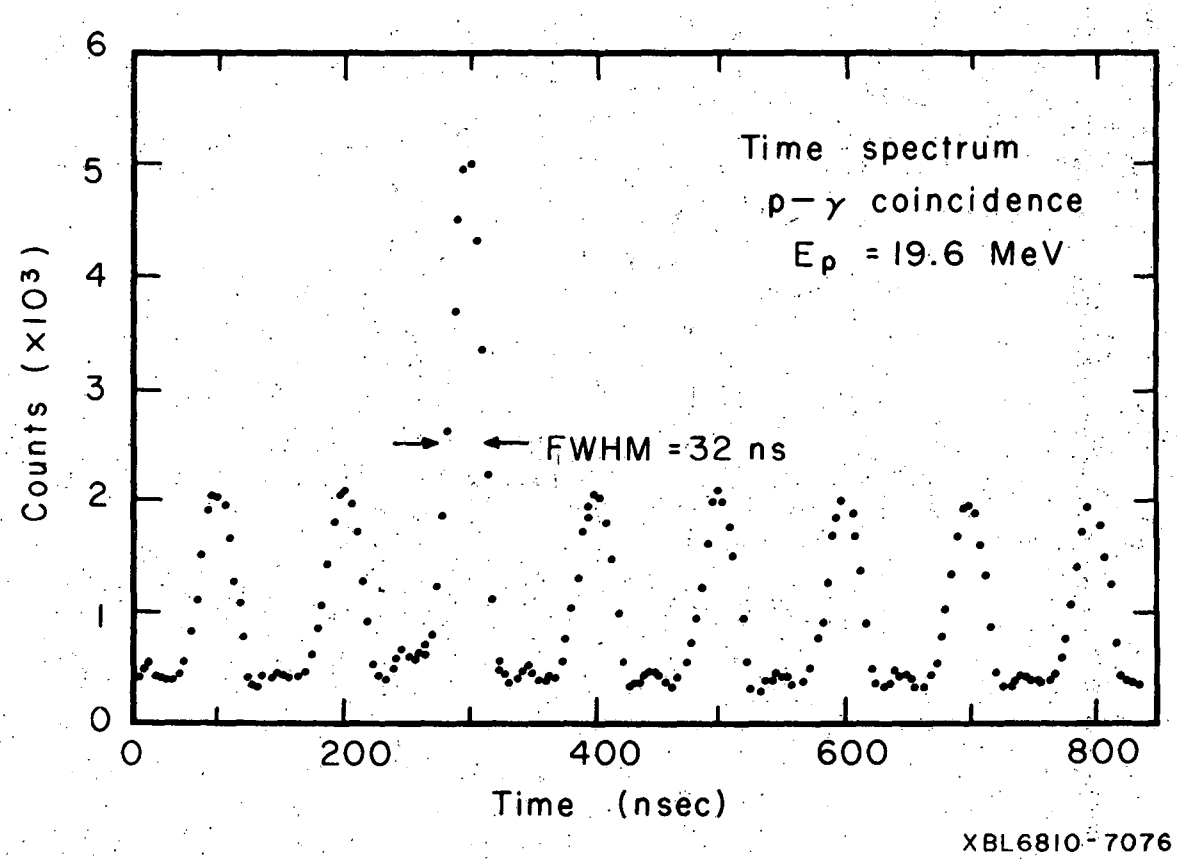

Fig. 9. Time-to-amplitude converter spectrum for proton-gamma ray coincidences from the reaction $^{54}Fe(p,p')^{54}Fe$ at 19.6 MeV. The spectrum is gated by protons from 10 to 19.6 MeV and gamma rays from 0.3 to 4 MeV. The large peak is due to true coincidences; the others are due to chance coincidences.

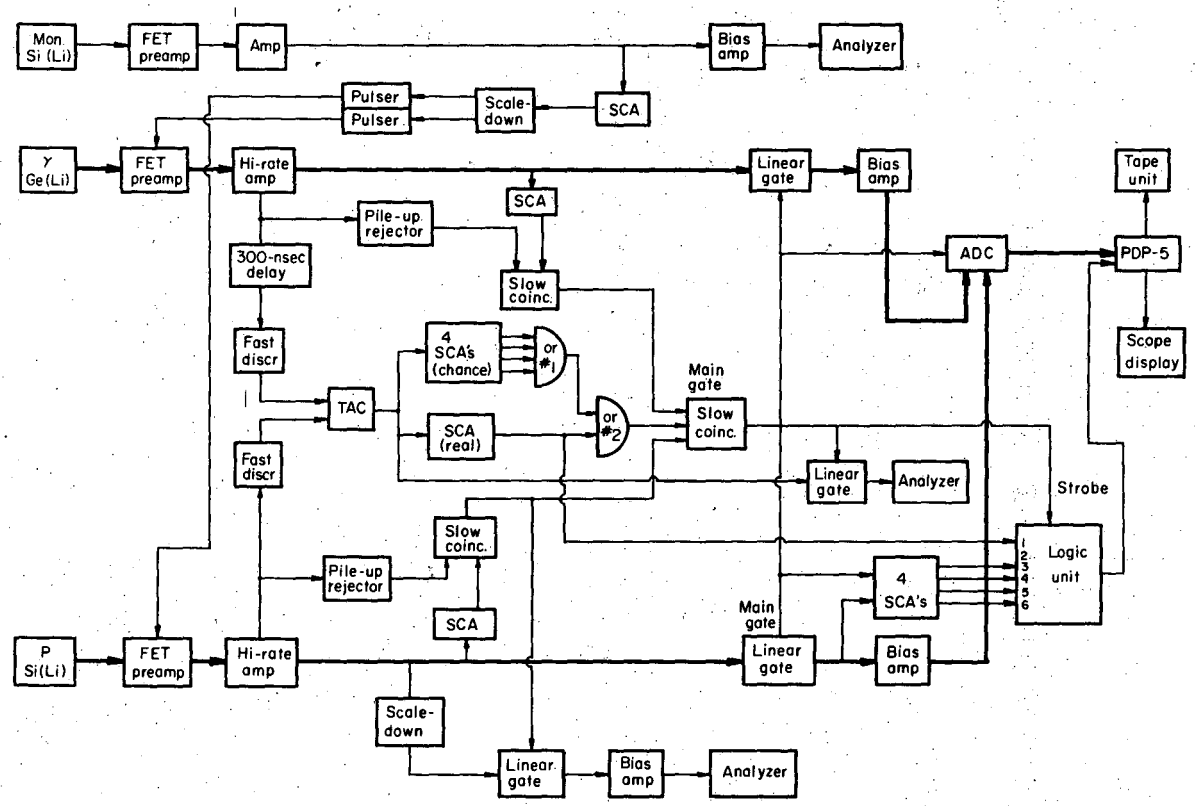

Fig. 10. Block diagram of the electronics for the ^{54}Fe spectroscopy experiment. The heavy lines indicate the paths of the energy signals from the two detectors.

in both detectors with a sufficient number of channels in the peaks. 2) It was essential to be able to monitor the progress of the experiment in order to insure the proper functioning of the system and to determine when enough data had been taken. This implied that a display of some portion of the stored data was necessary.

For the present system, the required storage and monitoring capabilities were obtained in the following manner. Valid pairs of gamma and proton signals from the biased amplifier outputs were fed into a multiplexed 4096-channel successive-approximation ADC.[48] In addition, the ADC also accepted 6 logic signals (this feature is indicated as a separate "logic unit" in Figs. 10 and 11, two of which identified the event as having occurred in a true or in a chance time peak, and four of which were generated by SCA's set around peaks in the proton spectrum. The latter, which were used for display purposes, are detailed for each experiment at the conclusion of this subsection.

The event information was transferred to a data buffer in the memory of a PDP-5 computer via an ADC interrupt of an on-line computer program. During the period of digitization and transfer ($\sim$400 μsec), an inhibit gate from the ADC prevented opening of the linear gates in each system.

Within a "real time" subroutine of the program (i.e., the program was subject to additional interrupts), the information in the data buffer was processed in the following manner. Logic signals one and two were combined with the most significant 9 bits of the proton energy signal to form a 12 bit word (one bit was not used); subsequently, this word and the 12

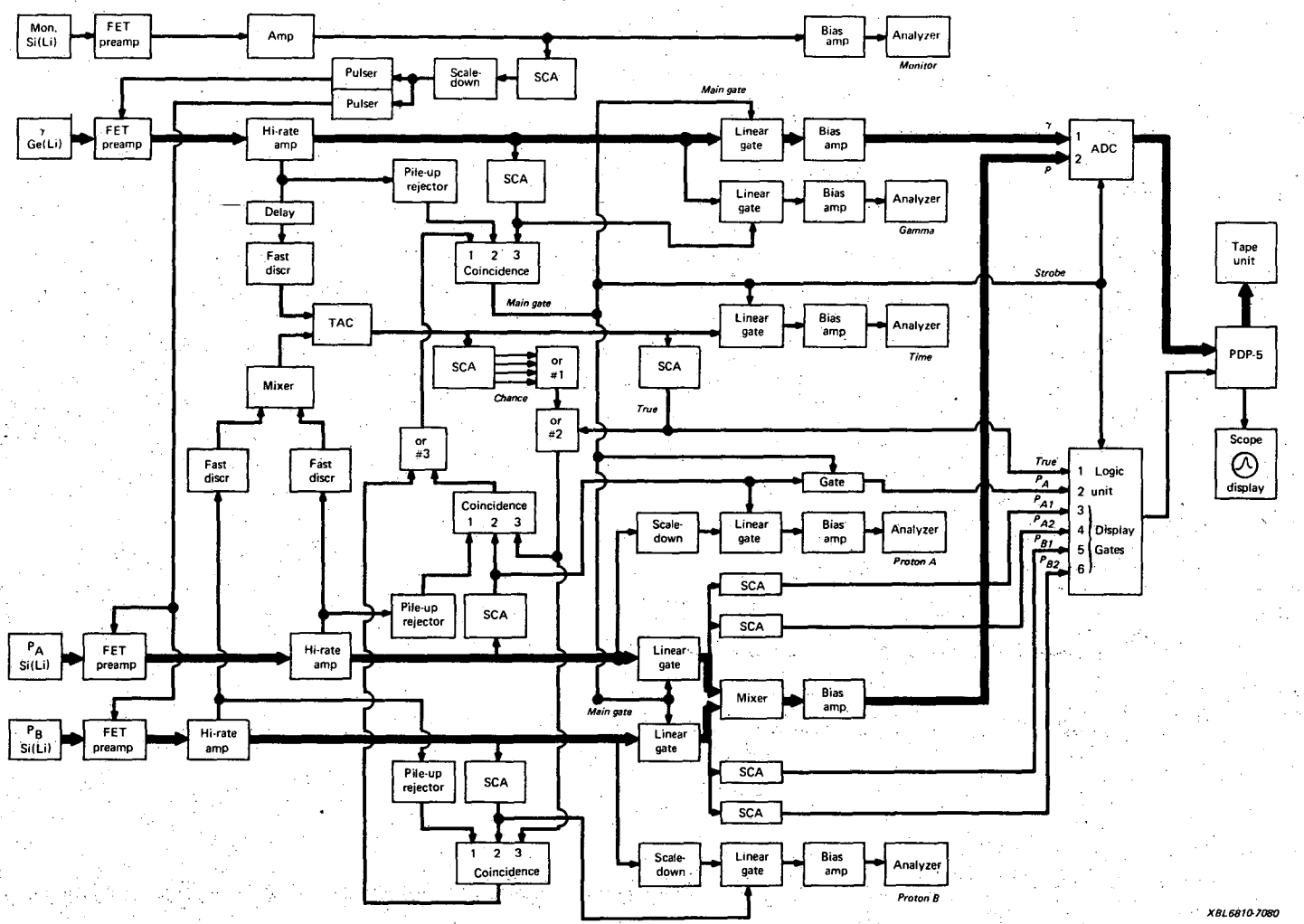

Fig. 11. Block diagram of the electronics for the spin-flip experiment. The heavy lines indicate the paths of the energy signals from the two particle detectors and the gamma detector.

bit gamma energy word were transferred to another buffer. The latter buffer was emptied onto magnetic tape after 1250 events had been collected. Further operations were performed if the first logic bit was a one (i.e., if the event was a "real"). In this case, the presence of one of the latter four logic bits produced storage of the gamma energy word of the event in one of four display fields. The background program produced a CRT display of these fields whose interpretation is now discussed for each experiment.

^{54}Fe Spectroscopy. Figure 10 shows the complete block diagram for this experiment. In addition to the time signal, four signals generated by SCA's set around peaks in the proton spectrum were fed into the logic unit. Those chosen were the elastic and three excited-state peaks. The CRT display then consisted of four-1024 channel gamma-ray spectra specified by these logic signals.

Spin-Flip Experiment. Figure 11 shows the complete block diagram for this experiment. In discussing the storage and display logic for this system, it is necessary to mention the complications incurred when using two particle detectors.

The outputs from the fast discriminators for the proton counters were mixed and fed into the start input of the TAC. Small differences in timing between the two Si(Li) counter systems were corrected for by delay lines before each fast discriminator (not shown in Fig. 11). The remainder of the fast system is identical to that previously discussed.

The slow systems were separate for each of the particle detectors up to and including the linear gate. The outputs at this point were

mixed, fed into a biased amplifier and then into the ADC.The linear gates were opened by the main gate, which was generated by coincidences between either particle detector and the gamma ray detector.

In order to distinguish between systems A and B, a logic signal generated by a wide SCA (set to encompass the entire range of interest) in system A was fed into the logic unit. In storage, this signal as well as the "real" time signal were recorded in the logic word of the event code. Additional logic signals were generated by two SCA's each, in systems A and B; these were set around the elastic and first excited state peaks in each system. The CRT display was thus four spectra of gamma rays specified by these signals.

5. Subsidiary Systems

It was essential in both experiments to preserve the non-coincidence (singles) proton spectra. This was done by providing secondary branches in the circuits for the proton signals. These signals were scaled down by a factor of 5 to 50 to provide suitable counting rates for storage in RIDL 400 channel analyzers.

A monitor proton counter was used as a check on the beam integration and to determine the energy stability of the beam. Additionally, the elastic peak in this spectrum was scaled down by a factor of 100 to 1000 and used to trigger a pulser; hence, the frequency of the pulser was proportional to the beam intensity. This pulser then fed accurately timed pairs of pulses to the proton and gamma pre-amplifier inputs. These pairs of pulses passed through the entire circuit in the same manner as real

coincidence events and were stored on tape as such. The pulser voltages were selected in such a way as to overlap with no proton counts (the pulser peak was slightly above the elastic peak) and few gamma counts (at the high energy end of the spectrum). Drifts of the pulser voltages would have indicated gain shifts of the electronics, but none were found. More importantly, the number of observed pulser coincident events stored in the two-dimentional array was a direct measure of the dead-time and pile-up losses in the entire system. Since these losses were usually about 40 to 50% of the input counts, it was crucial to know this quantity precisely.

G. High-Resolution System

For each of the two experiments, it was necessary to have high resolution singles proton spectra. These spectra were obtained in an experimental area specifically designed for high resolution measurements with precise geometry; it has been described in detail in Ref. 49.

Two 3mm thick Si(Li) detectors were used; these were cooled to -35°C with thermoelectric devices. Knock-on electrons from the target were eliminated with electrostatic electron suppression plates. The counters subtended solid angles of 1.7×10^{-4} sr and yielded resolutions of 30 keV. The total beam was measured in a Faraday cup and checked with a fixed-position monitor detector.

H. Targets

The targets used were self-supporting, isotopically enriched metallic foils obtained from the Stable-Isotopes Division of the Oak Ridge

National Laboratory. They ranged in thickness from 200 μg/cm^2 to 837 μg/cm^2. It was essential to use the thickest ^{54}Fe target (837 μg/cm^2) in the spectroscopy experiment in order to utilize the Doppler shift information (see Sec. IV.C-2).

The contaminants in the enriched ^{54}Fe were as follows:

^{56}Fe	2.81%
^{57}Fe	0.1%
^{58}Fe	0.1%

III. EXPERIMENTAL TECHNIQUES

A. General

The advent of large-volume ($\geq$ 30 cm^3) Ge(Li) detectors coupled with the development of a high-rate amplifier system has given new range to the powerful techniques of in-beam particle-gamma coincidence spectroscopy. It is with this enlarged view that we present a critical examination of some of the more general features of the present experiments.

In Sec. III.B, the factors which influence the true-to-chance ratio are considered in detail; included is an analysis of the chance coincidence problem encountered when using a pulsed beam. Section III.C is concerned with the present detector-electronics system, with particular attention given to fast-timing problems encountered with large volume Ge(Li) detectors. Finally, Sec. D deals with the practical evaluation of the number of true coincidences.

B. Analysis of the True-To-Chance Ratio

1. Evaluation of Chance Coincident Rate

The chance coincident rate, C, is related to the singles proton, C_p, and gamma, C_γ, counting rates by the general expression:

$$C(t) = C_p(t) \int_{t-\tau_f}^{t+\tau_f} C_\gamma(\tau-t)d\tau \qquad \text{(III-1)}$$

where τ_f is the fast coincidence resolving time. Now considering a pulsed beam with a period, τ_c, it is convenient to calculate the number of chance coincidences, N_i, during the ith beam burst. We make the substitution:

$$C_i(t) = N_i\ \rho(t), \qquad \text{where} \quad \int_0^{\tau_c} \rho(t)\ dt = 1.$$

Therefore:[50]

$$N_i = \int_0^{\tau_c} C_i(t)\ dt = N_{ip}\ N_i \int_0^{\tau_c} \rho_p(t) \int_{t-\tau_f}^{t+\tau_f} \rho_\gamma(\tau-t)d\tau dt \qquad \text{(III-2)}$$

In practice, a cyclotron beam burst is sufficiently narrow in time to allow the approximation:[51]

$$\rho_p = \delta(0)$$

Thus, III-2 becomes:

$$N_i = N_{ip}\ N_{i\gamma} \int_{t-\tau_f}^{t+\tau_f} \rho_\gamma(\tau-t)d\tau$$

We will define:

$$F_\gamma = \int_{t-\tau_f}^{t+\tau_f} \rho_\gamma(\tau-t)d\tau \qquad \text{(III-3a)}$$

so that:

$$N_i = F_\gamma N_{ip} N_{i\gamma} \qquad \text{(III-3b)}$$

F_γ is seen to be essentially the fraction of the total counting rate which is due to prompt gammas from the target. It should be emphasized that Eq. (III-3a) implies a time discrimination against a gamma background which is isotropic in time; it does not exclude events due to gammas which are delayed by an integral number of cyclotron periods, τ_c, from the target gammas. It was for this reason that the Faraday cup placement was chosen so that the delay time of gammas which originated there was $\sim 1/2\ \tau_c$.

To obtain the average random coincident rate, we consider an ensemble of beam bursts averaged, for convenience, over a one second time interval. The beam current, I, is then:

$$I = 1/\tau_c \sum_{i=1}^{1/\tau_c} Q_i = \overline{Q}/\tau_c$$

where Q_i is the charge of the ith beam burst. It follows that:

$$N_{ip} = C_p \frac{Q_i}{I} = \tau_c C_p \frac{Q_i}{\overline{Q}}$$

and

$$N_{i\gamma} = C_\gamma \frac{Q_i}{\bar{I}} = \tau_c C_\gamma \frac{Q_i}{\bar{Q}}$$

Therefore:[52]

$$C_{ii} = 1/\tau_c \sum_{i=1}^{1/\tau_c} N_i = 1/\tau_c \left[F_\gamma \tau_c^2 C_p C_\gamma / \bar{Q}^2 \right] \left[\sum_{i=1}^{1/\tau_c} Q_i^2 \right]$$

$$C_{ii} = \tau_c C_p C_\gamma F_\gamma F_{ii} \qquad \text{(III-4)}$$

where

$$F_{ii} = \left[1/\tau_c \sum_{i=1}^{1/\tau_c} Q_i^2 \right] / \bar{Q}^2 = \overline{Q^2}/\bar{Q}^2$$

Analogously, one may consider the random rate in which the proton and gamma ray events are not from the same beam burst:

$$C_{ij} = \tau_c C_p C_\gamma F_\gamma F_{ij} \qquad \text{(III-5)}$$

with

$$F_{ij} = \left[1/\tau_c \sum_{i=1}^{1/\tau_c} Q_i \, Q_j \right] / \bar{Q}^2$$

The subscripts are summed for all values in which i and j differ by a given number of cyclotron periods. C_{ij} is then the random coincident rate which is delayed by one or more periods from the real coincident time.

Equations (III-4) and (III-5) illustrate the danger of determining the coincident rate, C_{ii}, in the real spectrum by measuring the rate, C_{ij}, in one or more delayed spectra. It is seen that unless there are no fluctuations in beam intensity $C_{ii} > C_{ij}$.

Beams from the 88-inch cyclotron are known to have such fluctuations; thus, delayed random coincidences could not be used directly for correction of the real spectrum. Section III.D-2 discusses the approach which was adopted.

2. Factors Affecting the True-To-Chance Ratio

The real coincident rate, R, due to a state's decaying with a single gamma transition is:

$$R = \varepsilon_\gamma \Omega_p \frac{d\sigma}{d\Omega} I W(\theta) \qquad \text{(III-6)}$$

where ε_γ is the efficiency-solid angle factor for the gamma detector, Ω_p is the solid angle of the particle detector, $d\sigma/d\Omega$ is the differential cross-section for the reaction and $W(\theta)$ is the angular correlation function; the beam intensity, I, is normalized to include the target thickness.

In Eq. (III-4), we consider that F_γ and F_{ii} have been optimized, respectively, by elimination of background sources which produce gammas delayed by an integral number of τ_i, and by minimizing beam intensity fluctuations. The chance rate is then:

$$C \propto \tau_c C_p C_\gamma$$

In examining the contributions to C_p and C_γ, we consider simplified spectra in which no contaminant particle peaks are present. Therefore:

$$C_p = \Omega_p \frac{d\sigma}{d\Omega} I \qquad \text{(III-7)}$$

and

$$C_\gamma = \varepsilon_\gamma(\sigma_i W_i + \sigma_c W_c + A\sigma_B W_B) I \qquad \text{(III-8)}$$

where

$$A = \varepsilon_{B\gamma}/\varepsilon_\gamma$$

The contribution to C_γ requires some elaboration. σ_i is the total cross-section for production of the state of interest; σ_c is the sum of all cross-sections to states which cascade through the given state (corrected for the branching ratio), and σ_B is the sum of all cross-sections for processes which produce higher energy gammas and thus contribute a Compton background to the region of interest. The latter must be corrected for the difference in efficiencies between the Compton events, $\varepsilon_{B\gamma}$, and the FE peak events, ε_γ. All contributions must be multiplied by an angular distribution function W which may not be unity (W_B, in particular, may be ~ 1 in the case where many processes contribute).

The true-to-chance ratio, R/C, may be written as:

$$R/C \propto \frac{W(\theta)}{(\sigma_i W_i + \sigma_c W_c + A\sigma_B W_B) I \tau_c} \qquad \text{(III-9)}$$

Thus, R/C depends inversely on the beam intensity I but not on the counter efficiencies. It is more instructive, however, to consider the variation of R/C at a constant real coincident rate. Now, if either of the counter solid angles is increased by a factor of 2, the beam intensity may be decreased by the same factor, resulting in a corresponding decrease in R/C. The optimum R/C at fixed R is therefore obtained when the counter efficiencies are as large as is possible.

The other factors of Eq. (III-9) that depend on the reactions which occur at the chosen beam energy can be separated into two groups: those which produce gamma rays of energy E (σ_i and σ_c) and those which contribute Compton events at an energy E (σ_B). Examples of processes in which one of the two contributions above is dominant may be seen in Fig. 12. Shown is a singles spectrum of gamma rays from the reaction $^{54}Fe(p,p')^{54}Fe$ at 10 MeV; the gamma counter was at 90°. At this angle, the $0_2^+ \rightarrow 2_1^+$ (1153-keV gamma) coincident rate was about three times that for the $2_1^+ \rightarrow 0_1^+$ (1409-keV) transition. The singles spectrum, however, shows a dominant $2_1^+ \rightarrow 0_1^+$. This is because essentially all excited states have some cascade strength through the 2_1^+; on the other hand, no states below 5 MeV have a measurable cascade through the 0_2^+.

These considerations indicate the relation of gamma energy resolution to the true-to-chance ratio. If the dominant contribution to C is from σ_B, then R/C for a FE-peak summation is proportional to the FE-peak width; hence, good resolution is quite important. Processes of this type are most commonly encountered with in-beam coincidence experiments. In the $^{54,56}Fe$ spin-flip experiments, on the other hand,

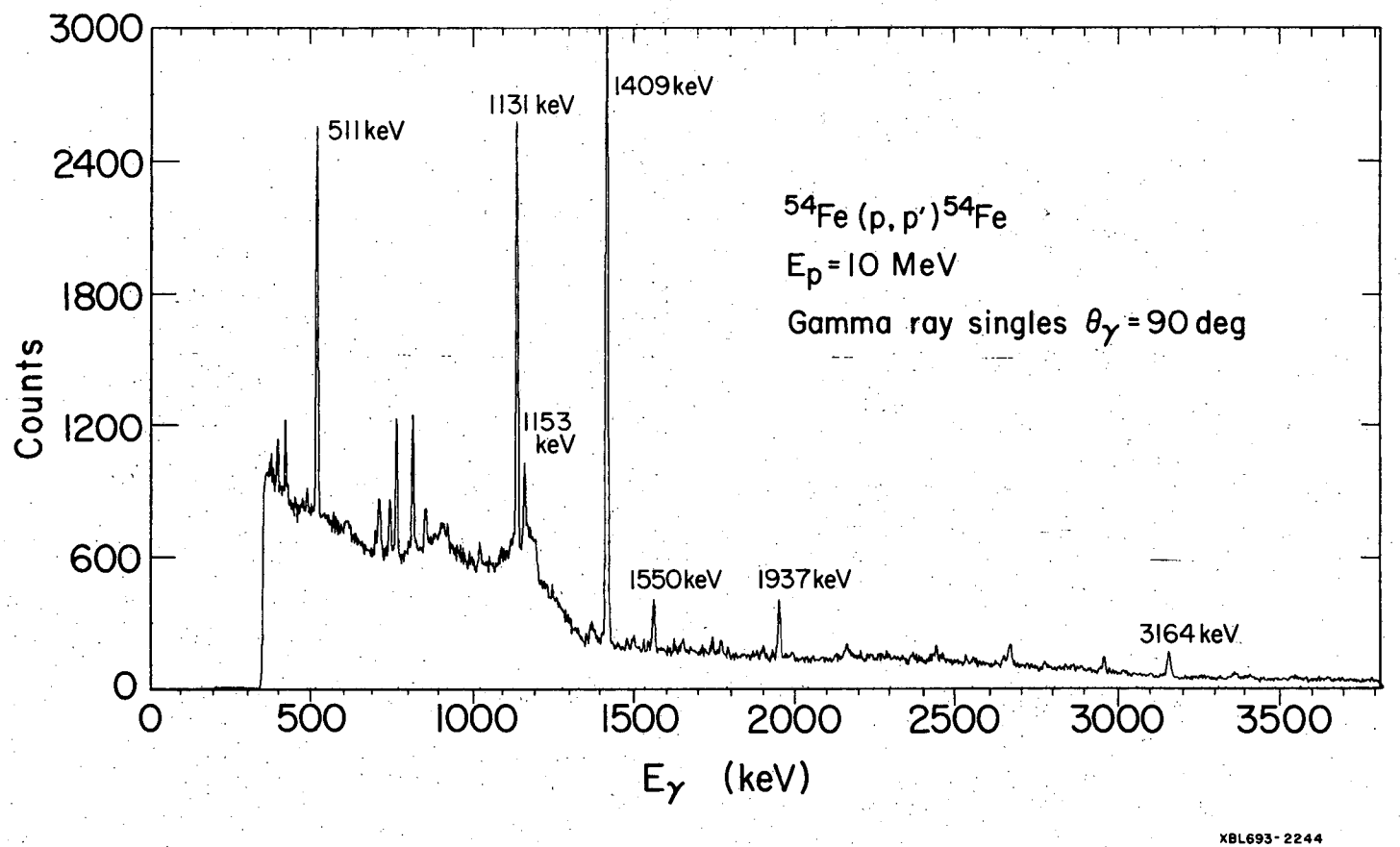

Fig. 12. Singles gamma-ray spectrum from the reaction $^{54}Fe(p,p')^{54}Fe$ at 10 MeV. The coaxial Ge(Li) detector was at 90° with respect to the beam axis.

resolution was of secondary importance, since both $2_1^+ \rightarrow 0_1^+$ transitions were strong in the singles spectra. This case is rather unfavorable since not only are contributions from σ_c large, but the measured quantity $S(\theta)$ was a small part of $\sigma_i(\theta)$.

The extension of the previous arguments to more complicated spectra is straight-forward. Resolution is clearly important in the particle spectrum if the states are closely spaced and if there is background. In gamma spectra, one often is interested in gamma rays which are located on a real background due to higher energy coincident gamma rays; good resolution is clearly helpful in such a case.

C. Detector and Electronics Systems

1. High-Rate Counting Systems

The development of the high-rate amplifier system was of major importance in the utilization of Ge(Li) detectors for in-beam coincident studies. To obtain reasonable coincident counting rates, singles gamma counting rates of $\sim 2 \times 10^4$ cps were required in the present experiments. Under such conditions, in conventional systems, pile-up would have resulted in much poorer peak resolution and higher backgrounds.

The response of the present system to high gamma counting rates is shown in Fig. 6; the spectra are of ^{60}Co, taken at 2×10^4 cps with and without pile-up rejection. The increase in FWHM was about 0.5 keV over that obtainable at low counting rates. The use of pile-up rejection makes almost no difference in the FWHM, but as is evident, a considerable reduction in background was obtained. Although the system was capable of

higher rates, little advantage was incurred, since this resulted in a higher percentage of pile-ups. The rejection rate at 2×10^4 cps was ~35% with a 20 μsec inspect time.

The modified high-rate systems for particle counting produced excellent results, although the improvement over conventional systems was not as great as that for gamma detection. For the annular counter, the peak FWHM at low rates was 55 keV for 10-MeV protons; at 1.5×10^4 cps, the FWHM increased to 70 keV. To take full advantage of the pile-up rejection system, it was essential to eliminate knock-on electrons from the target by means of a thin aluminum absorber (0.0025 inches for the annular counter and 0.005 inches for the detectors in the spin-flip experiment).

2. Fast Timing Characteristics of the Detectors

In Sec. III.B-1, it was found that the only dependence of the chance coincident rate on the fast resolving time was in the quantity F_γ. This result, however, depended on the assumption that $2\tau_f < \tau_c$. Thus, it is important to examine the factors affecting τ_f for the present system.

Considerable effort has been devoted to the study of fast-timing properties of Ge(Li) diodes.[43,53,54] Goulding[43] has given a simple analysis of the expected variations in rise time for a planar P-I-N diode. Assuming an electric field intensity in excess of 1000 V/cm, both holes and electrons have about the same drift velocity (1.5×10^7 cm/sec); then, if the event is considered to be localized in a small region (good for low-energy electrons), the expected distribution of rise times is shown in Fig. 13. For higher energy events in which the initial charge is

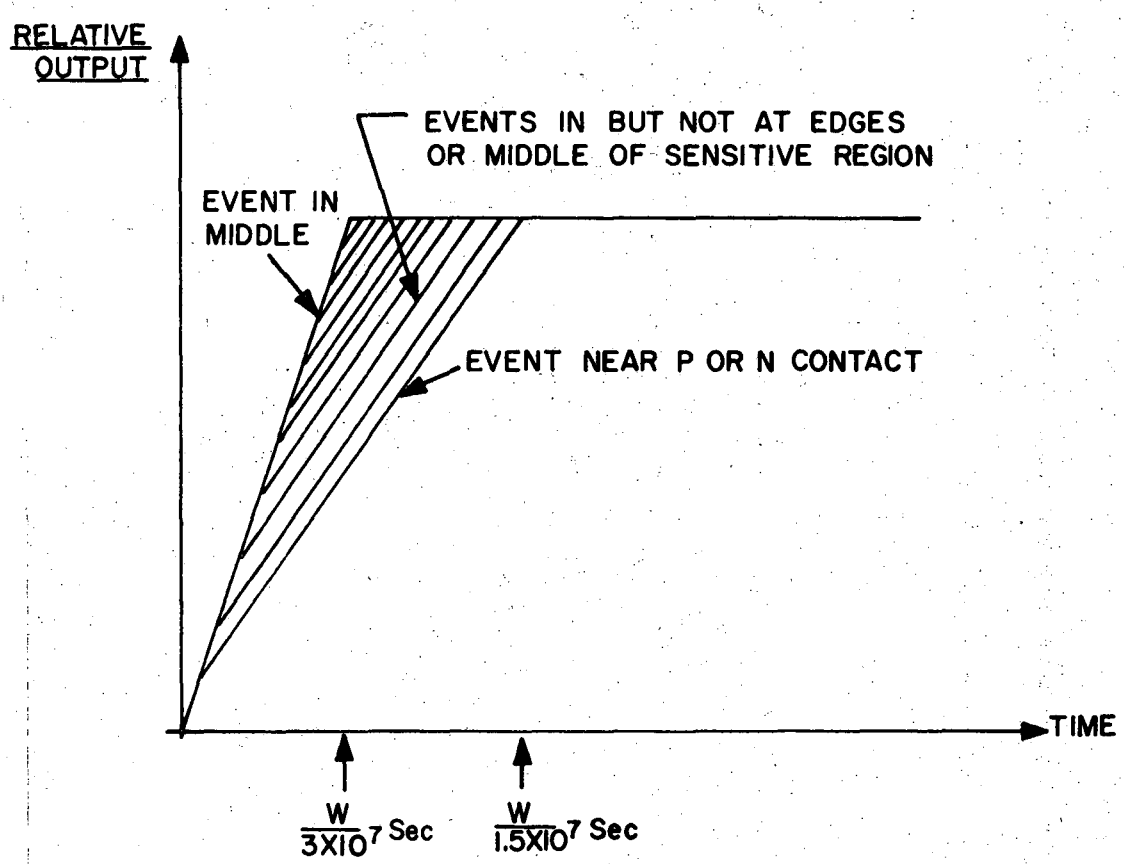

EXPECTED RANGE OF PULSE SHAPES FROM P-I-N GERMANIUM DETECTOR AT 77°K (ASSUMING V > 1000Volts/cm)

MUB-7022

Fig. 13. Expected range of pulse shapes from a P-I-N Ge(Li) detector at 77°K. (Assuming an electric field greater than 1000 volts/cm.) (Reference 43)

distributed over a finite range, the rise times will be more uniform.[54]

For co-axial detectors, the electric field strength decreases with radial distance (electric field $\propto 1/r^2$); furthermore, in CE-co-axial detectors, there is a very non-uniform field in the drifted end. As a result, it is found that the rise-time variations encountered in CE-co-axial detectors are greater than for those of the planar configuration. A detailed study of the timing characteristics of large co-axial detectors has been made by Graham et al.[53]

Because of these large rise-time variations for pulses of a given energy, cross-over pick-off timing could not be used for the Ge(Li) counter system; leading-edge (LE) timing was thus essential. In using LE timing, the problem of discriminator "walk" is encountered. This results from pulses, barely exceeding the discriminator level, which give an output delayed with respect to pulses of larger amplitude. This effect could have been corrected for either electronically[55,56] or by storing the TAC output along with the gamma ray and proton energies and correcting the data during analysis. However, the timing requirements in the present system were not critical enough to require the use of either method.

Figure 14 shows a simplified block diagram of the system used to investigate the timing properties of the detectors which were used. Figure 15 shows the timing characteristics of the Ge(Li) detector for gamma rays from the reaction $^{54}Fe(p,p')^{54}Fe$ at 10 MeV over an energy range from 0.35 to 4.0 MeV; the fast discriminator level was about 50 keV. In this energy range for this reaction, there are no known delayed gamma rays which contribute to the peak width.

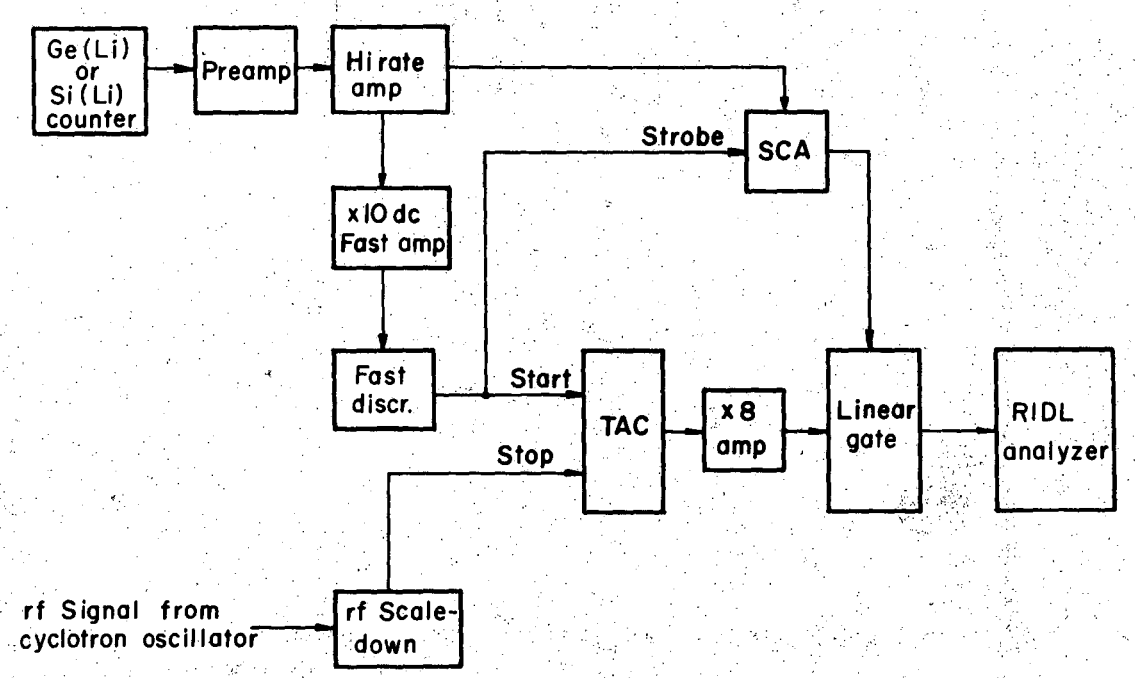

XBL693-2231

Fig. 14. Block diagram of the electronics used to investigate the timing properties of the detectors.

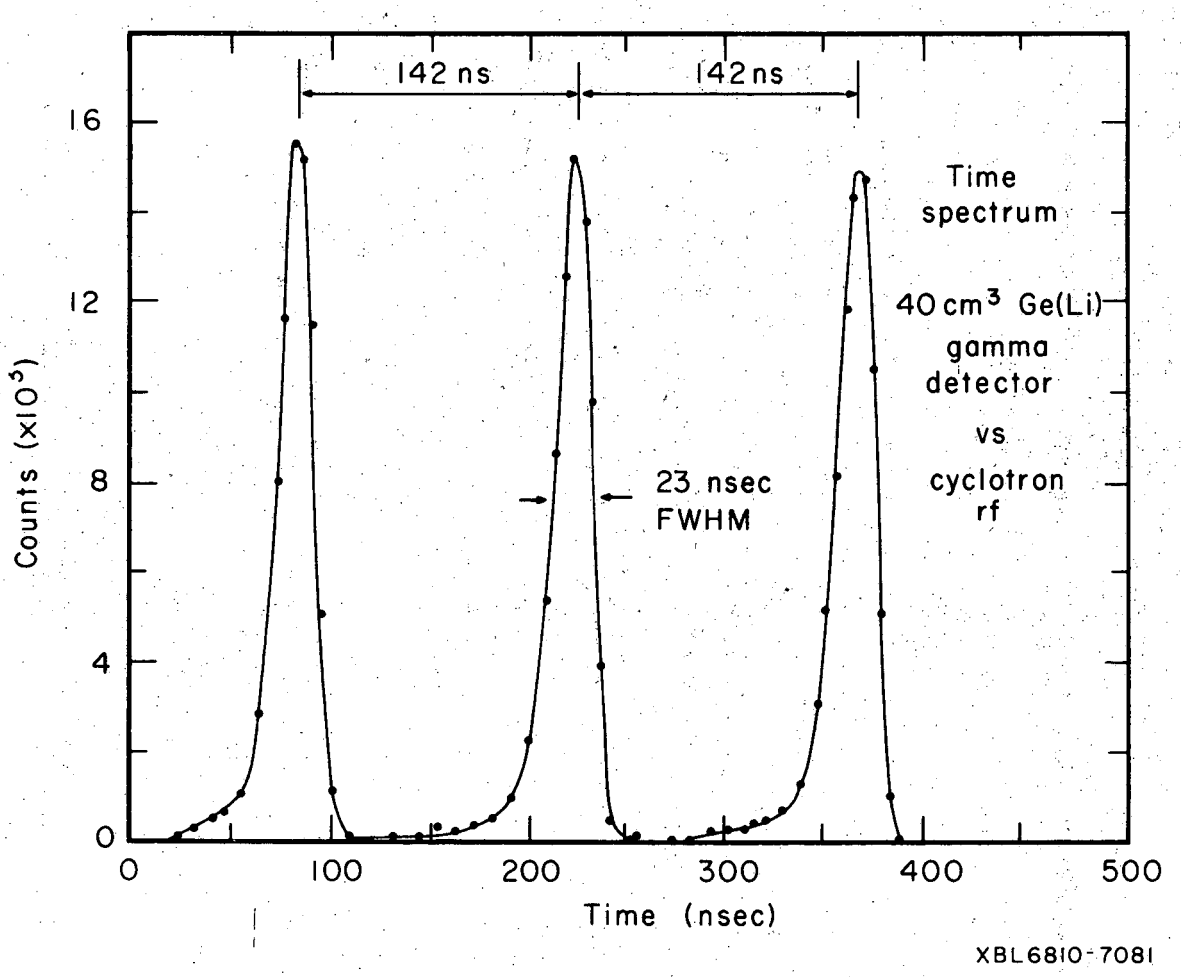

Fig. 15. Tune-to-amplitude converter spectrum with start pulses from the 40-cm^3 Ge(Li) detector and stop pulses from the cyclotron oscillator.

Timing considerations in Si(Li) detectors were less critical because of the rather small width (3mm or less) of the intrinsic region. Here, too, leading edge timing could be useful (and in the present case, more convenient) if the noise due to detector leakage current was reduced by cooling the detector. This allowed a low, fast discriminator setting.

Figure 16 shows the timing characteristics of the annular counter, using the reaction and electronics system described previously. The proton energy range included was from 3 to 10 MeV; the fast discriminator level was below 0.5 MeV.

D. Coincidence Evaluation

1. Spectrum Summation

In evaluating the number of coincident events, the usual procedure was to sum over the individual peaks in the proton spectrum to produce coincident gamma spectra. However, because the gamma spectra included FE peaks, Compton distributions, and for higher energy gammas, escape peaks, there was a choice as to the region of summation along this axis. In complex gamma decays, of course, the region was limited to clearly defined peaks, except for the highest energy transition in the spectrum.

In simple spectra, the full spectrum summation (only the part of the spectrum free of contaminant peaks) greatly increased the gamma detection efficiency, often putting it in the same range as that of NaI crystals. This method of summation, of course, eliminated the energy discrimination against chance events and resulted in poorer true-to-chance ratios.

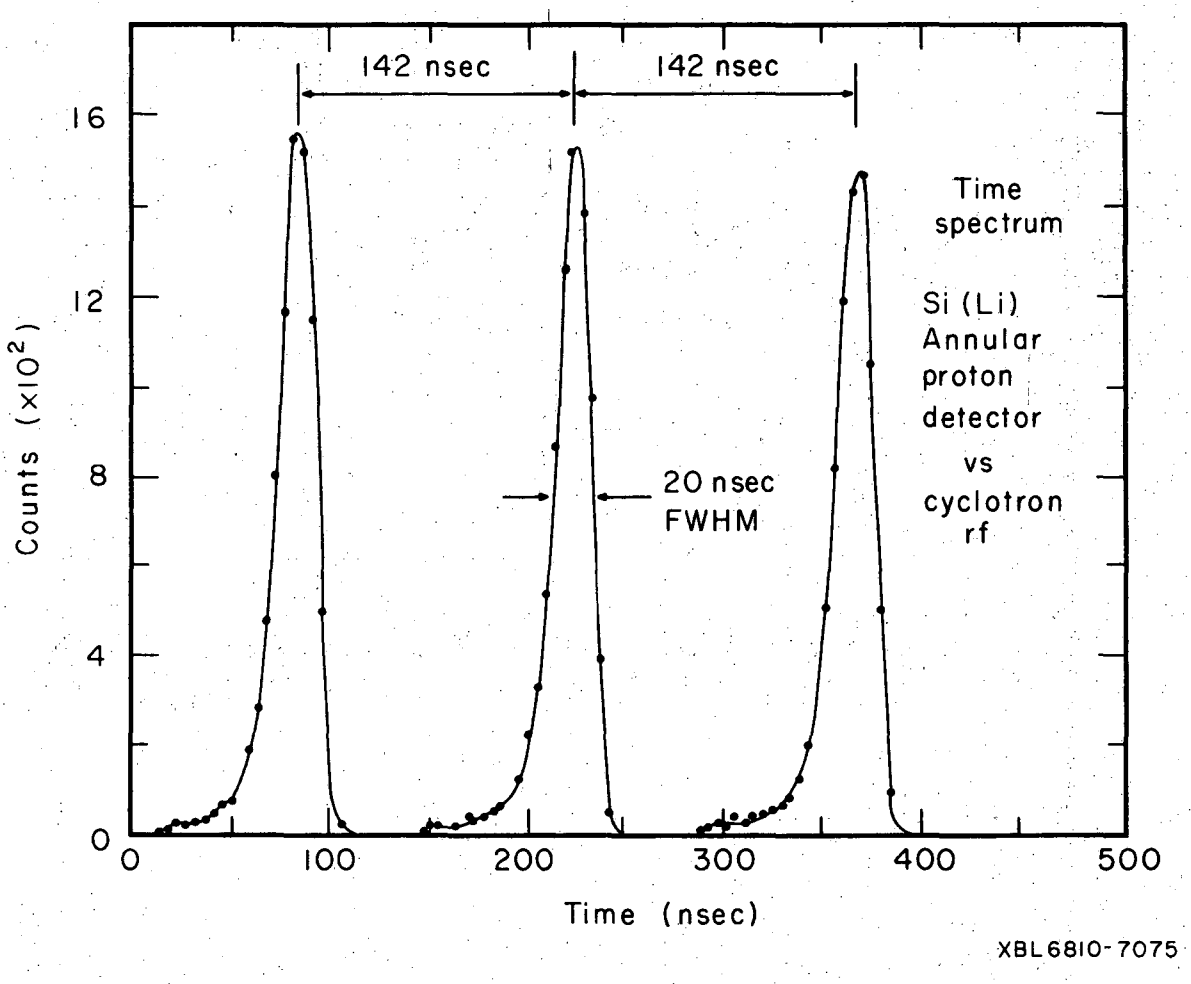

Fig. 16. Time-to-amplitude converter spectrum with start pulses from the annular Si(Li) detector and stop pulses from the cyclotron oscillator.

In more complex spectra, only FE-peak summation was used. When real background was present under a peak, it was approximated by a line and subtracted out. In some cases, a majority of the background was due to the Compton spectrum of the first 2^+ to ground transition; this could be rather precisely subtracted because the pure $2_1^+ \rightarrow 0_1^+$ transition was available with good statistics. All spectrum summations were done by hand with the aid of a desk calculator.

2. Chance Coincidence Evaluation

A common method for correcting the real spectrum for chance events is to sum the region of the coincidence array corresponding to "real" coincidences with the elastic peak, R_E. Then the number of chance coincidences in any inelastic peak, C, is given by:

$$C = (C'_I/C'_E)\, R_E \qquad \text{(III-10)}$$

The ratio of counts, C'_I/C'_E, is obtained from a singles particle spectrum; this quantity may presumably be determined with very small statistical error. This method, however, was not used because of possible systematic errors incurred by using a separate scaled-down particle system which fed into a different ADC.

The procedure adopted was to store events gated by four chance TAC peaks; thus these events were treated, electronically, in a manner identical to real events. Because of the considerations discussed in Sec. III.B-1, it was necessary to establish a scale factor between the real and chance arrays. The factor was the number of gamma-elastic counts

in the chance array, C_E, divided by the corresponding number in the real array, R_E; this quantity, which would be 4 for a non-fluctuating beam, was usually found to be 3.7. The number of chance events in any real coincident peak was thus:

$$C = (R_E/C_E)\, C_I \qquad \text{(III-11)}$$

where C_I is the number of counts in the chance array for the same region in which the real array was summed. The error, σ'_R, in the number of real coincident events, is then:

$$\sigma'_R = (\sigma_R^2 + \sigma_C^2)^{1/2} \qquad \text{(III-12)}$$

There errors on all quantities from Eq. (III-11) contributing to σ_C have been included.

3. Pile-Up Rejection and Dead Time Losses

A most essential consideration in the present experiments is the evaluation of the number of coincidences lost due to dead-time and pile-up effects. The expected losses from these effects may be estimated from the expression:

$$B = e^{-C\tau} \qquad \text{(III-13)}$$

where C is the total singles counting rate, τ is either the dead time of an electronic device or the rejection time of a PUR, and B is the fractional counting rate of "good" events. With this definition, the

measured number of real counts may be related to the number which actually occurred during the counting time.

Applying Eq. (III-13) to the conditions encountered in the spin-flip experiment, with C_γ = 20,000 cps and C_p = 7,000 cps, we find that the losses due to various components are approximately as follows:

SOURCE	1 - B
Gamma PUR	0.33
TAC Dead Time	0.04
Proton PUR	0.07
ADC and Data Storage	0.02
Total	0.46

In order to evaluate B accurately, the system described in Sec. II.F-5 was used, in which pulser coincidences were randomly generated (in proportion to the beam intensity) and stored in the coincidence array. The quantity B was, then, the number stored, divided by the number generated.

IV. ^{54}Fe SPECTROSCOPY

A. ^{54}Fe Excitation Function

Previous experiments on ^{54}Fe at this Laboratory had indicated that inelastic cross sections for the ^{54}Fe(p,p') reaction varied quite strongly with energy in the region around 9-MeV incident proton energy. For this reason, prior to performing the coincidence experiment, the excitation function for this reaction was measured in steps of 100 and 200 keV from 8 to 13 MeV. For the experiment, the high resolution experimental area described in Sec. II.G was used. Figure 17 shows the results of the experiment from 8.5 to 10.5 MeV for states up to 4.287 MeV.

Changes in inelastic cross section due to small shifts in beam energy during the coincidence run could have produced errors in normalization. It was, therefore, important to choose a beam energy where the excitation function was reasonably flat, thereby minimizing the variation of cross section with energy. It is apparent from Fig. 17 that this criterion could not be met simultaneously for all states; however, it was felt that 10 MeV was a good compromise for most of them.

B. Coincidence Experiment

The intensity of gamma rays, in coincidence with inelastically scattered protons detected in the range 168° to 172°, was measured at 90°, 70°, 55°, 40°, and 25°, with respect to the beam axis. The total data aquisition time at each angle was about 10 hours. This was obtained by summing the counts from seven separate cycles through the angular range. By taking a series of short runs at each angle and subsequently combining

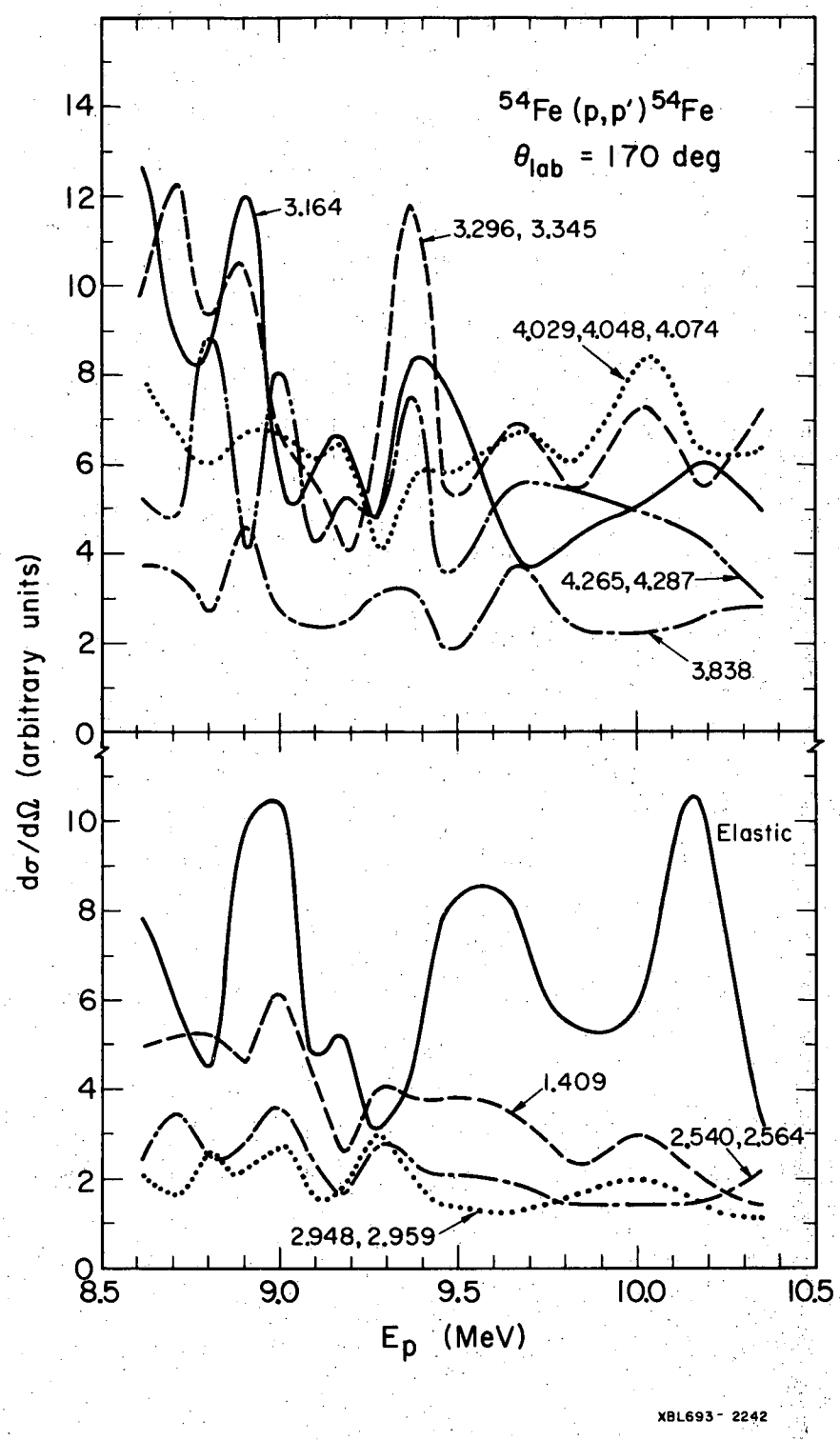

Fig. 17. Excitation functions for various states in the reaction ^{54}Fe(p,p')^{54}Fe from 8.5 to 10.5 MeV. The differential cross sections were measured at 170 deg lab angle in steps of 100 keV and 200 keV.

them, it was hoped to further reduce the effect of any normalization error due to beam energy fluctuations.

Beam intensities, which were usually about 50 to 60 nanoamps, produced counting rates of ∿20,000 cps in the gamma detector and ∿15,000 cps in the annular Si(Li) detector. The total rate of real coincidences was about 25 cps. The precautions taken to insure that no shifts in beam energy occurred have been outlined in Sec. II.A-2. The beam energy was monitored by periodically checking the peak positions in both the monitor and annular-counter spectra. Within the sensitivity of this method, no energy shifts greater than 10 keV were observed during the run. Both proton singles spectra were also checked for variations in the number of inelastic counts per micro-coulomb; this quantity was constant to within 2%.

C. Analysis

1. Angular Correlations

The analysis was accomplished by summing the coincidence array over all gamma-ray energies to produce real and random proton coincidence spectra. Figure 18 shows an example of the latter; it is equivalent to a singles spectrum. Gamma coincidence spectra were then generated for each peak which was cleanly resolved in the proton spectrum. Summation of the peaks in the gamma-coincidence spectra varied considerably, depending on the complexity of the spectrum. For spectra generated from well-separated states in the proton spectrum, the gamma summation for the highest energy transition included the FE peak, escape peaks (if any), and Compton

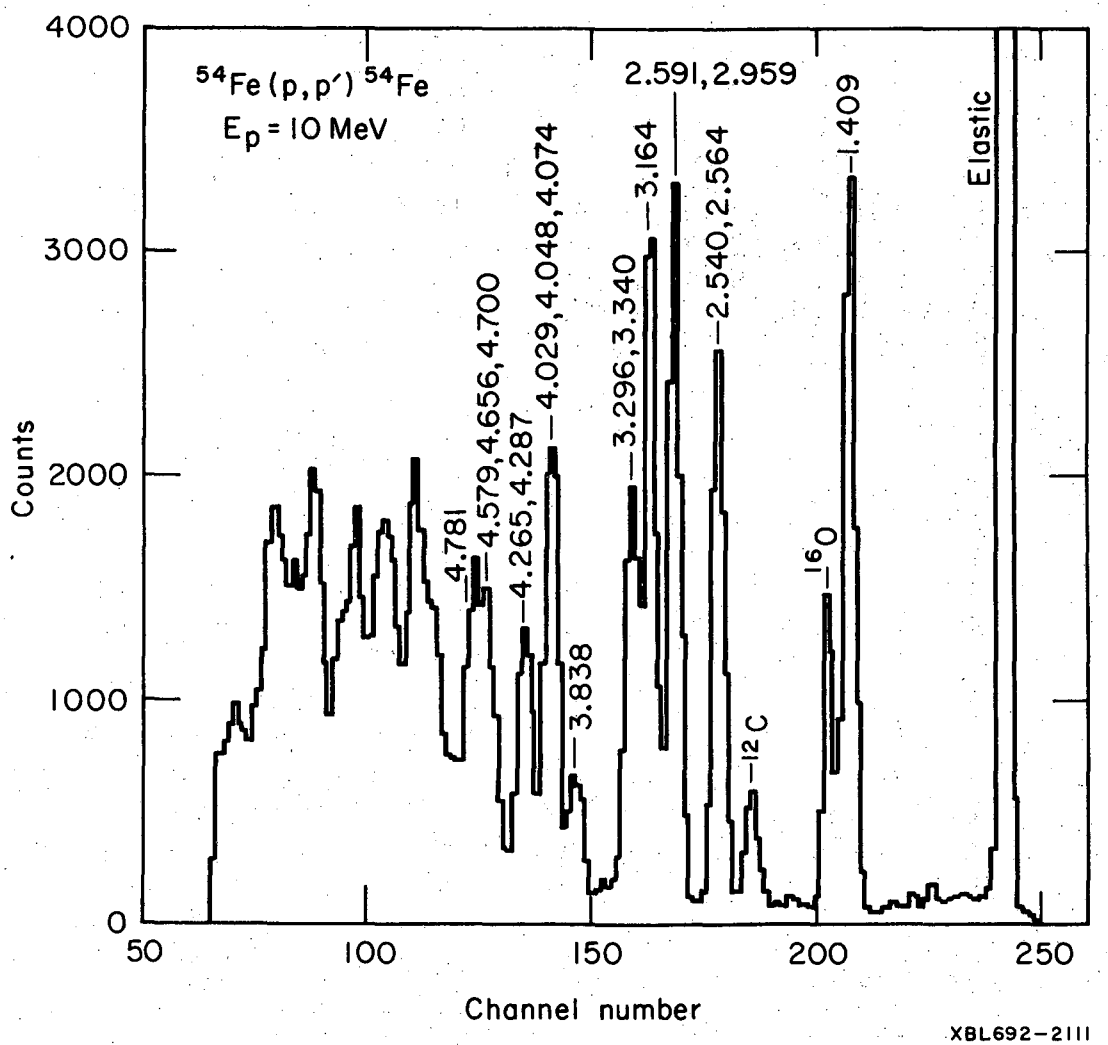

Fig. 18. Spectrum of protons from the reaction $^{54}Fe(p,p')^{54}Fe$ at 10 MeV. The protons were detected by the annular Si(Li) counter at 168-172 deg lab angle. The counting rate was 15,000 counts/sec.

distribution. This procedure was used only in cases where it was clearly justified, and in all cases, the results were checked against the corresponding FE-peak summations. For lower-energy gamma rays in simple spectra, and in the case of more complicated spectra, only peak summation was used. In these cases, where necessary, an average background was evaluated by summing a few channels on either side of the peak and subtracted out.

For states which were not cleanly resolved in the proton spectrum, the total number of gamma ray counts was obtained by summing the appropriate FE-peak region in all spectra which contained counts due to the given state.

The spectra were normalized to the total charge collected on the Faraday cup. Equivalently, the total number of monitor counts could have been used, since the two methods yielded identical results within 1.5 to 2%. The dead-time and pile-up rejection losses were accounted for in the manner discussed in Secs. II.F-5 and III.D-3.

Errors. Since accurate error evaluation is essential to the spin assignment arguments given in Sec. IV.D, great care was taken to eliminate systematic errors from the present analysis. For the highest-energy gamma-ray transitions, no background (i.e., real coincident background) was present and the errors quoted are those given by Eq. (III-12). When background subtraction was necessary, only the statistical errors from the background evaluation were combined with those of Eq. (III-12). In some cases, it was advantageous to subtract the Compton background from the cascade $2_1^+ \rightarrow 0_1^+$ transition (present in all spectra). This was possible since the pure $2_1^+ \rightarrow 0_1^+$ spectrum was available. All statistical errors propogated by this procedure were included.

Fortunately, there existed a method of checking the assumption that statistical errors were dominant in the present analysis. The 2.564-MeV state was determined to be a 0^+ by Church et al;[57] therefore, the observed $0_2^+ \rightarrow 2_1^+$ transition must be isotropic. As is seen in Fig 19, a fit to the experimental angular distribution using only an isotropic term is consistent within the errors, which are ∿2.8%. Further checks were obtained by fitting the ground state transitions for the known 2^+ states at 1.409, 2.959, and 3.164 MeV with theoretical $2^+ \rightarrow 0^+$ curves from Eq. (IV-1); these are shown in Fig. 19. The χ^2 obtained for the 2.959 and 3.164-MeV states are reasonable (respective average errors on the points were 1.4% and 1.1%). However, χ^2 obtained for the 1.409-MeV state suggests that an additional error of about 1% may be present; this was necessary to reduce χ^2 to the 50% confidence level; the statistical errors ranged from 1.6% at 90° to 0.66% at 40°. The effect of such an error would be quite small on any of the other angular distributions. It appears, then, on the basis of this evidence, that the assumption of negligible normalization error is justified.

Method of Analysis. The method of analysis used is quite similar to that of Poletti and Warburton.[22] Equation (I-1) may be written as:

$$W_T(\theta) = \sum_k [\rho_k(a,0)I(0) + \rho_k(a,1)I(1)]\ F_k(ab)Q_k P_k(\cos\theta) \quad \text{(IV-1)}$$

where

$$P(0) = I(0)/(I(0) + I(1)) \text{ and } P(1) = I(1)/(I(0) + I(1))$$

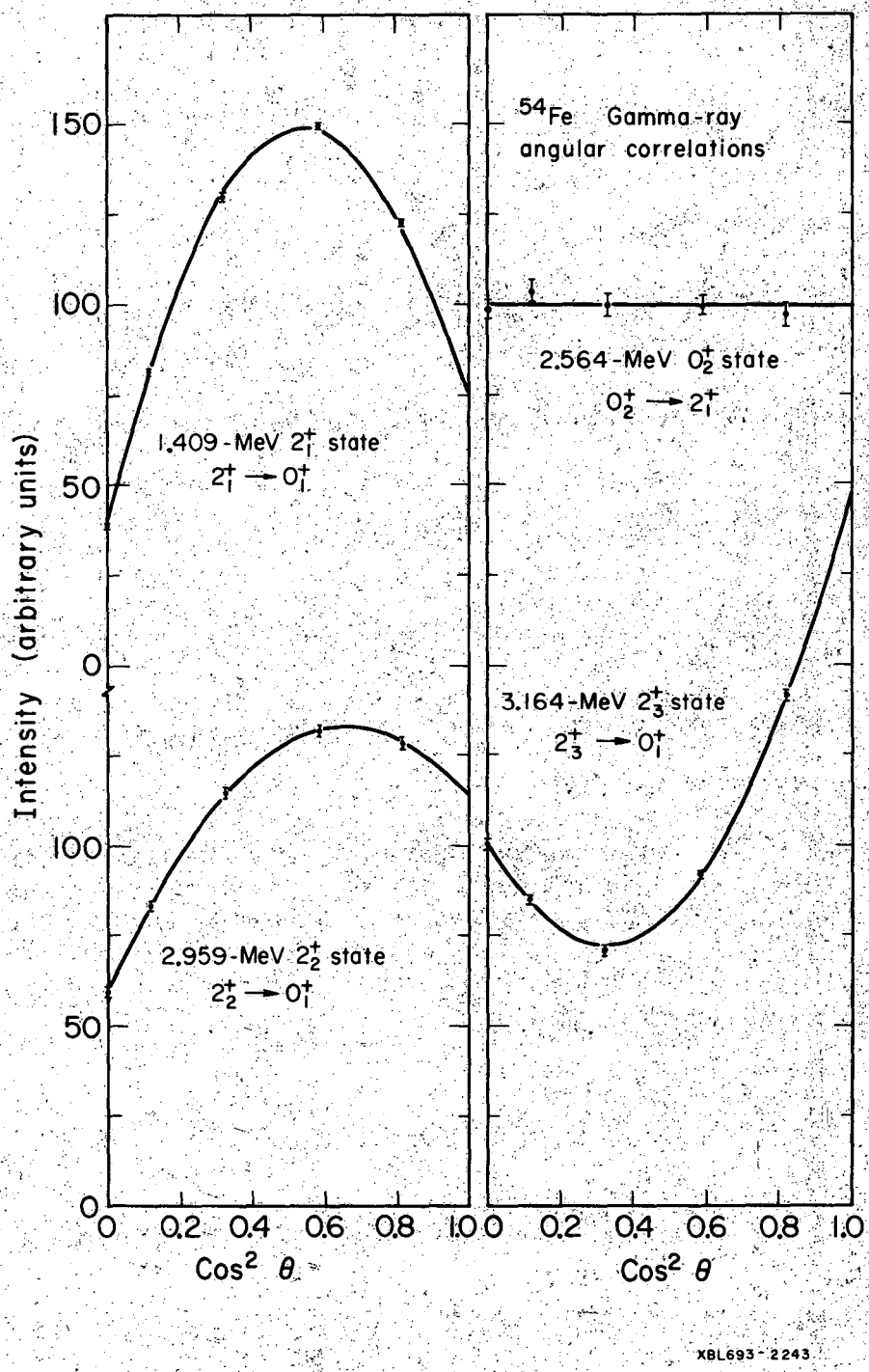

Fig. 19. (a) Theoretical fits, assuming J_i=2 and J_f=0, to the experimental angular correlations for the 1.409-MeV state (1.409-MeV gamma ray) and the 2.959-MeV state (2.959-MeV gamma ray).

(b) Theoretical fits to the experimental angular correlations for the 2.564-MeV state (1.155-MeV gamma ray) assuming J_i=0, and for the 3.164-MeV state (3.164-MeV gamma ray) assuming J_i=2 and J_f=0.

For assumed initial and final spins, the unknown parameters of Eq. (IV-1) are δ, I(0), I(1); the I's are constrained to be positive. The multipole mixing ratio, δ, enters the F coefficients quadratically; however, a linear least squares procedure may be used if δ is not considered to be a continuous variable. χ^2 is then minimized with respect to I(0) and I(1) for a range of values of δ. χ^2 is defined as:

$$\chi^2 = \frac{1}{n} \sum_i \left(\frac{W_t(\theta_i) - W_E(\theta_i)}{\sigma_i} \right)^2$$

where n is the number of degrees of freedom; in the present case, it was the number of data points minus two. Equation (IV-1) was evaluated for values of δ in steps of $\tan^{-1}(\delta) = 1$ from $-90°$ to $90°$.

We have adopted the standard method of explicitly displaying the dependence of χ^2 on δ by plotting χ^2 versus $\tan^{-1}(\delta)$. These curves showed solutions for certain values of δ for at least one of the spin combinations (see Fig. 24, for example). Accepted solutions were those exhibiting a χ^2 within the range expected for n-2 degrees of freedom as given by the χ^2 probability tables.[58] Spins which did not give solutions below the 1% confidence level were assumed to be incorrect.

In most cases, it was possible to obtain statistically significant angular distributions for more than one gamma ray from a given state; these consisted of either two branch decays from the state or two gamma rays in cascade. In such cases, χ^2 was minimized with respect to all the transitions simultaneously. For the second transition in a cascade, this involved the use of Eq. (I-2).

In the simultaneous analysis of more than one angular distribution, it was necessary to normalize the curves to a common total intensity. This was done by first fitting the curves individually with the expansion:[22]

$$W(\theta) = A_0 + A_2 Q_2 P_2(\cos\theta) + A_4 Q_4 P_4(\cos\theta) \qquad \text{(IV-2)}$$

then dividing the data points by A_0. In the subsequent analysis, it was possible to vary the mixing ratio of only one transition at a time; the others were fixed at an assumed value. In such cases, several runs were made, in which the mixing ratio considered the variable was changed. This was necessary to eliminate the possibility of missing any minima.

Population of m > 1 Substates. Litherland and Ferguson[21] have considered the effect of the finite size of the annular detector on population of $|m| \geq 2$ substates. On the basis of their work, we have estimated the population of $|m| = 2$ substates to be on the order of 3% and that of $|m| > 2$ to be negligible. In order to determine the effect of $|m| = 2$ substate population, all fitting was done twice--once with $P(2) = 0$ and once with $P(2) = 0.1\ P(1)$. In most cases, the two calculations were quite similar and in no case were additional spin solutions obtained using the latter calculations.

Multipole Mixing Ratios. It has become common practice to evaluate the errors for multipole mixing ratios by the following procedure. The point where the χ^2 curve reaches a minimum is normalized to the 50% confidence level. The two error limits are then given by the points at which the curve crosses the 10% confidence level. This procedure has the

advantage of eliminating the dependence of the quoted errors on the absolute value of χ^2 determined in the fitting. The additional uncertainty incurred by population of $|m| \geq 2$ substates has been included by some authors.[22] However, we have found this effect to be negligible; therefore, only the errors evaluated by the first method are given in the present analysis.

2. Doppler Shift Analysis

The usual procedure in measuring an attenuated Doppler shift is to observe the gamma-ray energy at two widely separated angles. The maximum shift in this case is given by:

$$\Delta E_{max} = \frac{v_0}{c} (\cos\theta_1 - \cos\theta_2) E_0 \qquad \text{(IV-3)}$$

In the present experiment, the angular range spanned was only from 25° to 90°. However, the precision with which the centroid shift could be determined was increased by evaluating the centroid of the peak at all five angles. A least-squares minimization was then used to calculate a line of the form $E_0 + \Delta E_{obs}(\cos\theta)$. The ΔE_{obs} given in the following discussion is listed in terms of $E_{25°} - E_{90°}$. The errors in ΔE_{obs} were obtained by combining the statistical errors from the centroid evaluations with an estimate of the error due to the uncertainty in the region over which to evaluate the centroids. These estimates were in general agreement with those inferred from the least squares fit.

To obtain ΔE_{max}, the initial recoil velocity v_0 was calculated from the kinematics of the reaction for each state. This quantity was then averaged over the angluar acceptance of the annular counter. Further effects due to the finite size of both counters were estimated to be about 1% and were therefore neglected.

As was discussed in Sec. I.B-3, in order to relate the measured attenuation factor, $\Delta E_{obs}/\Delta E_{max}$, to the quantity $F(\tau)$ from Eq. (I-4), it was necessary to know dE/dx throughout the range of velocities. We have used the form:

$$dE/dx = k_e v + (dE/dx)_n$$

The first term is the electronic contribution to the stopping power, which in the theory of Lindhard, Scharf, and Schiott[28] (LSS), is proportional to the velocity of the ion. The compilation of data by Northcliffe[59] shows that in the velocity range $v/c \leq 137$, this form for the electronic stopping is accurate, but that the values of k_e predicted by LSS are systematically about 20% too low. No data were analyzed, however, for ions as heavy as ^{54}Fe.

Eswaran et al.[60] have measured the lifetimes of states in ^{56}Fe, ^{62}Ni, and several isotopes of Cu by the Doppler Shift Attentuation Method. They obtain k_e by interpolating from stopping power data on several types of ions in nickel. Their value of k_e for ^{56}Fe is essentially that predicted by LSS. The predicted lifetime of the first 2^+ state in ^{56}Fe agrees well with that obtained from other methods.

A more recent analysis of heavy ion stopping data has been given by Steward and Wallace.[61] Their work included some of the data analyzed by Northcliffe and, additionally, fission fragment range data. On the basis of their systematics, the value of k_e for ^{54}Fe ions stopping in ^{54}Fe is 12% higher than that of LSS. We have chosen to use this latter estimate of k_e in the present analysis.

The predicted curve of the nuclear stopping power $(dE/dx)_n$ has not been tested directly by experiment. We have therefore adopted a functional form, given in Ref. 61, which fits $(dE/dx)_n$ given by LSS. In the Thomas-Fermi units of energy and distance (see Refs. 25 and 28):

$$(dE/dx)_n = 4.57\ \varepsilon^{\frac{1}{2}} \exp(-2.54\ \varepsilon^{0.277}) \qquad \text{(IV-4)}$$

Some calculations were also made using the form:

$$(dE/dx)_n = 0.4/\varepsilon^{\frac{1}{2}} \qquad \text{(IV-5)}$$

In the present analysis, it made little difference in $F(\tau)$ whether Eq. (IV-4) or (IV-5) were used. Figure 20 shows the nuclear and electronic stopping powers over the relevant velocity range for the present experiment.

We have included an estimated 10% error in $F(\tau)$, resulting from the lack of knowledge of dE/dx. The errors in the mean lifetimes are thus a combination of the uncertainties in $\Delta E/\Delta E_0$ and in $F(\tau)$.

The range of the recoils predicted from the total dE/dx was $\sim$160 $\mu g/cm^2$, which is a sizable fraction of the target thickness of

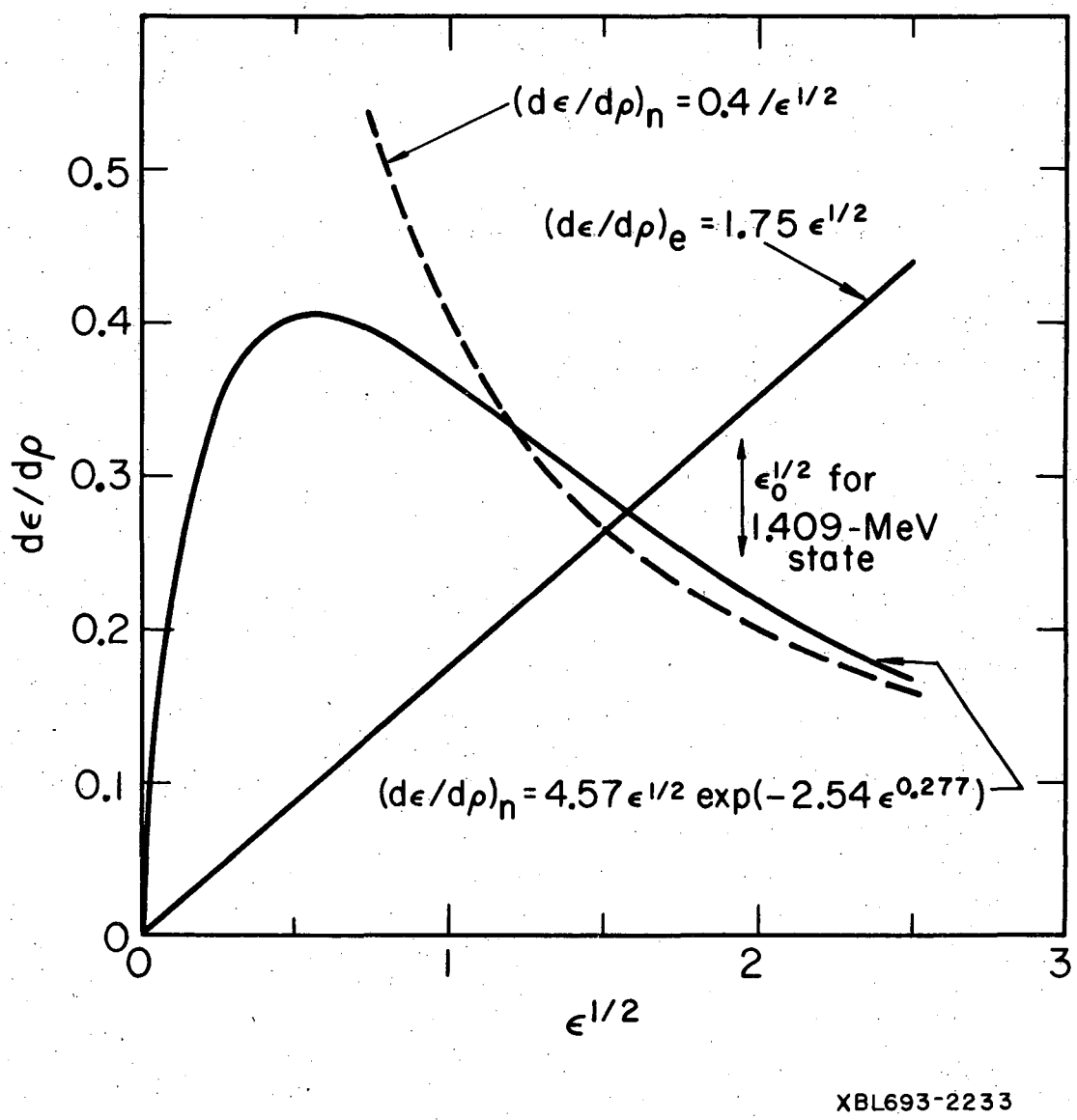

Fig. 20. Stopping power ($d\epsilon/d\rho$) versus velocity ($\epsilon^{1/2}$) both in Thomas-Fermi units. Shown are the electronic stopping power and two functional forms which approximate the nuclear stopping power.

837 $\mu g/cm^2$. Thus it was necessary to correct the predicted $F(\tau)$ for those ions which escaped from the target. This was done by constructing a curve of distance versus time. Then for recoils within the total range of the back of the target, Eq. (I-4) was integrated out to a time t_e at which the recoil escaped from the target; in the remaining integration $v(t)$ and $\cos\theta(t)$ were constant at the values $v(t_e)$ and $\cos\phi(t_e)$, respectively. Figure 21 shows the predicted $F(\tau)$ curve with and without this correction for the recoils of 3.164-MeV state in ^{54}Fe.

Comparison of the lifetimes derived in the present analysis to those obtained from other experiments is given in Sec. IV.D-1.

3. Observed States

Accurate excitation energies from high resolution (p,p') experiments on ^{54}Fe have been reported by Aspinall et al.[62] and by Sperduto and Buchner.[63] This information was quite valuable in allowing the unambiguous interpretation of the coincidence spectra.

All levels below 5 MeV which were seen by Aspinall et al. were observed in this experiment. Further, the known 6^+ state at 2.948 MeV which was not seen in the high resoltuion (p,p') work was observed here. Sperduto and Buchner[63] report a level not seen in Ref. 62 which was unresolved from a strong level at 2.540 MeV; the presence of this level was inferred from a peak shape analysis. Hansen et al.[64] have reported levels at 2.537 and 2.550 MeV seen in the $^{54}Fe(d,d')^{54}Fe$ reaction at 7.5 MeV. Both states were made with very small cross sections (0.02 and 0.03 mb/sr, respectively). In the present coincidence experiment, we have

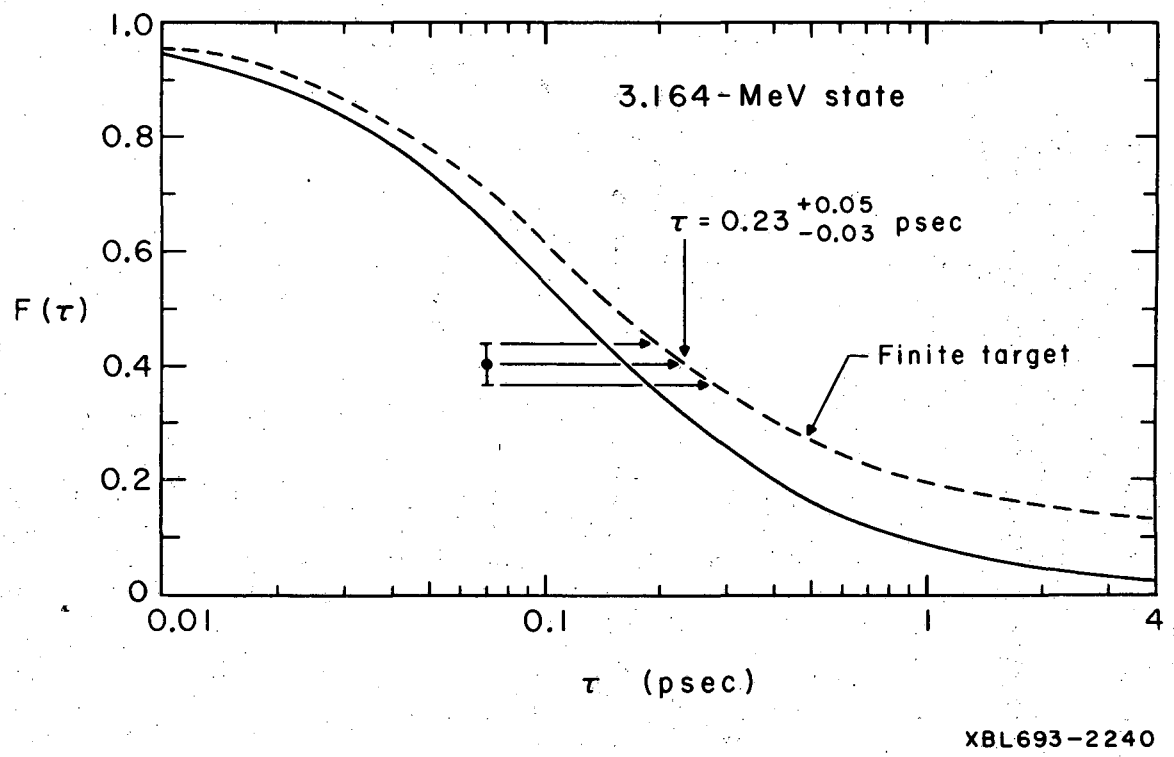

Fig. 21. The expected Doppler-shift attenuation versus mean lifetime for the 3.164-MeV state of ^{54}Fe. The dotted curve has been corrected for the effect of finite target thickness. The point shown indicates the experimentally observed attenuation factor and estimated error.

observed only one level in this energy region--that at an excitation energy of 2.539 ± 0.001 MeV. The gamma-ray coincidence spectrum (Fig. 23) reveals no additional transition either to the 1.409-MeV 2_1^+ or to the ground state. (The level at 2.564 MeV, which was unresolved from the 2.539-MeV level in our proton spectrum, was seen in both the (p,p') and (d,d') experiments and thus presents no problem.) Furthermore, within the experimental resolution (5 keV), no transition to another state from any higher excited state was observed. In another coincidence spectrum taken at 9 MeV incident proton energy, no evidence was seen of any level but that at 2.539 MeV.

We have identified the 2.539-MeV state as having $J^\pi = 4^+$, which is in agreement with the assignment of Wegener,[65] who observed a 4^+ state at 2.537 ± 0.002 MeV in the decay of ^{54m}Co. Since our excitation energy assignments are in general agreement with those of Sperduto and Buchner, their level at 2.540 MeV is probably the 4^+ (see in Ref. 62 at 2.540 MeV). The evidence for the presence of another level then is somewhat contradictory. We conclude that if an additional level is present in the region of 2.54 MeV, then it is excited in our work with a differential cross section less than 0.005 mb/sr (this is less than 5% of the 4_1^+ cross section). This applies to angular range 168° to 172° at proton energies of 9 and 10 MeV.

A comparison of the excitation energies from this experiment with those from previous work is shown in Table I. The agreement is generally satisfactory, particularly between our assignments and those of Ref. 63. In the following discussion, for convenience, the energies of transitions

Table I. Comparison of excitation energies for levels of ^{54}Fe. The energies are given in keV.

Present experiment	Sperduto and Buchner; (p,p') Ref. 63*	Aspinall et al. (p,p') Ref. 62*	Hansen et al. (d,d') Ref. 64	Wegener Decay of ^{54m}Co Ref. 65
1408 ± 1	1409 ± 4	1408 ± 4	1410 ± 4	1408 ± 1
	2534 ± 5		2537 ± 6	
2539 ± 1	2540 ± 6	2540 ± 4	2550 ± 6	2537 ± 2
2948 ± 2				2948 ± 3
2961 ± 2	2959 ± 5	2961 ± 4	2959 ± 6	
3163 ± 2	3164 ± 5	3161 ± 4	3167 ± 8	
3298 ± 2	3296 ± 5	3291 ± 4		
3345 ± 2	3345 ± 5	3340 ± 4	3349 ± 8	
3836 ± 2	3838 ± 5	3829 ± 4		
4037 ± 3		4029 ± 4		
4048 ± 2	4048 ± 5	4047 ± 4		
4072 ± 2	4074 ± 5	4070 ± 4		
4271 ± 3		4265 ± 4		
4290 ± 3		4287 ± 4		
4583 ± 2		4579 ± 4		
4655 ± 3		4656 ± 4		
4702 ± 3		4700 ± 4		
4787 ± 3		4781 ± 4		
4950 ± 3		4949 ± 4		

*Only random errors are quoted for these numbers.

from levels below 4.2 MeV are referred to by the energies determined from the numbers of Ref. 63; those above this point are derived from Ref. 62. Thus the excitation energies from our work appear only in Table I.

D. RESULTS

1. Detailed Spectroscopic Information

This section is devoted to a presentation of the angular correlation and lifetime information obtained for each excited state. In Sec. IV.D-2, all of the electromagnetic transition data, that is, lifetimes, multipole mixing and branching ratios, are summarized in Tables II-V. In the summary and in the discussion previous to it, we have referred to electric and magnetic reduced transition strengths in terms of Weiskopf Units (WU); the values given by Wilkinson[66] have been used.

1.409-MeV State. The gamma-coincidence spectrum of the first excited state at 55° is shown in Fig. 22 (all succeeding coincidence spectra illustrated are at this angle). The BE2 of the $2^+ \rightarrow 0^+$ transition has been measured by Coulomb excitation[67] and by electron scattering and thus affords a test of the Doppler-shift analysis. A comparison of the BE2's is given below:

Measurement	$BE2(e^2 f^4)$
Coulomb excitation	102 ± 4
electron scattering	104 ± 6
Doppler shift	$131 {}^{+50}_{-32}$

The measured lifetime of 1.1 psec is near the limit of sensitivity of the DSAM, resulting in rather large errors; within the limits, the agreement

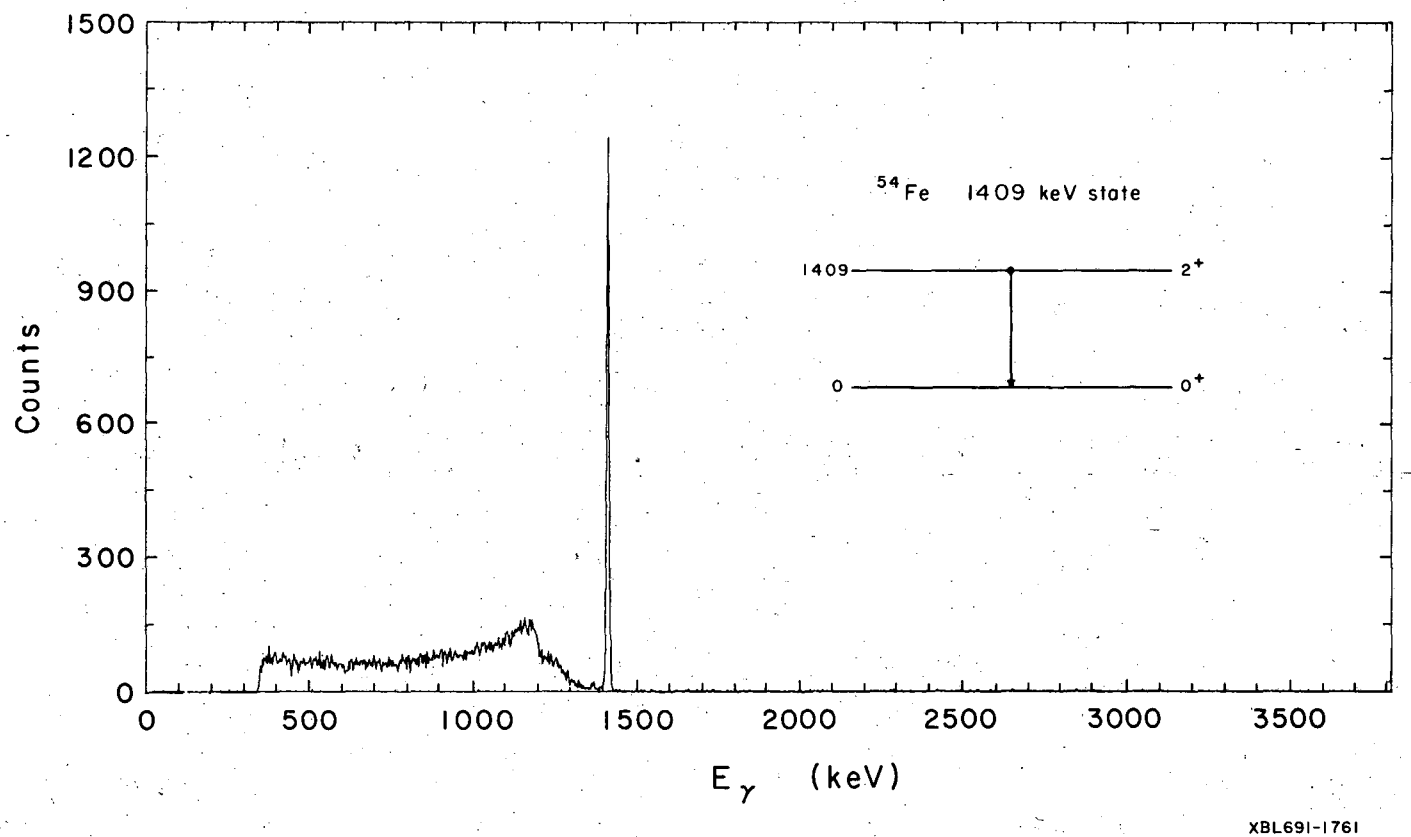

Fig. 22. Gamma-ray coincidence spectrum for the 1.409-keV 2_1^+ state of ^{54}Fe at θ_γ = 55 deg.

is satisfactory. Using the BE2 from Coulomb excitation, the transition strength is 8.4 WU and is thus collectively enhanced.

2.540 and 2.564-MeV States. The gamma coincidence spectrum for these states which are unresolved in the proton spectrum is shown in Fig. 23; no evidence is seen for another state in this energy region.[63,64] On the basis of the decay of ^{54m}Co, Sutton et al.[69] first suggested that the 2.540-MeV level was the 4^+ member of the $(f_{7/2})^2$ proton configuration; several (p,p') and (α,α') experiments are in agreement with this assignment, but are themselves ambiguous in part because of the presence of the unresolvable 2.564-MeV state. More recently, Wegener[65] re-examined the decay of ^{54m}Co, using (γ,γ) angular correlation techniques and was able to assign J^π of 4^+ to the 2.540-MeV state and J^π of 6^+ to the 2.948-MeV state. The results of the present angular correlation analysis are shown in Fig. 24; it is seen that only J = 4 gives a solution, thus confirming the assignment of Wegener.

The 2.564-MeV state is known to be a 0^+ from the work of Church et al;[57] this assignment was first suggested by Belote et al.[70] Figure 19 shows that the angular distribution of the $0^+ \rightarrow 2^+$ gamma ray from this state is isotropic, as expected.

Both the $4_1^+ \rightarrow 2_1^+$ and the $0_2^+ \rightarrow 2_1^+$ gamma rays show very small Doppler shifts; thus it can be said only that their lifetimes are longer than 3 psec and 2 psec, respectively.

2.948 and 2.959-MeV States. The coincidence spectrum of these states is shown in Fig. 25. The 2.948-MeV state is known to have J^π of 6^+ from the work of Wegener.[65] The angular distributions of $6^+ \rightarrow 4^+$,

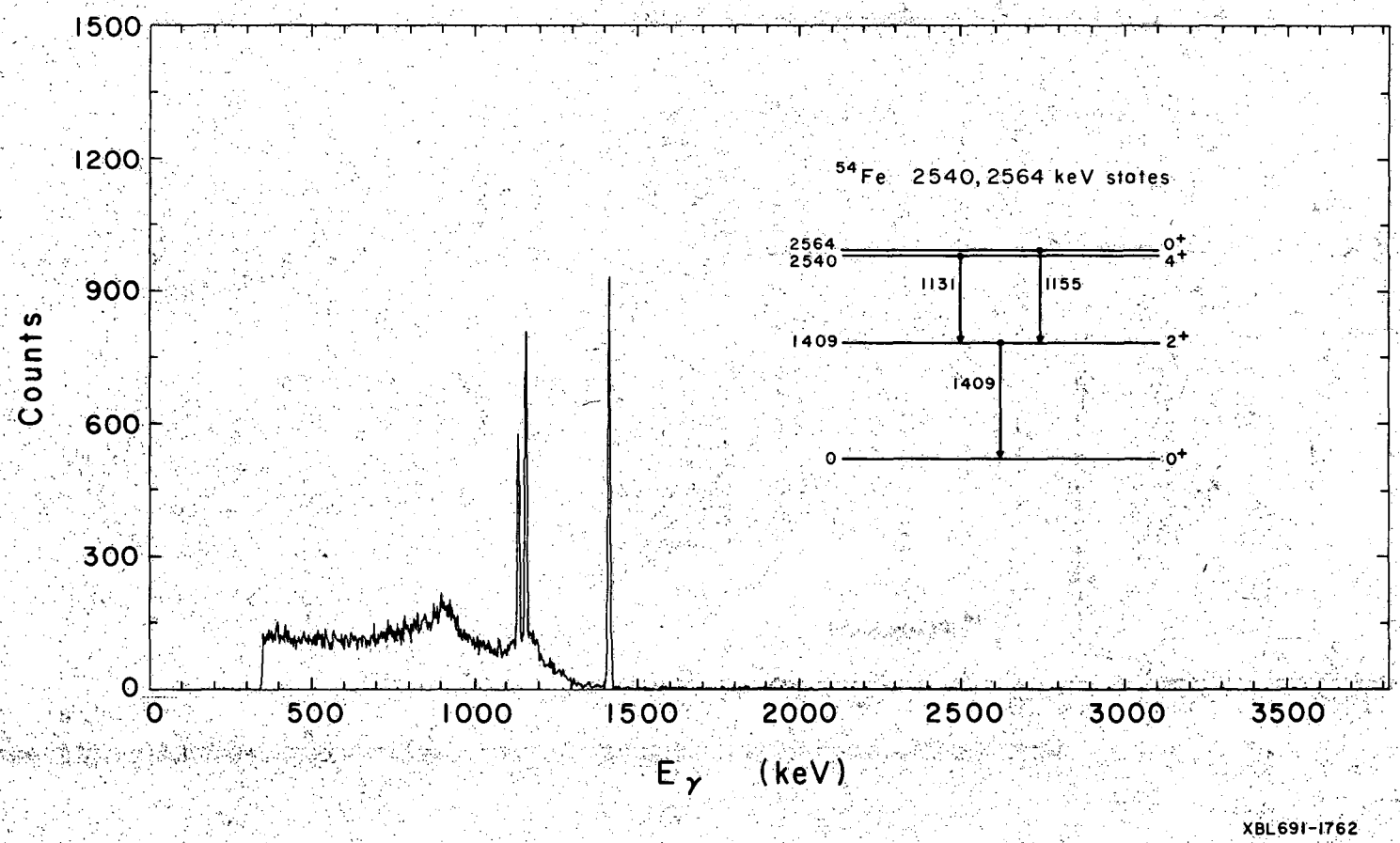

Fig. 23. The gamma-ray coincidence spectrum for the 2540, 2564-keV states (unresolved in the proton spectrum) of ^{54}Fe at θ_γ = 55 deg.

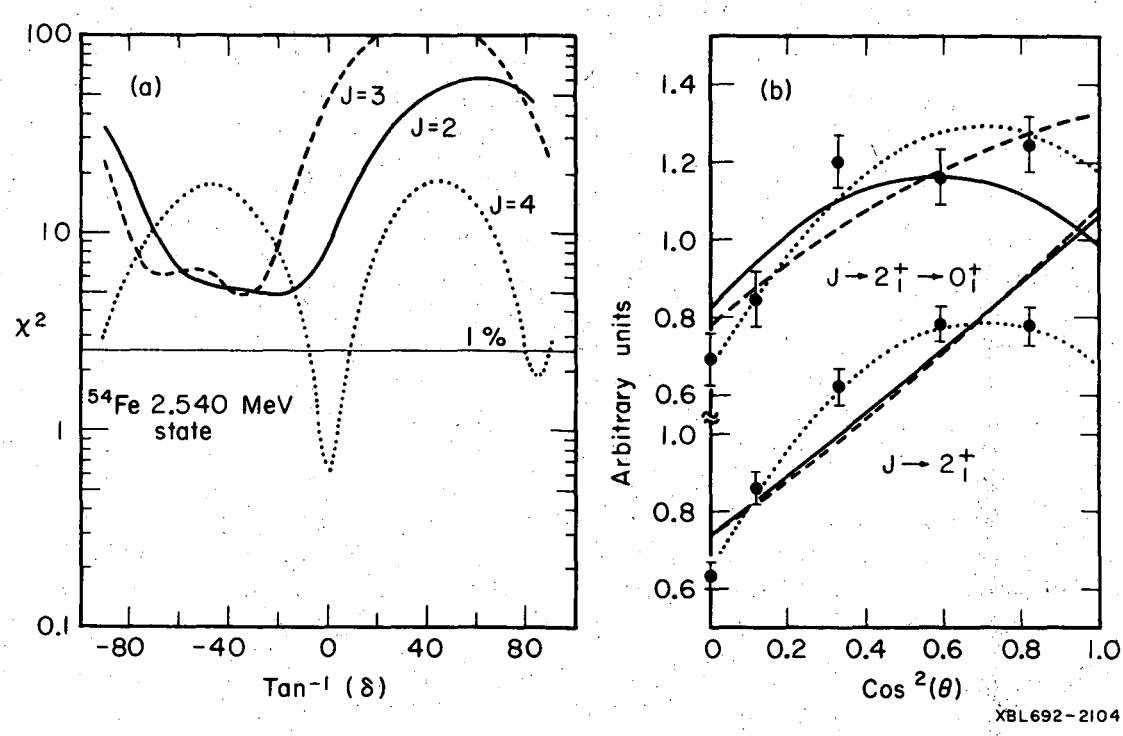

Fig. 24. χ^2 versus $\tan^{-1}(\delta)$ for the 2.540-MeV state of ^{54}Fe and the best fits to the experimental angular correlations for each initial spin. The $J_i \rightarrow 2_1^+$ and $2_1^+ \rightarrow 0_1^+$ angular correlations were analyzed simultaneously. For a correct spin solution χ^2 should be near unity.

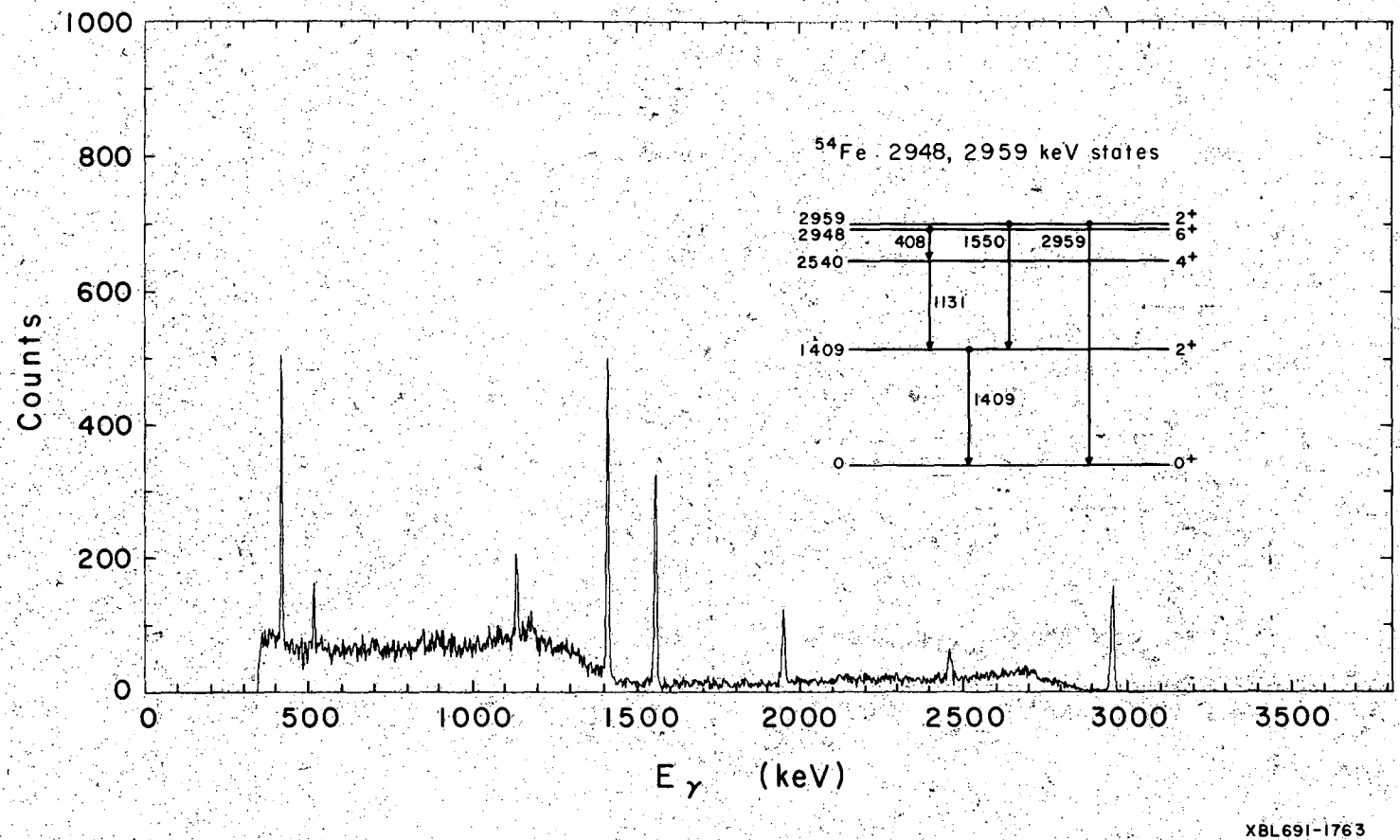

Fig. 25. Gamma-ray coincidence spectrum for the 2948 and 2959-keV states of ^{54}Fe (unresolved in the proton spectrum) at θ_γ = 55 deg.

$4^+ \rightarrow 2^+$ transitions obtained here were consistent with this assignment, but due to poor statistics, other initial spins also gave solutions.

The 2.959-MeV state was assigned J^π of 2^+ from the work of Thomas et al.[16] The simultaneous fitting of both the 1.550-MeV $2_2^+ \rightarrow 2_1^+$ and the 2.959-MeV $2_2^+ \rightarrow 0_1^+$ angular distributions from this experiment yielded a value of $\delta(2_2^+ \rightarrow 2_1^+) = 0.105^{+0.040}_{-0.042}$. This is in reasonable agreement with the value $\delta = 0.25 \pm 0.19$ obtained by Thomas et al.[16,71] The analysis in the latter reference ruled out a second solution of $\delta = -3.3$, found in the present work.

Figure 26 shows a summary of the Doppler shift analysis for the 2.959-MeV level, which gave a mean lifetime of 0.075 ± 0.012 psec; this is an average of the values obtained from the 0.550 and 2.959-MeV gamma rays. Combining the lifetime determination with the branching ratio for the 2.959-MeV transition yeilds a BE2 of $27.2 \pm 4.5\ e^2f^4$. This is in poor agreement with the (e,e') experiment of Ref. 68, where the value $45 \pm 5\ e^2f^4$ was obtained. However, since the resolution in the (e,e') experiment was 700 keV, the 2.959-MeV level was not resolved from the other states nearby and thus the BE2 may be overestimated.

<u>3.164-MeV State</u>. The gamma coincidence spectrum (Fig. 27) shows that this level decays to both the ground state and to the 2_1^+. It has been assigned a J^π of 2^+ by Thomas et al.[16] The mixing ratio for the $2_3^+ \rightarrow 2_1^+$ transition is poorly fixed in our analysis; it is clear, however, from the value $\delta = 0.63^{+0.57}_{-0.25}$ that there is strong E2 competition in the transition. The results of the Doppler shift analysis (shown in Fig. 21) gave a mean lifetime for this level of $0.23^{+0.05}_{-0.04}$ psec. This corresponds

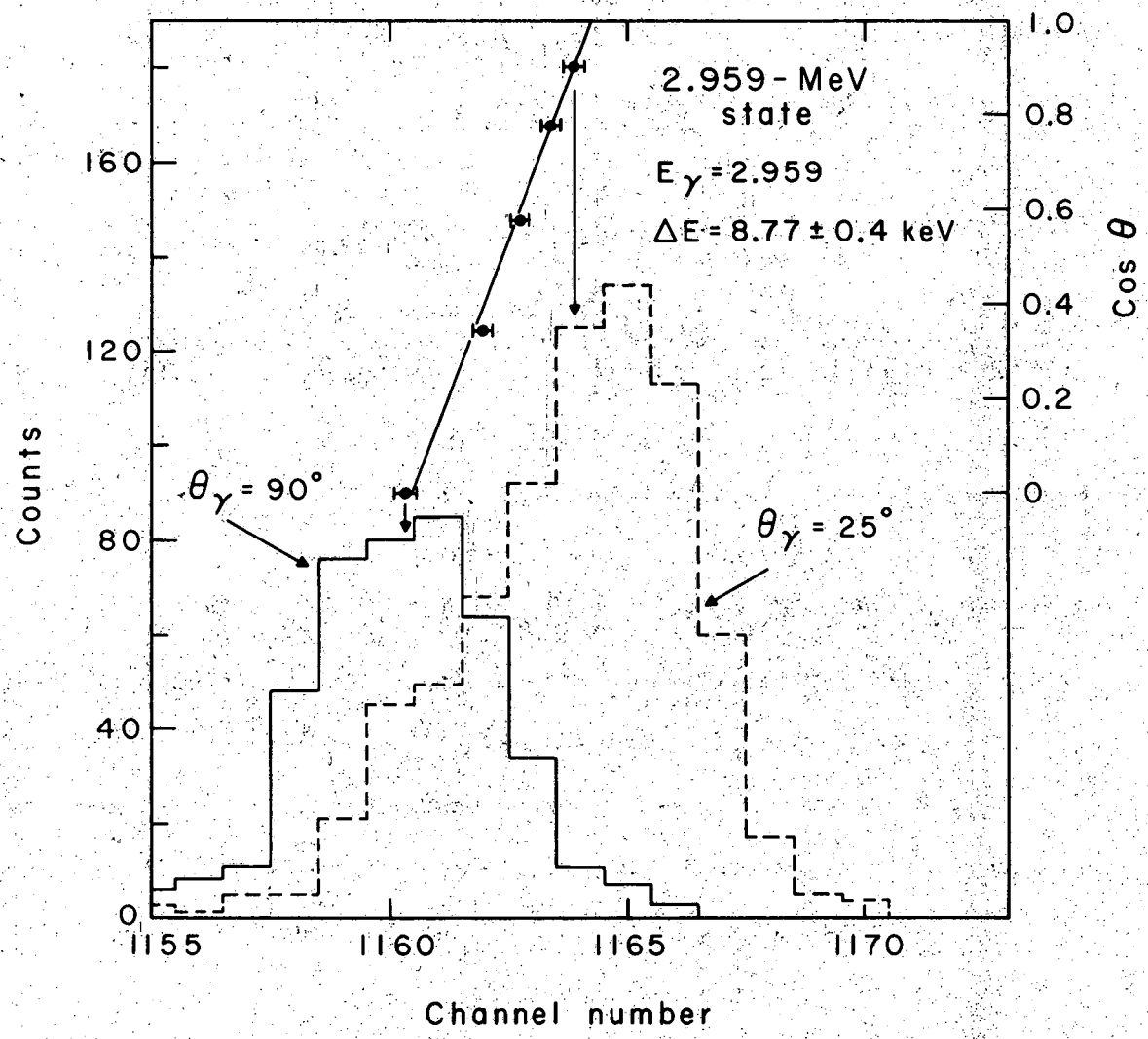

XBL693-2235

Fig. 26. Summary of the Doppler shift analysis for the 2.959-MeV state (2.959-MeV gamma ray). The FE gamma ray peaks at θ_γ = 90 deg and θ_γ = 25 deg are shown. Shown on the same channel scale is the best fit line to the centroids of all five gamma angles. The form of the line was $E_0 + \Delta E_{obs} \times \cos\theta_\gamma$.

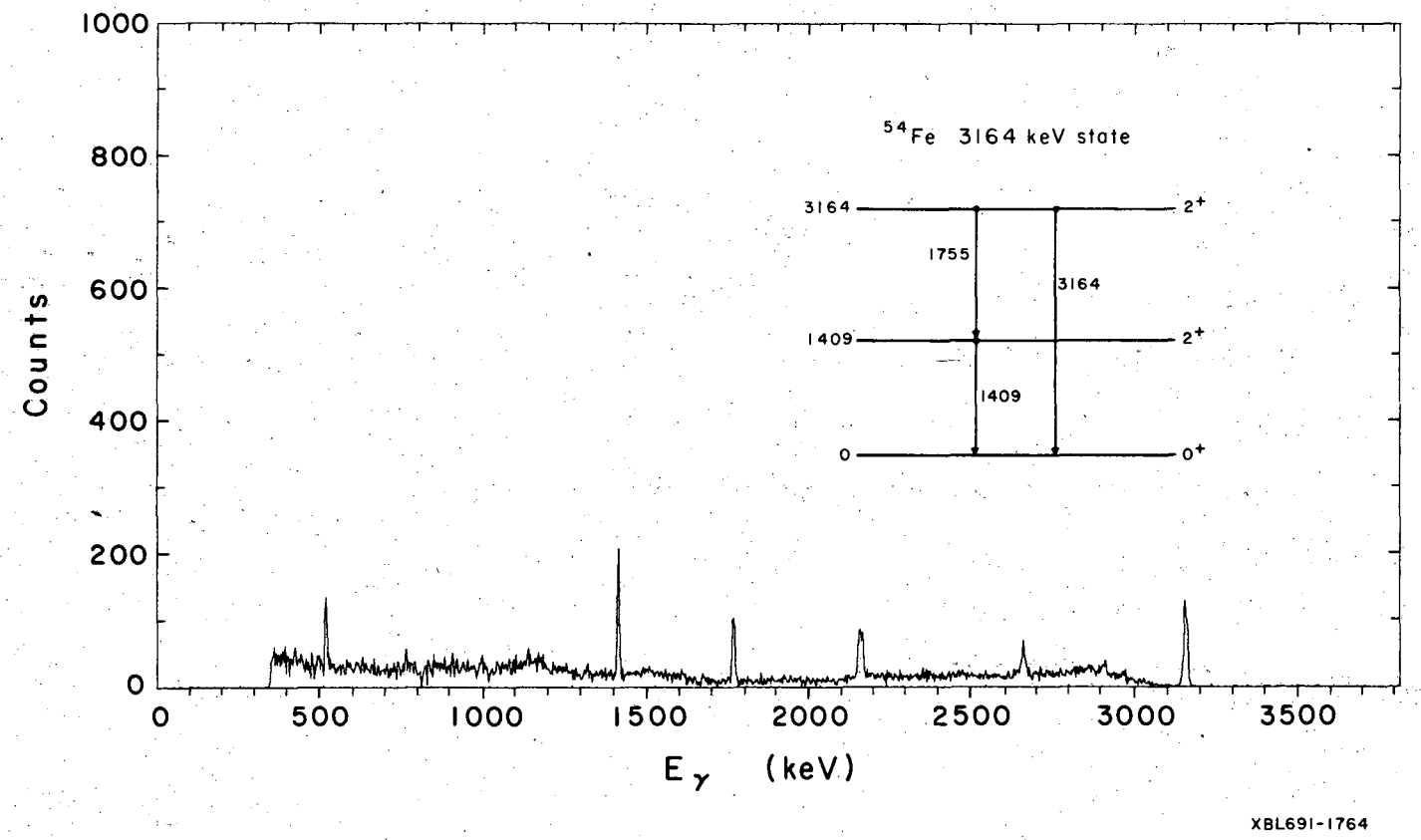

Fig. 27. Gamma-ray coincidence spectrum for the 3164-keV state of ^{54}Fe at θ_γ = 55 deg.

to a $2_3^+ \rightarrow 0_1^+$ transition strength which is slightly retarded with respect to the single particle estimate (0.73 WU).

3.296 and 3.345-MeV States. Figure 28 shows the gamma coincidence spectrum from the 3.296, 3.345-MeV doublet. Neither state has been assigned a spin from previous work. The angular correlation analysis for the 756-keV and 1887-keV transitions from the 3.296-MeV state is shown in Fig. 29. The curves shown are as follows: for J = 2 the variable shown is $\delta(2 \rightarrow 2)$ with $\delta(2 \rightarrow 4) = 0$; for J = 3 the variable is $\delta(3 \rightarrow 4)$, with $\delta(3 \rightarrow 2) = -0.55$, and for J = 4 the variable displayed is $\delta(4 \rightarrow 4)$, with $\delta(4 \rightarrow 2) = 0$. These curves show the best solutions obtainable for each initial spin; spins less than 2 and greater than 4 were eliminated on the basis of the observed branches to states of spin 2 and 4. It is seen that spin 2 is eliminated, but spins 3 and 4 are allowed. An attempt was made to resolve the ambiguity by including the cascade $4_1^+ \rightarrow 2_1^+$ transition in the analysis. However, since the 3.345-MeV state also decays to the 4_1^+, the uncertainty in subtracting out its contribution to the transition was too large to allow distinction between a $3 \rightarrow 4 \rightarrow 2$ and a $4 \rightarrow 4 \rightarrow 2$ sequence. Furthermore, no transition to this state from higher lying levels of known spin distinguished between spin of 3 or 4. The Doppler shift of the $3.296 \rightarrow 1.409$ transition was quite small, indicating only that the lifetime of this state is longer than 3 psec.

The results of the angular correlation analysis for the 3.345-MeV state are shown in Fig. 30. The following mixing ratios were held constant at the values given: for J = 2, $\delta(2 \rightarrow 4) = 0$; for J = 3, $\delta(3 \rightarrow 2) = -0.81$; and for J = 4, $\delta(4 \rightarrow 2) = 0$. It is seen that only

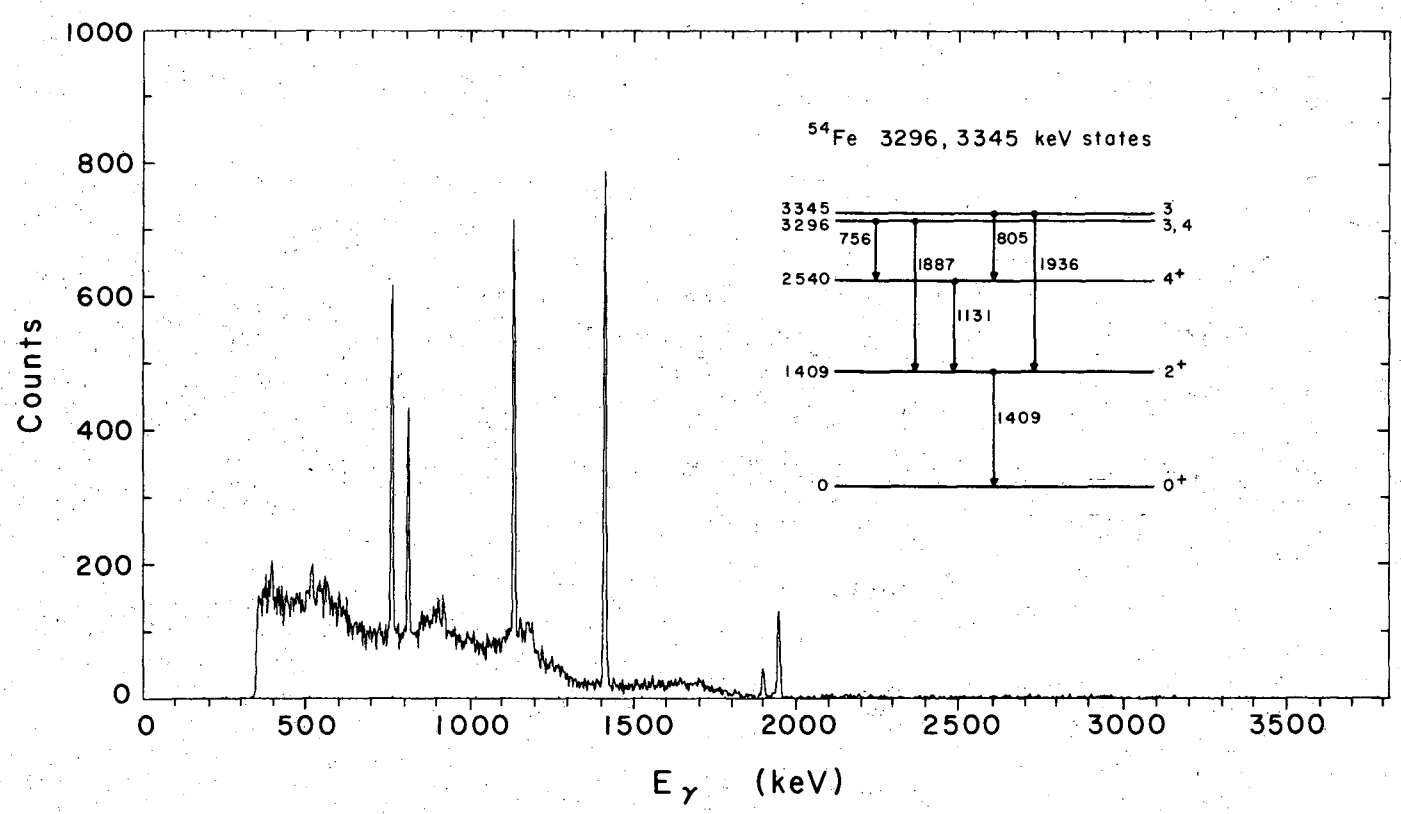

XBL691-1765

Fig. 28. The gamma-ray coincidence spectra for the 3296 and 3345-keV states of ^{54}Fe (unresolved in the proton spectrum) at θ_γ = 55 deg.

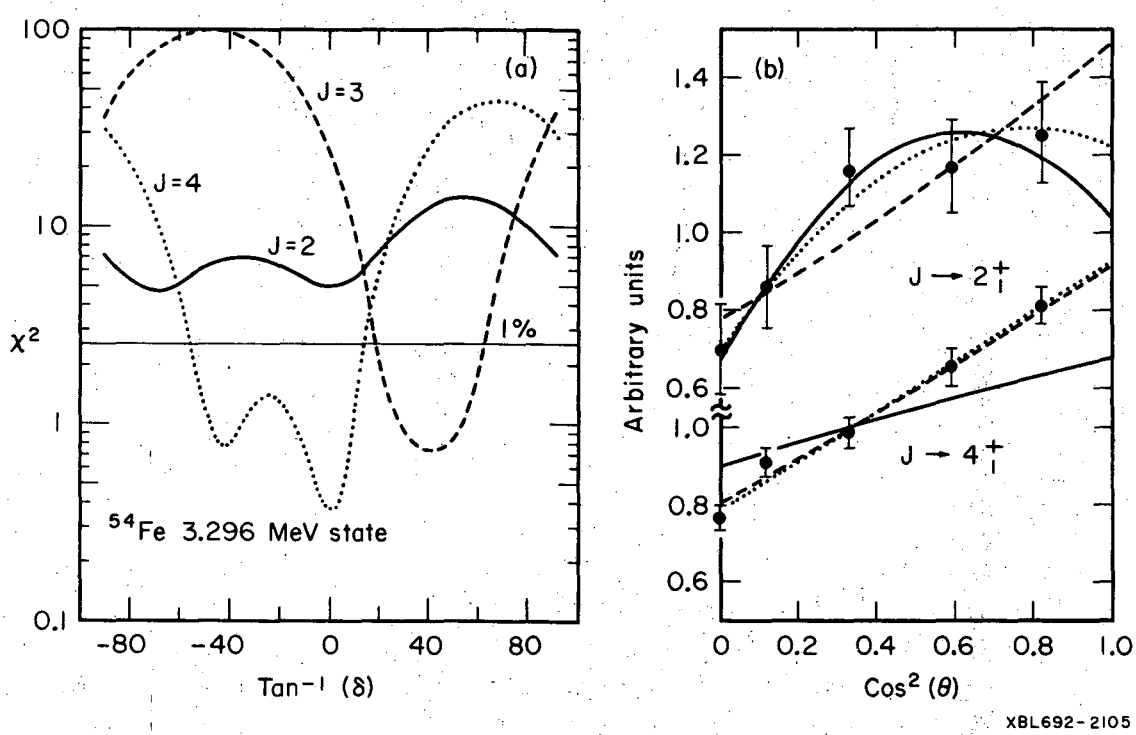

Fig. 29. χ^2 analysis for the 3.296-MeV state of ^{54}Fe and best fits to the experimental angular correlations for each initial spin. The $J_i \rightarrow 4_1^+$ and $J_i \rightarrow 2_1^+$ angular correlations were fitted simultaneously. The variables displayed explicitly are as follows: for $J_i = 4$, $\delta(4 \rightarrow 2) = 0$ and $\delta(4 \rightarrow 4)$ is shown; for $J_i = 3$, $\delta(3 \rightarrow 2) = -0.55$ and $\delta(3 \rightarrow 4)$ is shown; for $J_i = 2$, $\delta(2 \rightarrow 4) = 0$ and $\delta(2 \rightarrow 2)$ is shown.

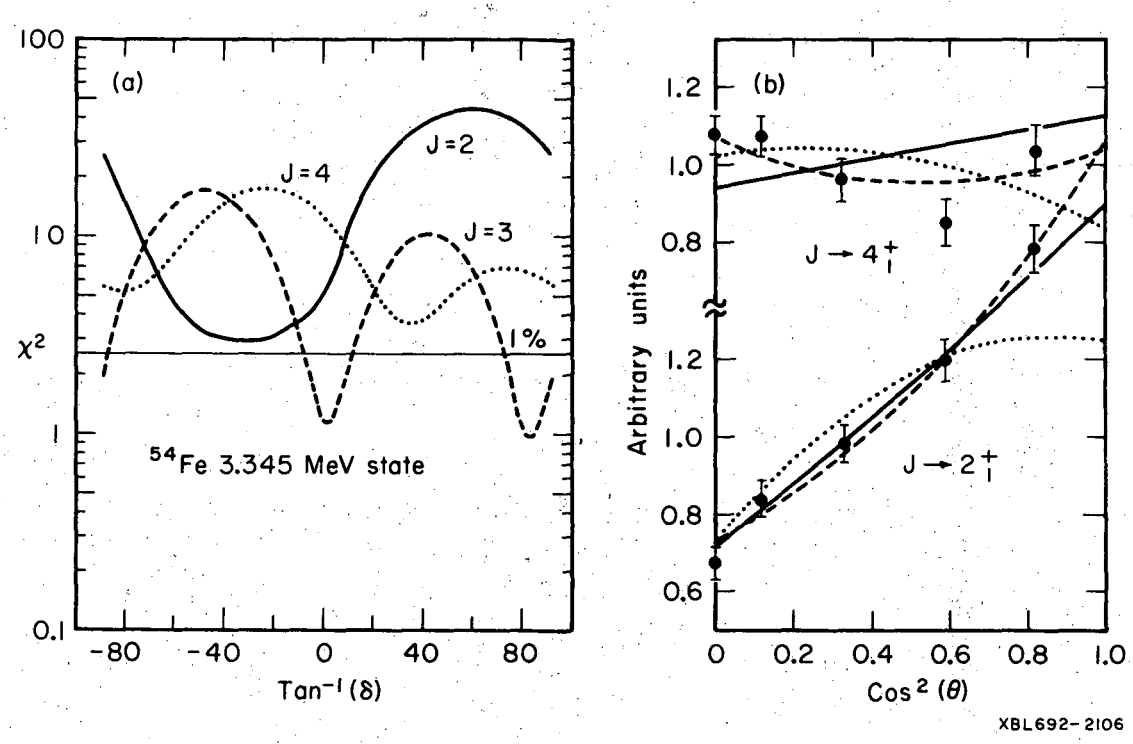

Fig. 30. χ^2 analysis for the 3.345-MeV state of ^{54}Fe and best fits to the angular correlations for each initial spin. The $J_i \rightarrow 4_1^+$, and $J_i \rightarrow 2_1^+$ angular correlations were analyzed simultaneously. The variables displayed explicitly are as follows: for $J_i = 4$, $\delta(4 \rightarrow 2) = 0$ and $\delta(4 \rightarrow 4)$ is shown; for $J_i = 3$, $\delta(3 \rightarrow 2) = -0.81$ and $\delta(3 \rightarrow 4)$ is shown; for $J_i = 2$, $\delta(2 \rightarrow 4) = 0$ and $\delta(2 \rightarrow 2)$ is shown.

J = 3 gives a reasonable χ^2. The mixing ratio $\delta(3 \rightarrow 4)$ is confined to the values $\delta = 0 \pm 0.14$ or $\delta \geq 3.5$, while for the $3 \rightarrow 2_1^+$ transition, δ is confined to the range $-2.9 \leq \delta \leq -0.45$. A χ^2 below the 1% limit may be obtained for J = 2 if one allows $\delta(2 \rightarrow 4) \leq -0.04$; however, lifetime (limit set by the fast coincidence resolving time) and branching ratio arguments allow exclusion of any solution requiring a non-zero $\delta(l=3/l=2)$. The Doppler shift analysis for the 3.345-MeV state indicates a lifetime longer than 3 psec.

3.838-MeV State. Figure 31 shows the gamma coincidence spectrum for this state; it has been established as a 4^+ from the work of Thomas et al.[16] The state decays primarily via E2 radiation to the first 2^+ state; a weak branch is observed to the 2.540-MeV 4^+ state. Only slight evidence was seen for a branch to the 3.296-MeV state found by Thomas et al.[16] It was not possible to obtain a mixing ratio for the transition to the 2.540-MeV state, due to poor statistics. The lifetime of the 3.838-MeV level was determined to be 0.091 ± 0.002 psec from the DSAM. This analysis is summarized in Fig. 32. A rather large enhancement of 8.0 WU is found for the 2.429-MeV E2 transition.

4.029, 4.048, and 4.074-MeV States. This triplet was completely unresolved in the proton spectrum; thus, Fig. 33 is a composite gamma spectrum of the three states. The lowest member of the triplet decays mostly to the 3.296-MeV state; only a weak branch (seen only in the spectrum at $\theta_\gamma = 90°$) is observed to the 4^+ at 2.540 MeV. Due to the spin ambiguity in the final state, the 4.029 → 3.296-MeV transition does not give an unambiguous spin assignment to the 4.029-MeV level. The possible combinations are:

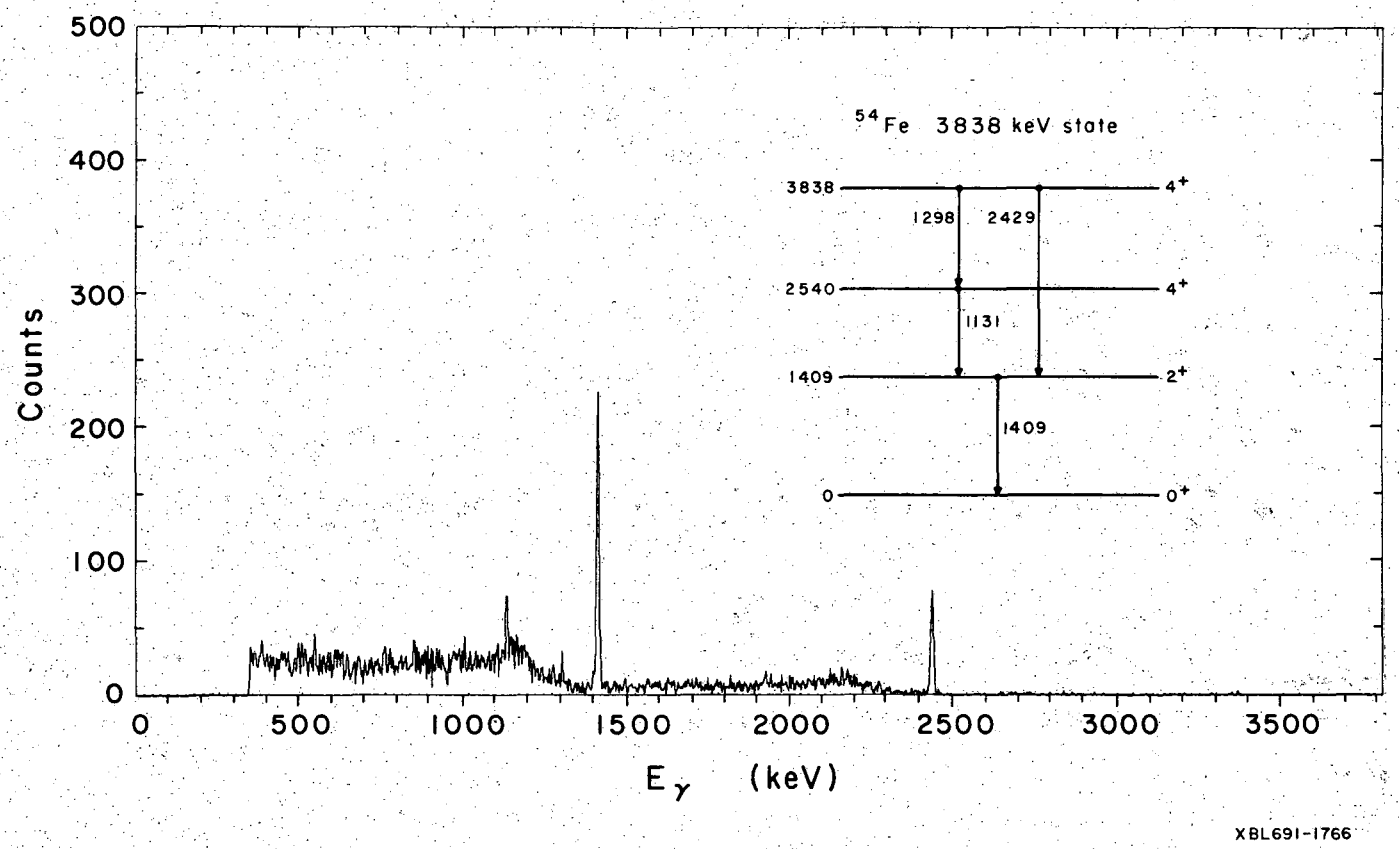

Fig. 31. Gamma-ray coincidence spectrum for the 3838-keV state of ^{54}Fe at θ_γ = 55 deg.

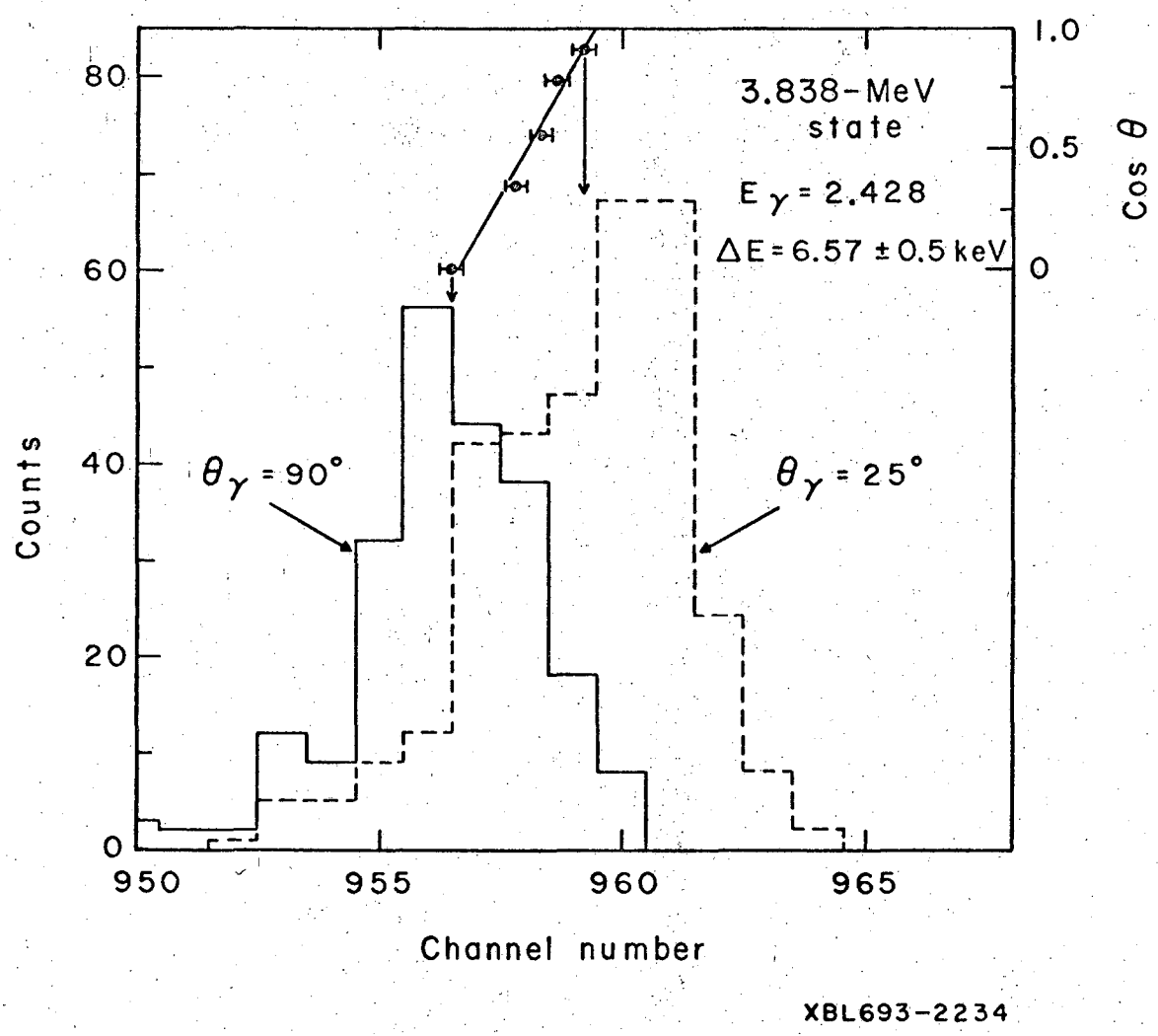

Fig. 32. Summary of the Doppler shift analysis for the 3.838-MeV state (2.429 MeV gamma ray). The FE gamma-ray peaks at $\theta_\gamma = 90$ deg and $\theta_\gamma = 25$ deg are shown. Shown on the same channel scale is the best fit line to the centroids of all five gamma angles.

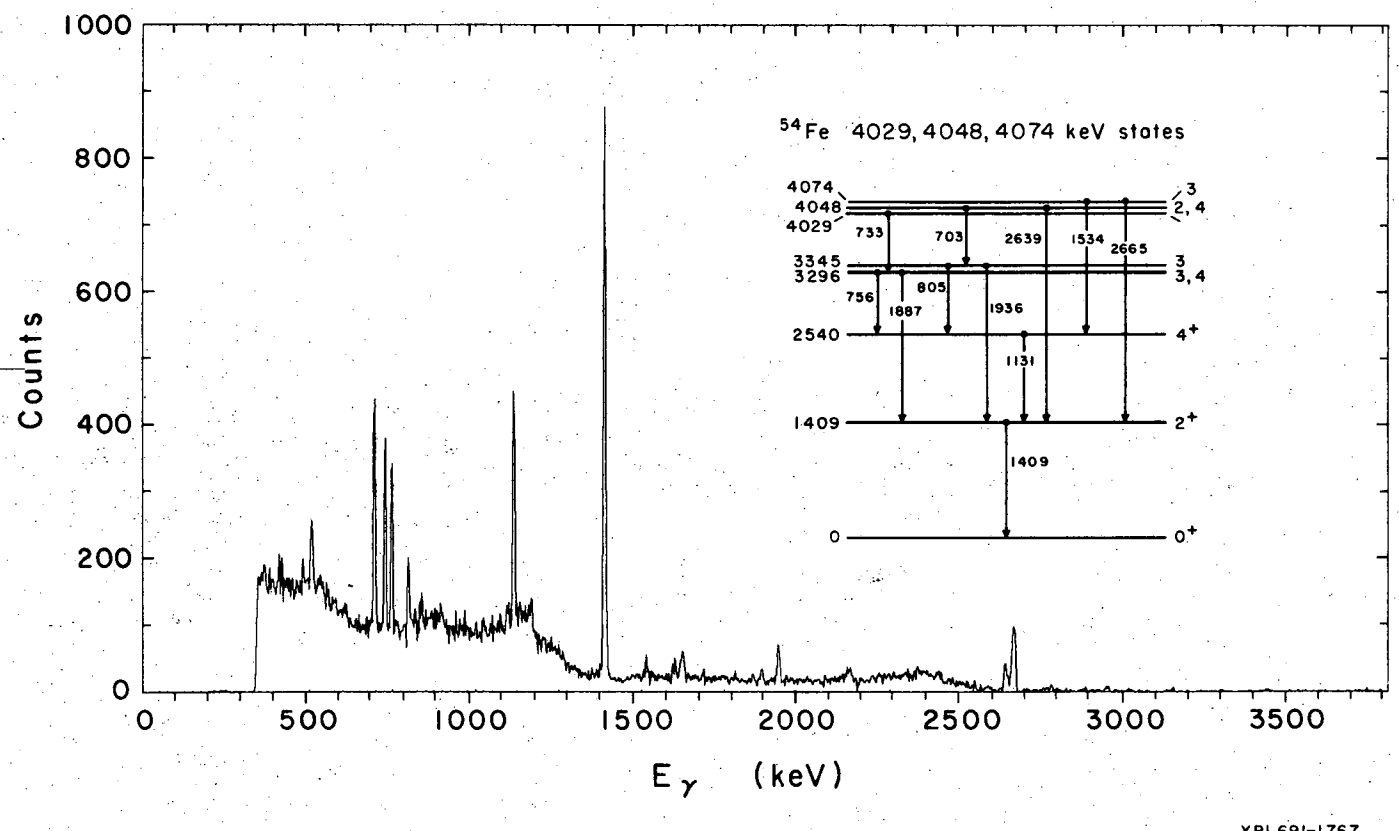

Fig. 33. Gamma-ray coincidence spectrum for the 4029, 4048, and 4074-keV states of ^{54}Fe (unresolved in the proton spectrum) at θ_γ = 55 deg.

$J_{4.029}$	$J_{3.296}$
3,5	4
2,4	3

On the basis of the observed decays of both states, the combination 4.029 (5) → 3.296 (4) is felt to be most likely. The absence of an observable Doppler shift indicates a lifetime longer than 0.6 psec for for 4.029-MeV state.

The 4.048-MeV state has strong branch decays to both the 1.409-MeV 2^+ and to the 3.345-MeV $3^{(+)}$; a very weak branch, seen only at $\theta_\gamma = 90°$, goes to the 2.540-MeV 4^+. The angular distribution analysis (Fig. 34) of the 703-keV transition indicates spin of either 2 or 4 for this level (the $J \rightarrow 2_1^+$ transition produces no additional information). Using the measured lifetime of $0.44^{+0.34}_{-0.15}$ psec and the branching and mixing ratios, plausible arguments may be given against a J = 2 assignment. The lack of an observable ground state decay gives an upper limit of 6% for the branching ratio. This gives a partial lifetime of 7.3 psec for the ground state decay, corresponding to an E2 transition of $\leq$ 0.01 WU. Such a decay is considerably more retarded than any observed E2 transition in ^{54}Fe (see Table V). (An M2 $2^- \rightarrow 0^+$ transition is unlikely because of the large mixing ratios observed in the other transitions.) Further evidence against a 2^+ assignment comes from the large mixing ratio observed for an assumed $2^+ \rightarrow 3^+$ transition. This gives a BE2 $\geq$ 26 WU, whereas a $4^+ \rightarrow 3^+$ transition is consistent with a more moderate BE2 (see Table V). Such arguments do not, of course, eliminate J = 2 rigorously; however, the evidence definitely favors J = 4.

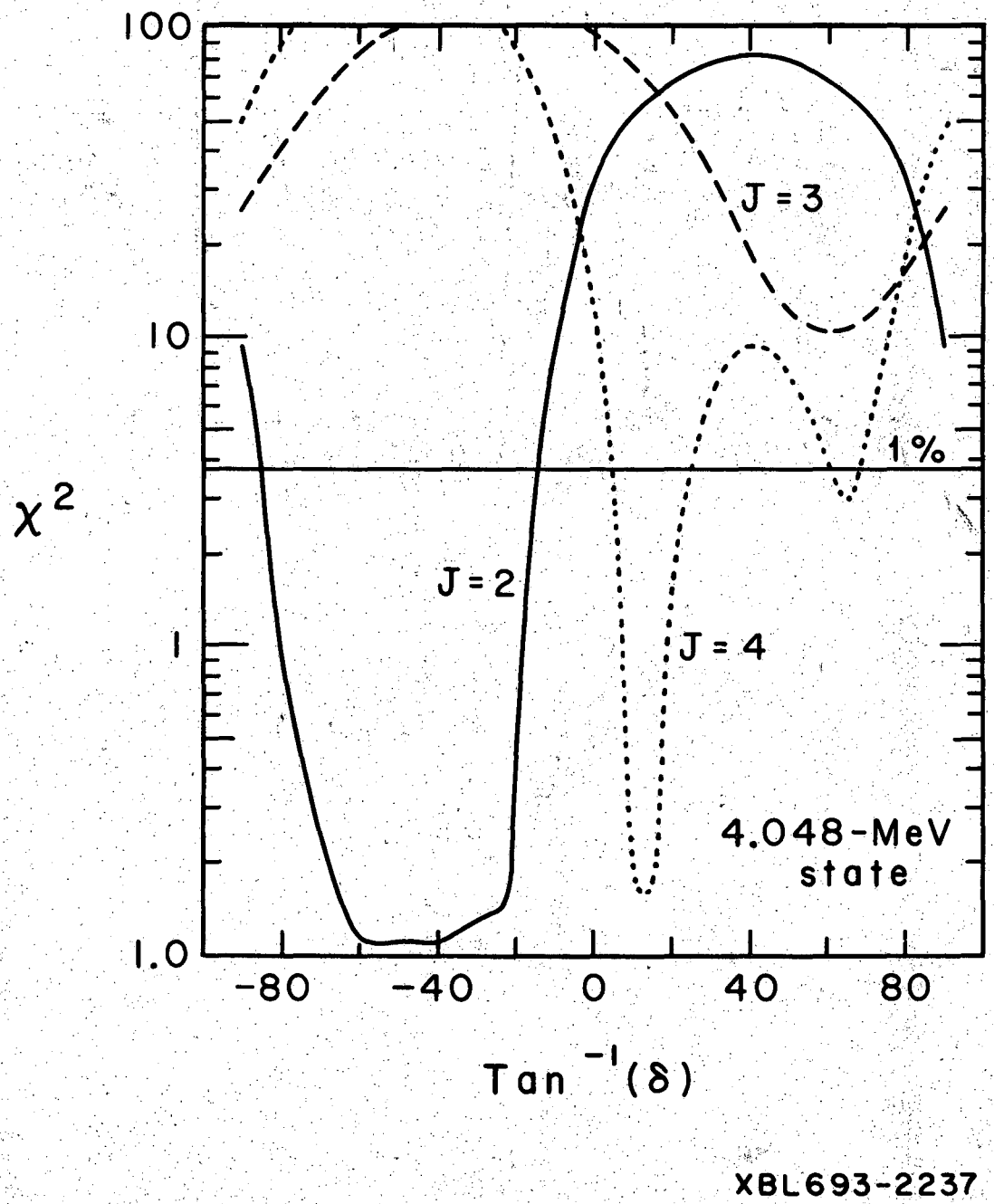

Fig. 34. χ^2 analysis for the 4.048-MeV state. The angular distribution of the 4.048 → 3.345-MeV gamma ray was analyzed.

The angular correlation analysis for the 4.074 to 1.408-MeV transition gives an unambiguous assignment of $J = 3^{(+)}$ to the 4.074 MeV state (Fig. 35). Assuming positive parity, the mixing ratio $\delta(E2/M1)$ is $1.88^{+0.50}_{-0.44}$. The $3^{(+)}$ to 4^+ transition is too weak to provide further information. Using the DSAM, the lifetime of this state was found to be 0.084 ± 0.025 psec.

4.265 and 4.287-MeV States. The gamma coincidence spectrum from this doublet is shown in Fig. 36. The analysis for the 4.265-MeV state is shown in Fig. 37(a); only the 1725-keV (4.287 → 2.540) transition was fitted. The cascade transition from the 4_1^+ could not be evaluated without large errors from background subtraction. J = 2 is rigorously eliminated because of the non-zero $\delta(L = 3/L = 2)$ required for a reasonable χ^2. Both J = 4 and J = 3 give χ's below the limit; however, the latter gives a rather poor fit and is thus less likely than J = 4. The observed Doppler shift of the 1725-keV transition gave a mean lifetime of $0.119^{+0.033}_{-0.025}$ psec for this level.

The 4.287-MeV level decays entirely to the first 2^+ state; the angular distribution of the transition is, within errors, isotropic, indicating a spin of 0. However, as may be seen in Fig. 37(b), spins of J = 1, 2, and 3 are not eliminated by the χ^2 analysis; in particular J = 1 can give a perfectly isotropic distribution, since the m = 0 and m = ± 1 substates can be equally populated. Again, one must appeal to plausibility arguments in order to determine the most likely spin. The measured lifetime and the upper limit of 8% for a transition to the ground state give the transition probabilities of 0.05 WU for a $2^+ \rightarrow 0^+(E2)$

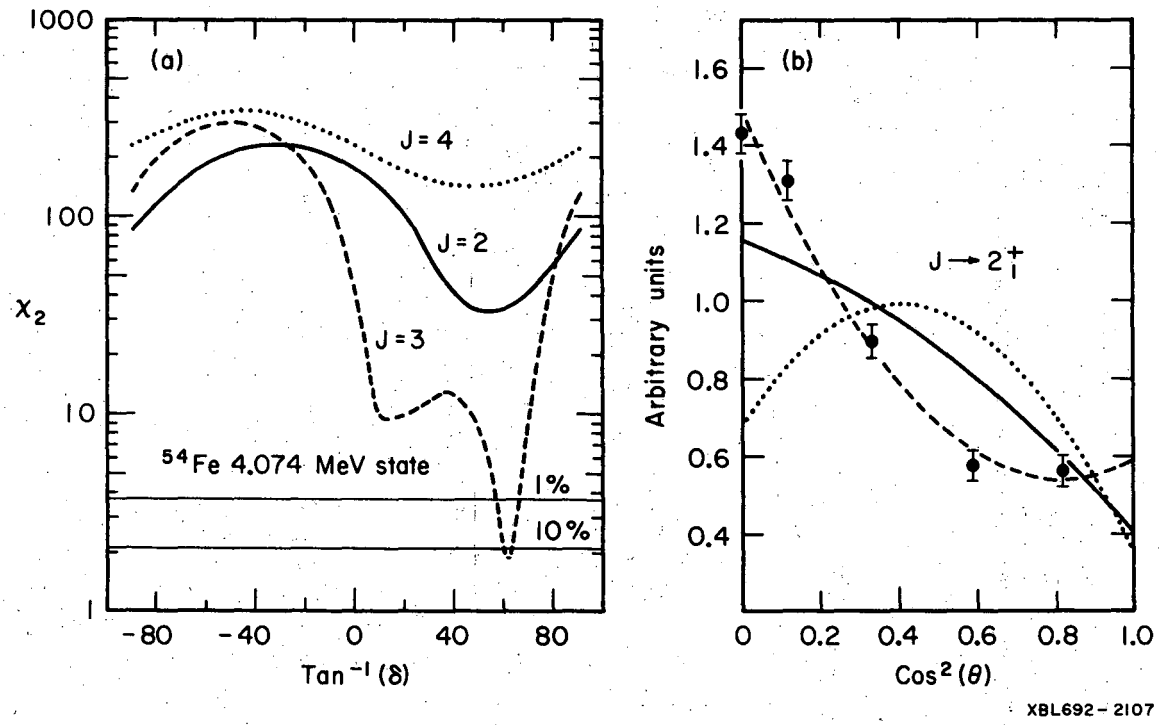

Fig. 35. χ^2 analysis for the 4.074-MeV state. The angular correlation of the 4.074 → 1.409 (2.665-MeV) gamma ray was fitted.

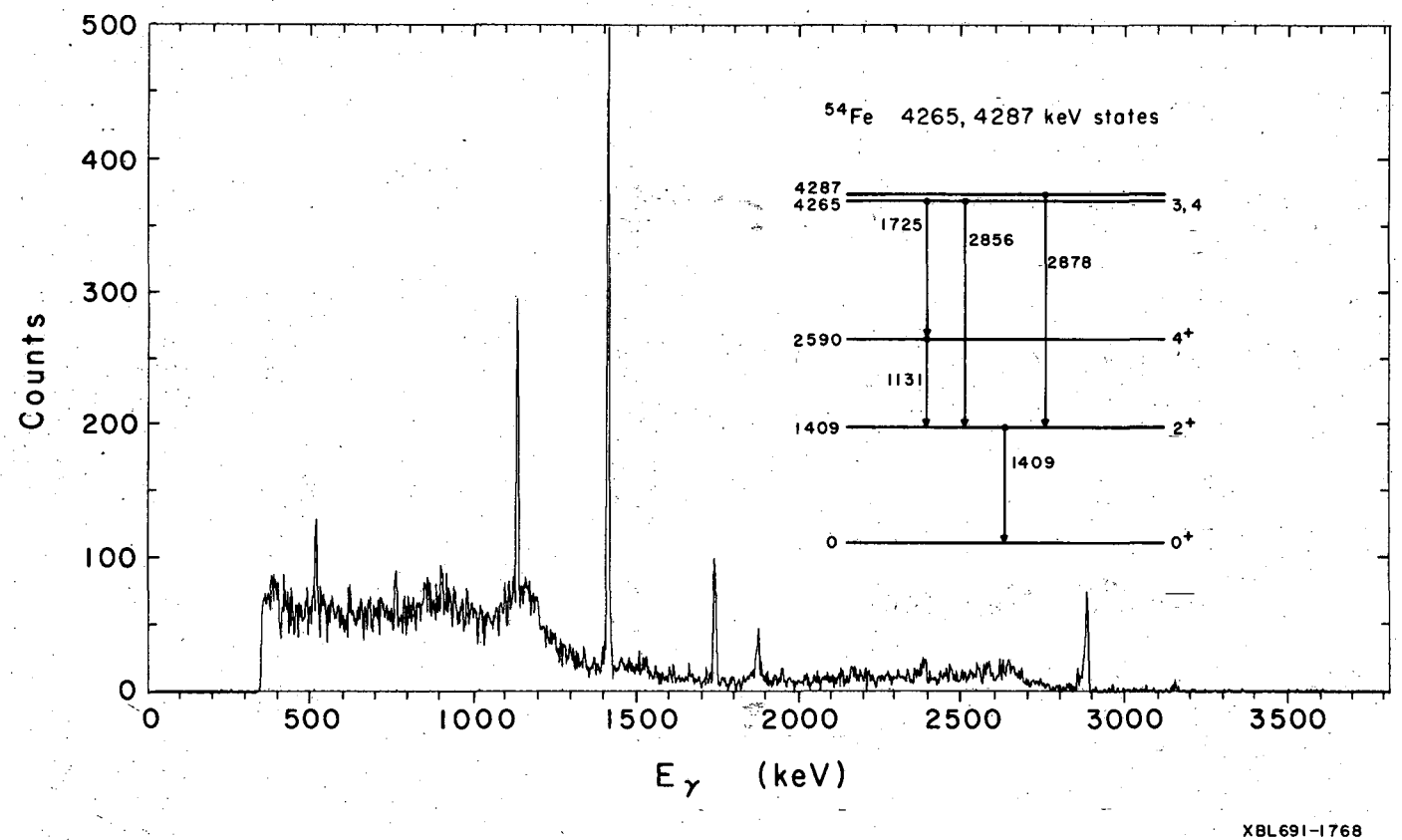

Fig. 36. Gamma-ray coincidence spectrum for the 4265 and 4287-keV states of ^{54}Fe (unresolved in the particle spectrum) at θ_γ = 55 deg.

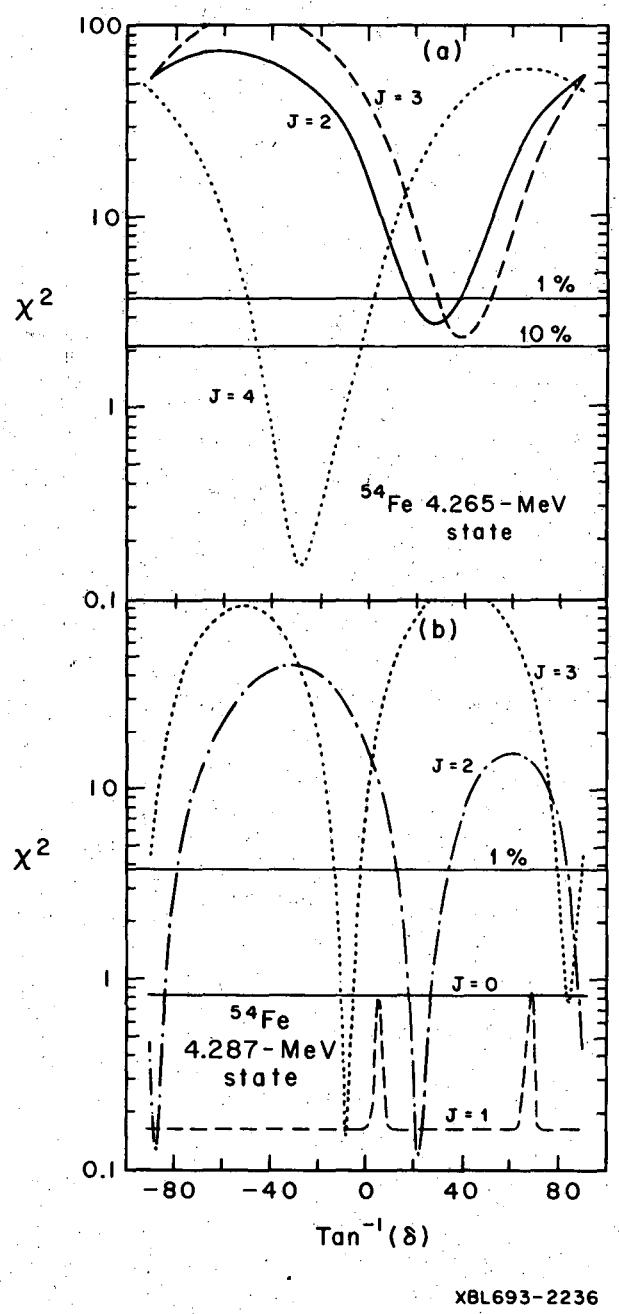

Fig. 37. (a) χ^2 analysis for the transition to the 2_1^+ state from the 4.265-MeV state.

(b) χ^2 analysis for the transition to the 2_1^+ state from the 4.287-MeV state.

decay and 5×10^{-4} WU for a $1^+ \rightarrow 0^+$ (M1) decay; both numbers are outside the observed range for this nucleus. Additional evidence for the assignment of J = 0 comes from the observed purity of the decay (i.e., only the $J \rightarrow 2_1^+$ transition is seen).

4.579, 4.656, and 4.700-MeV States. Limits were set in the proton spectrum to encompass most of this triplet; however, there was some contribution of the 4.700-MeV state in two different gamma spectra (see Fig. 38). The 4.579-MeV level was assigned J^π of 2^+ by Peterson,[15] using the $^{54}Fe(\alpha,\alpha')^{54}Fe$ reaction. From Fig. 39, it is seen that J = 2 is uniquely determined by analysis of the transitions from this state to the 0_1^+ and 2_1^+ states. Because the double-escape peak efficiency at 4.579 MeV is not well known, the error in the branching ratios for the two transitions are rather large. The observed Doppler shift for this state is, within errors, the maximum possible shift; thus the lifetime is $\leq$ 0.01 psec. The mixing ratio for the $2^{(+)}$ to 2_1^+ transition is either $\delta = -0.105 \pm 0.09$ or $\delta = -1.8^{+0.4}_{-0.5}$.

Within the present limit of sensitivity, the 4.656-MeV state decays only to the 3.296-MeV state; the 4.700-MeV state decays mostly to the 3.345-MeV $3^{(+)}$ state, with some evidence of a weak branch to the 2.540-MeV 4^+ state. The energies of the two strong gamma rays from these states are within 5 keV and are hence unresolvable. Thus, very little can be inferred about these levels; they are probably of rather high spin ($\geq$ 4).

4.781-MeV State. Figure 40 shows the gamma coincidence spectrum for this state; some contribution from the 4.700-MeV state is present.

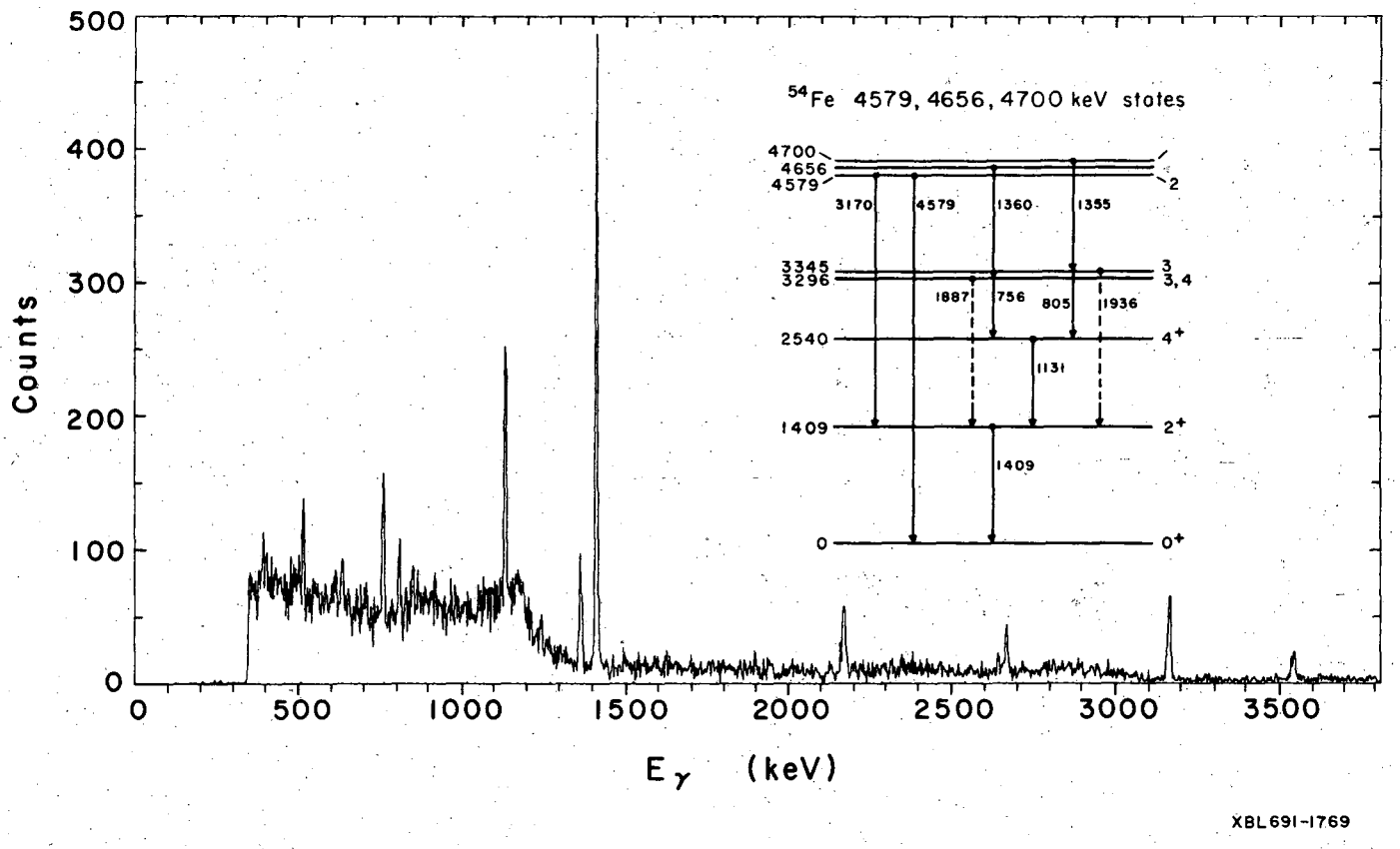

Fig. 38. Gamma-ray coincidence spectrum for the 4579, 4656, and 4700-keV states of ^{54}Fe (unresolved in the proton spectrum) at θ_γ = 55 deg.

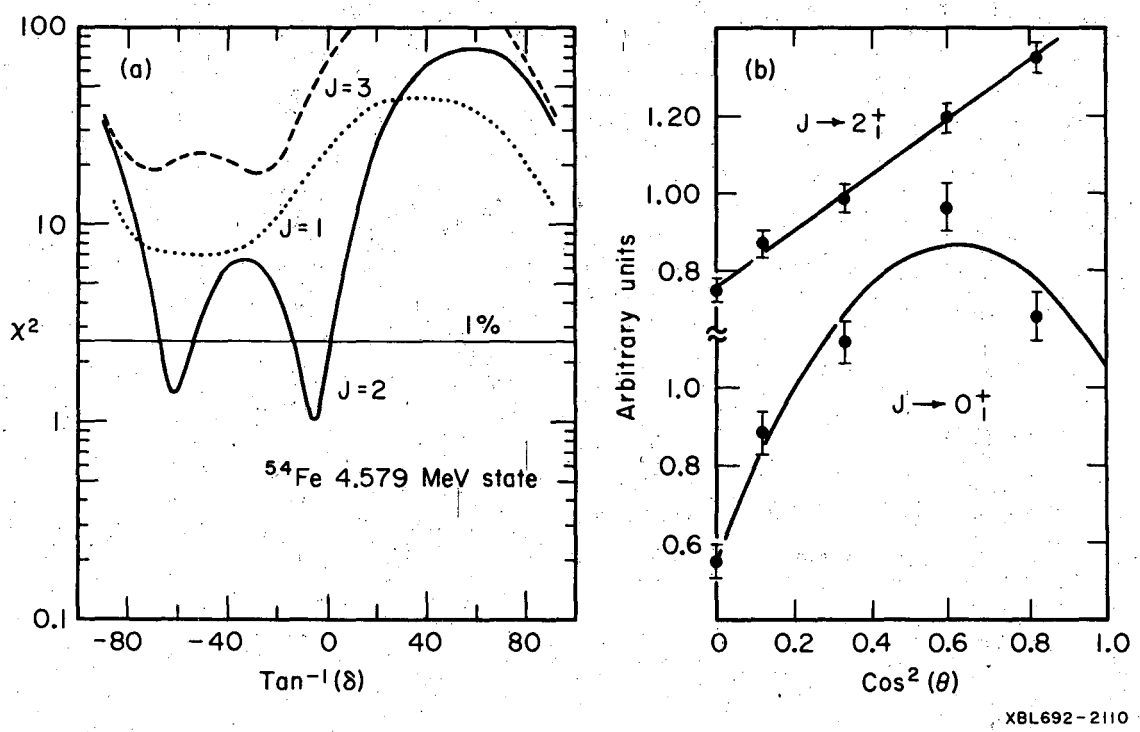

Fig. 39. χ^2 analysis for the 4.579-MeV state. The transitions to the 2_1^+ and to the ground state were analyzed simultaneously.

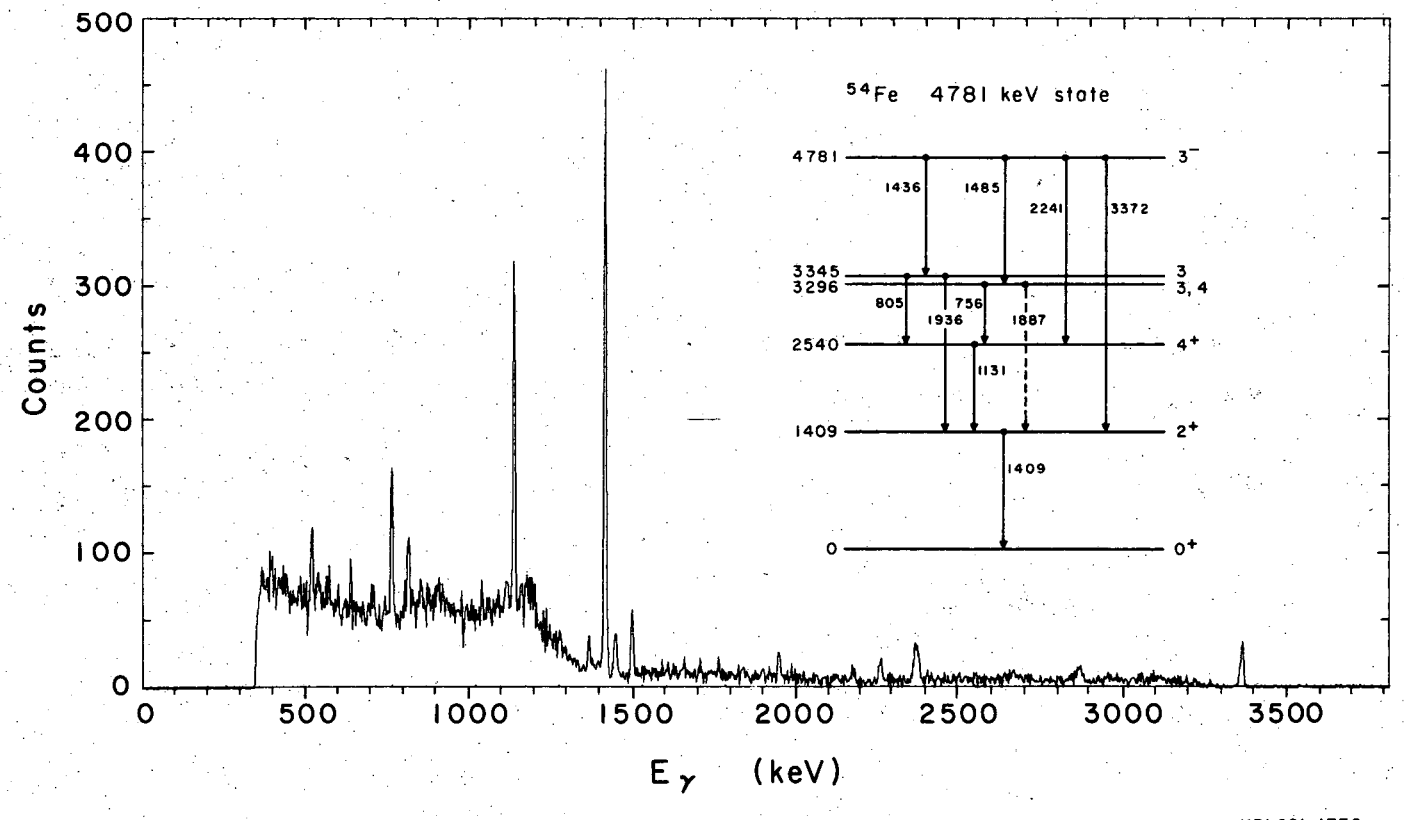

Fig. 40. Gamma-ray coincidence spectrum for the 4781-keV state of ^{54}Fe at $\theta_\gamma = 55$ deg. Some contribution is present from the 4700-keV state.

Bellicard and Barreau[68] have assigned J^{π} of 3^- to the 4.781-MeV level from electron scattering work. Several other (α,α')[15] and (p,p')[11-14] experiments have confirmed this choice. However, all these experiments depend upon a reaction model for interpretation and thus it was important to determine the spin of this state in a model independent way. Fitting only the 4.781 → 1.409 transition rules out spin 4, but both J = 2 and J = 3 are allowed. However, when the cascade $2_1^+ \rightarrow 0_1^+$ transition is included (see Fig. 41), only J = 3 gives a solution; the value of $\delta = 0$ is quite consistent with negative parity for this level. Because of the complex decay of the 3^- state, it was necessary to correct the $2_1^+ \rightarrow 0_1^+$ cascade transition for contributions other than 3 → 2 → 0. This could be done because most of the other contribution came from cascades through the 4_1^+ state. From the properties of cascades of the type $4^+ \xrightarrow{\gamma_1} 2^+ \xrightarrow{\gamma_2} 0^+$, it is known that γ_1 and γ_2 have identical angular correlations and thus such contributions to the $2^+ \rightarrow 0^+$ decay could be subtracted out. All but 10% of the required correction could be made in this manner; the remainder was felt to be negligible.

The Doppler shift analysis for both the FE and double-escape peaks of the 3.372-MeV gamma ray gives a mean lifetime of 0.048 ± 0.016 psec for this state. This corresponds to a very retarded BE1 of 1.99×10^{-4} WU for the $3^- \rightarrow 2_1^+$ decay. Retardations of this magnitude have been found for other $3^- \rightarrow 2^+$ transitions.[72]

<u>4.949-MeV State</u>. Although it is weakly excited and thus not visible in the singles proton spectrum, the 4.949-MeV level is cleanly separated in the coincidence array. Figure 42 shows the pure gamma decay

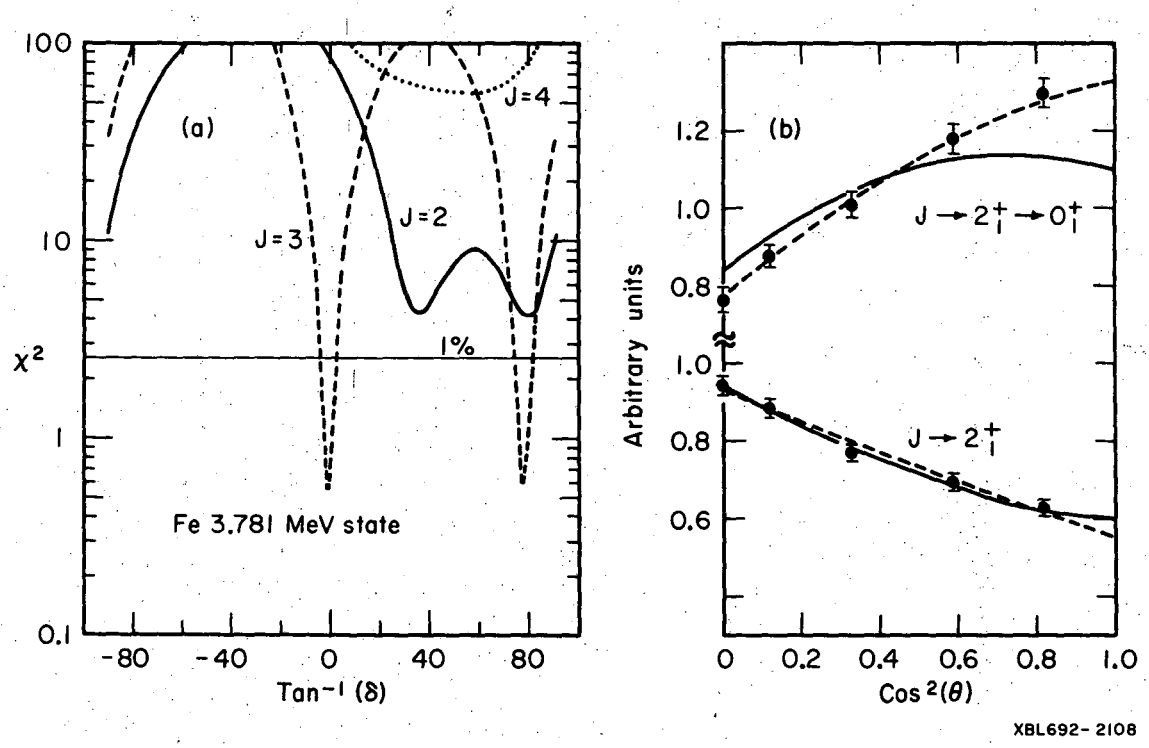

Fig. 41. χ^2 analysis for the 4.781-MeV state. The 4.781 → 2_1^+ and $2_1^+ \rightarrow 0_1^+$ cascade transitions were fitted simultaneously.

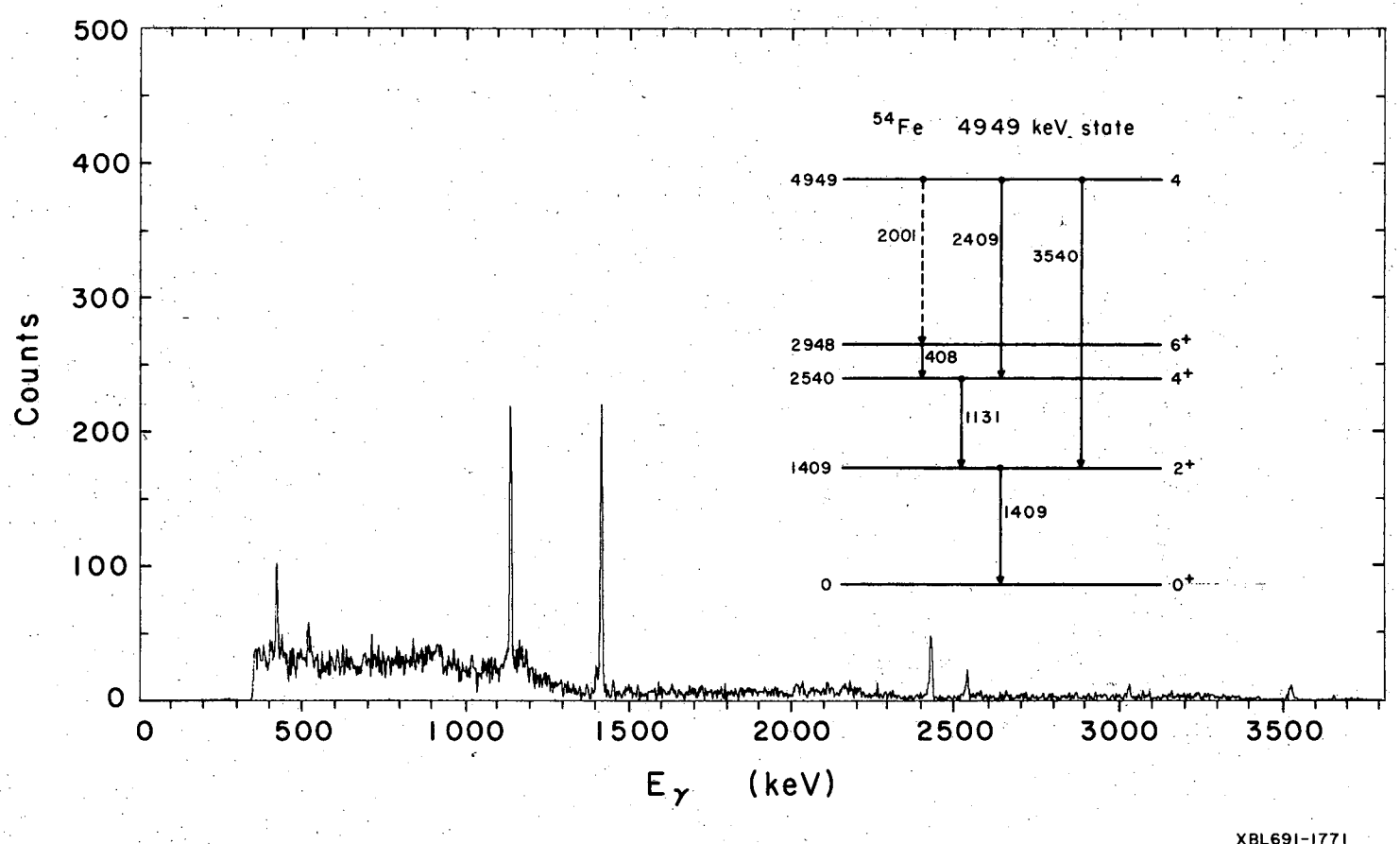

Fig. 42. Gamma-ray coincidence spectrum for the 4.949-keV state of ^{54}Fe at θ_γ = 55 deg.

spectrum for this state. Decay modes are seen to the 2_1^+, 4_1^+, and 6_1^+ states; although the latter is weak and thus not directly visible, the cascade $6_1^+ \rightarrow 4_1^+$ is strong, because of the high detection efficiency for the low energy gamma ray. The decay mode of the 4.949-MeV state is sufficient to assign it as $J^\pi = 4^{(+)}$; this is in agreement with the angular correlation analysis (Fig. 43). In Fig. 43, the mixing ratios are as follows: For J = 2, $\delta(2 \rightarrow 4) = 0$, $\delta(2 \rightarrow 2)$ is the variable; for J = 3, $\delta(3 \rightarrow 2)$ is optimized at -0.53 and $\delta(3 \rightarrow 4)$ is the variable; for J = 4, $\delta(4 \rightarrow 2) = 0$, and $\delta(4 \rightarrow 4)$ is the variable. The $4^{(+)} \rightarrow 4_1^+$ mixing ratio is found to be $\delta = -0.36^{+0.20}_{-0.29}$. The Doppler shift of the 2.409-MeV gamma ray yielded a mean lifetime of 0.042 ± 0.015 psec.

2. Summary of Electromagnetic Transition Data

Figure 44 summarizes the spin and decay information on levels of ^{54}Fe below 5 MeV; spin assignments from previous experiments are included. The branching ratio and multipole mixing ratio data are summarized in Table II and III. All transitions in which the minimum $|J_i - J_f| = 2$ had mixing ratios which were consistent with zero and hence are not listed in Table III. The agreement of the branching ratios determined here with those from other experiments is only fair, but within errors. There appears to be strong disagreement, however, between the multipole mixing ratio for the $2_3^+ \rightarrow 2_1^+$ determined here and that from the work of Thomas et al.[16] This discrepancy is not understood at the present time.

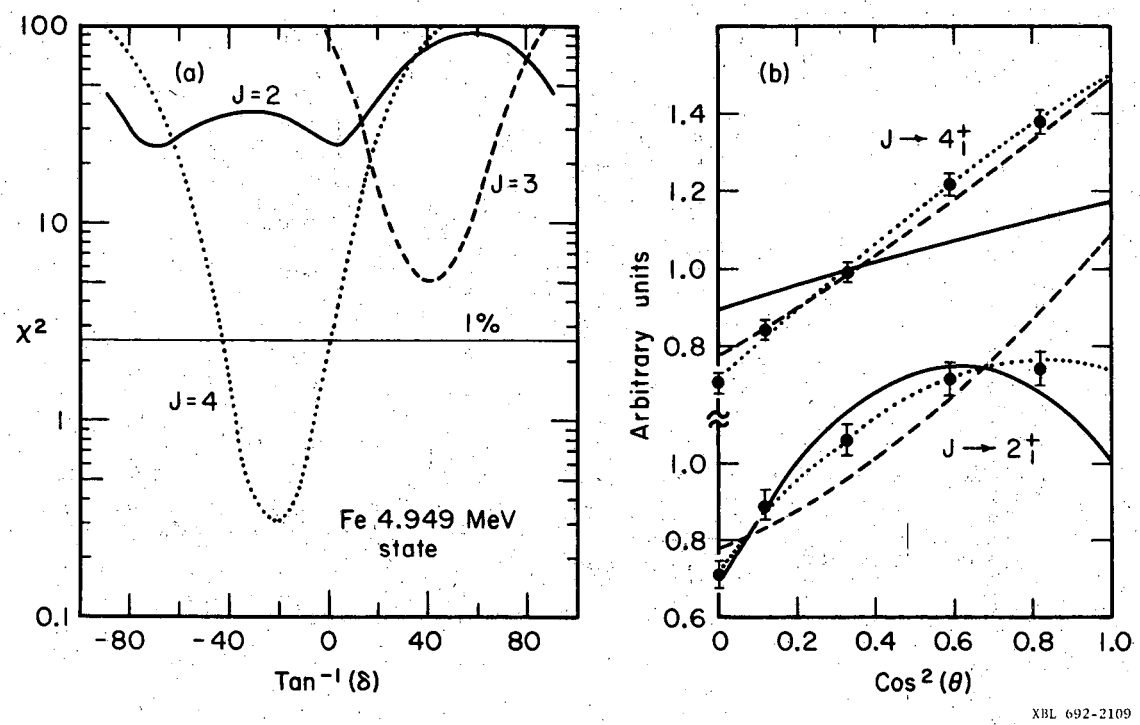

Fig. 43. χ^2 analysis for the 4.949-MeV state. The $4.949 \rightarrow 2_1^+$ and $4.949 \rightarrow 4_1^+$ transitions were fitted simultaneously. The mixing ratios for the assumed initial spins are as follows: for $J_i = 2$, $\delta(2 \rightarrow 4_1^+) = 0$ and $\delta(2 \rightarrow 2^+)$ is the variable; for $J_i = 3$, $\delta(3 \rightarrow 2_1^+) = -0.53$ and $\delta(3 \rightarrow 4)$ is the variable; and the $J_i = 4$, $\delta(4 \rightarrow 2_1^+) = 0$ and $\delta(4 \rightarrow 4_1^+)$ is the variable.

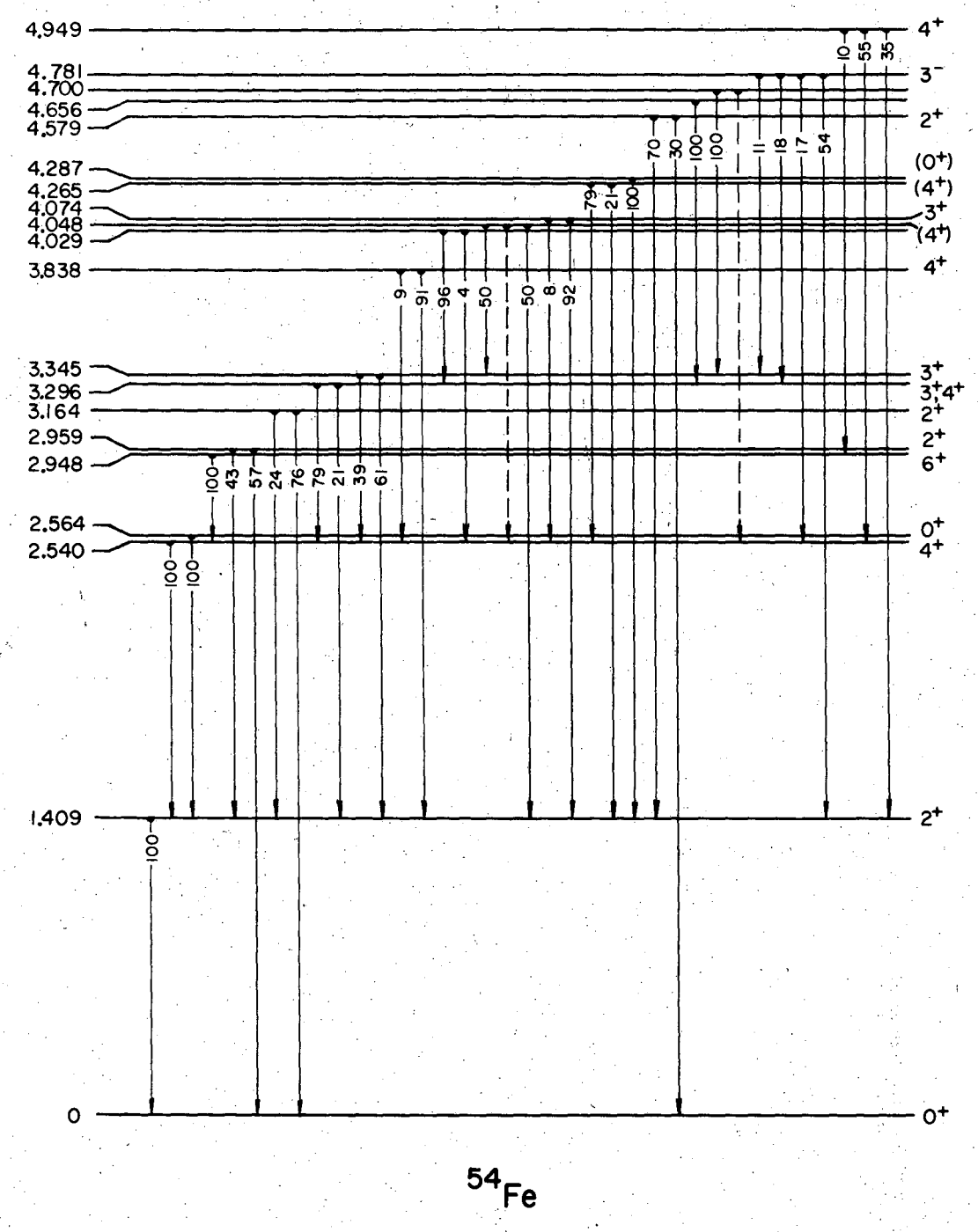

Fig. 44. Levels of ^{54}Fe below 5 MeV. The branching ratios were derived in the present experiment. The spin assignments include those from previous work and from this experiment. The excitation energies are from Refs. 62 and 63.

Table II. Branching ratios for the decay of excited states of ^{54}Fe.

Level	E_γ(MeV)	$J_i \rightarrow J_f$	Branching ratios	Other values (a)	(b)
1.409	1.409	2 → 0	100		
2.540	1.131	4 → 2	100		
2.564	1.155	0 → 2	100		
2.948	0.408	6 → 4	100		
2.959	1.550	2 → 2	43 ± 3	37 ± 5	49 ± 5
	2.959	2 → 0	57 ± 3	63 ± 5	51 ± 5
3.164	1.755	2 → 2	24 ± 3	17 ± 4	23 ± 4
	3.164	2 → 0	76 ± 3	83 ± 4	77 ± 4
3.296	0.756	3,4 → 4	79 ± 3		
	1.887	3,4 → 2	21 ± 3		
3.345	0.805	3 → 4	39 ± 3	43 ± 10	
	1.936	3 → 2	61 ± 3	57 ± 10	
3.838	0.548	4 → 3,4	≤ 2	7	
	1.298	4 → 4	9 ± 3	5	
	2.429	4 → 2	91 ± 3	88 ± 5	
4.029	0.733	J → 3,4	95 ± 3		
	1.498	J → 4	5 ± 3		
4.048	0.703	(4) → 3	50 ± 3		
	1.508	(4) → 4	≤ 2		
	2.639	(4) → 2	50 ± 3		
4.074	1.534	3 → 4	8 ± 3		
	2.665	3 → 2	92 ± 3		

Table II. Continued

Level	E_γ(MeV)	$J_i \rightarrow J_f$	Branching ratios	Other values (a)	(b)
4.265	1.725	(4) → 4	79 ± 14		
	2.856	(4) → 2	21 ± 6		
4.287	2.878	(0) → 2	100		
4.579	3.170	2 → 2	70 ± 10		
	4.579	2 → 0	30 ± 10		
4.656	1.360	J → 3,4	100		
4.700	1.355	J → 3	≥ 90		
	2.160	J → 4	≤ 10		
4.781	1.436	3 → 3	11 ± 3		
	1.485	3 → 4,3	18 ± 4		
	2.241	3 → 4	17 ± 4		
	3.372	3 → 2	54 ± 7		
4.949	2.001	4 → 6	10 ± 3		
	2.409	4 → 4	55 ± 5		
	3.540	4 → 2	35 ± 8		

(a) Ref. 16

(b) Ref. 73

Table III. Multipole mixing ratios for transitions in ^{54}Fe.

Level	E_γ(MeV)	$J_i \rightarrow J_f$	(E2/M1)	Other values
2.959	1.550	2 → 2	$0.105\pm^{0.040}_{0.042}$	0.25 ± 0.19,[a] $0\leq\delta\leq2.2$[b]
3.164	1.755	2 → 2	$0.63\pm^{0.57}_{0.25}$, $\delta\geq2.4$	$-0.60\pm^{0.40}_{0.34}$, $\lvert\delta\rvert\geq3$[a]
			$\delta\leq-10$	
3.296	0.756	4 → 4	$-1.1\leq\delta\leq-0.67$,	
			$-0.24\leq\delta\leq0.18$	
	0.756	3 → 4	$0.38\leq\delta\leq1.66$	
	1.887	3 → 2	$-12\leq\delta\leq-0.25$	
3.345	0.806	3 → 4	0 ± 0.14, $\delta\geq3.5$	
	1.936	3 → 2	$-0.65\pm^{0.18}_{2.25}$	
4.029	0.733	5 → 4	0.27 ± 0.07	
	0.733	3 → 4	$-1.2\pm^{0.82}_{1.5}$	
	0.733	4 → 3	0.27 ± 0.09	
	0.733	2 → 3	$-9\leq\delta\leq-0.43$	
4.048	0.703	2 → 3	-2.75 _ _ -0.38	
	0.703	4 → 3	0.23 ± 0.09	
4.074	2.665	3 → 2	$1.88\pm^{0.50}_{0.44}$	
4.265	1.725	3 → 4	$0.81\pm^{0.73}_{0.39}$	
	1.725	4 → 4	-0.53 ± 0.24	

Table III. Continued

Level	E_γ(MeV)	$J_i \rightarrow J_f$	δ(E2/M1)	Other values
4.287	2.879	1 → 2	All values of δ	
	2.879	2 → 2	$0.40\pm^{0.07}_{0.04}$, $\delta \leq -14$	
	2.879	3 → 2	$-0.16\pm^{0.05}_{0.01}$	
4.579	3.170	2 → 2	-0.105±0.09, -1.8±0.5	
4.781*	3.372	3 → 2	-0.018±0.026	
4.949	2.409	4 → 4	$-0.36\pm^{0.2}_{0.3}$	

*This state is known to have negative parity thus the mixing ratio is δ (M2/E1).

(a) Ref. 16

(b) Ref. 73

The Doppler shift analysis is summarized in Table IV. In most cases, only the gamma transition which gave the most precise value of $\Delta E/\Delta E_0$ is given; in cases where two transitions were analyzed for a given state, the lifetime derived was based on the weighted average of the two values of $\Delta E/\Delta E_0$. For gamma rays having values of $\Delta E/\Delta E_0$ less than 0.11,[74] the present analysis indicates only that the lifetime is longer than (or equal to) a certain limit. This limit is set by the value $\Delta E/\Delta E_0$ + error $(\Delta E/\Delta E_0)$.

The data from Tables II, III, and IV have been combined to produce the reduced transition probabilities given in Table V. For transitions where more than one δ was possible, we have included only the solution considered to be most likely. Furthermore, the parity of all states except the 4.781-MeV 3^- was assumed to be positive. Thus, for the former states, E2 and M1 transition probabilities are given. The errors in the derived quantities (e.g., BE2 or BM1) were obtained combining the errors in the branching ratios, mixing ratios, and lifetime in quadrature; this was done separately for the upper and for the lower limits of the BE2 or BM1.

E. Conclusion

In order to discuss the nature of the states in the low energy spectrum (< 4 MeV) of ^{54}Fe, it is convenient to appeal to analogy, since no detailed calculations are available. Fortunately, ^{42}Ca, a nucleus which should be similar to ^{54}Fe, has been the subject of intensive theoretical investigation.[4-7] For ^{42}Ca it has been found that, in addition to

Table IV. Mean lifetimes for states in ^{54}Fe from the Doppler shift attenuation analysis.

Level	E_γ(MeV)	E_0(keV)	E(keV)	$\Delta E/\Delta E_0$	τ(psec)
1.409	1.409	6.56	1.31±0.2	0.200±0.03	$1.1\pm^{0.50}_{0.32}$
2.540	1.131	5.03	0.3 ±0.2	0.06 ±0.04	≥ 3
2.564	1.155	5.13	0.6 ±0.3	0.12 ±0.04	≥ 2
2.948	0.408	1.82	0 ±0.4	≤ 0.22	≥ 0.8
2.959	1.550	6.89	4.82±0.30	0.700±0.04	0.075±0.012
	2.959	13.14	8.77±0.38	0.677±0.03	
3.164	3.164	13.95	5.63±0.5	0.404±0.036	$0.23\pm^{0.05}_{0.04}$
3.296	1.887	8.31	0.4 ±0.5	≤ 0.11	≥ 3
3.345	1.936	8.53	0.5 ±0.6	≤ 0.13	≥ 3
3.838	2.429	10.46	6.57±0.5	0.628±0.045	0.091±0.02
4.029	0.733	3.12	0 ±0.6	≤ 0.16	≥ 1
4.048	2.639	11.26	3.08±1.0	0.274±0.09	$0.44\pm^{0.34}_{0.15}$
4.074	2.665	11.36	7.29±0.76	0.642±0.07	0.084±0.025
4.265	1.725	7.30	4.05±0.5	0.550±0.07	$0.119\pm^{0.033}_{0.025}$
4.287	2.878	12.18	7.98±0.7	0.655±0.06	$0.080\pm^{0.024}_{0.020}$
4.579	3.170	13.27	13.33±0.7	1.00 ±0.05	≤ 0.01
4.656	1.360		-	-	-
4.700	1.355	unresolved	-	-	-
4.781	3.372	13.99	10.73±0.76	0.767±0.054	0.048±0.016
	3.372(DE)	13.99	11.34±0.9	0.811±0.065	
4.949	2.409	9.93	7.98±0.6	0.804±0.075	0.042±0.015

Table V. Electromagnetic transition probabilities for ^{54}Fe derived from Tables II, III, and IV.

Level	E_γ(MeV)	$J_i^\pi \rightarrow J_f^\pi$	δ(E2/M1)	BE2(e^2f^4)	BE2 (Weiskopf)	(M1)(eV)	BM1 (Weiskopf)
1.409	1.409	$2^+ \rightarrow 0^+$	0	$133\pm^{55}_{41}$			
				102 ± 4 [a]	8.4 ± 0.3		
2.540	1.131	$4^+ \rightarrow 2^+$	0	≤ 147	≤ 12		
2.564	1.155	$0^+ \rightarrow 2^+$	0	≤ 199	≤ 16		
2.959	1.550	$2^+ \rightarrow 2^+$	$0.105\pm^{0.040}_{0.042}$	$5.7\pm^{5.1}_{3.7}$	$0.47\pm^{0.42}_{0.30}$	3.73×10^{-3}	0.048 ± 0.008
	2.959	$2^+ \rightarrow 0^+$	0	27.2 ± 4.5	2.25 ± 0.4		
				45 ± 5 [b]			
3.164	1.755	$2^+ \rightarrow 2^+$	$0.63\pm^{0.57}_{0.25}$	$12.7\pm^{20}_{7.8}$	$1.0\pm^{1.7}_{0.6}$	4.3×10^{-4}	$0.0038\pm^{0.0013}_{0.002}$
	3.164	$2^+ \rightarrow 0^+$	0	8.8 ± 1.9	0.73 ± 0.16		
3.296	1.887	$(4^+) \rightarrow 2^+$	0	≤ 2.4	≤ 0.2		
3.345	1.936	$3^{(+)} \rightarrow 2^+$	$-0.65\pm^{0.18}_{2.25}$	≤ 5.4	≤ 0.45	$\leq 1.1\ 10^{-4}$	≤ 0.0007
3.838	1.298	$4^+ \rightarrow 4^+$	0			6.5×10^{-4}	0.014 ± 0.006
	2.429	$4^+ \rightarrow 2^+$	0	96.7 ± 21	8.0 ± 1.8		
4.048	0.703	$(4^+) \rightarrow 3^{(+)}$	0.23 ± 0.09	$270\pm^{270}_{203}$	$22\pm^{22}_{16}$		

Table V. Continued

Level	E_γ(MeV)	$J_i^\pi \rightarrow J_f^\pi$	δ(E2/M1)	BE2(e^2f^4)	BE2 (Weiskopf)	(M1)(eV)	BM1 (Weiskopf)
	0.703	$(2^+)\rightarrow 3^{(+)}$	$-1.2\pm^{0.82}_{1.5}$	$3180\pm^{2270}_{2860}$	$263\pm^{187}_{237}$		
	2.639	$(4^+)\rightarrow 2^+$	0	$7.2\pm^{3.8}_{3.1}$	$0.6\pm^{0.30}_{0.26}$		
4.074	1.534	$3^{(+)}\rightarrow 4^+$	0			6.3×10^{-4}	0.0083±0.004
	2.665	$3^{(+)}\rightarrow 2^+$	$1.88\pm^{0.50}_{0.44}$	51.7±16	4.3±1.3	1.6×10^{-3}	0.004 ±0.002
4.265	1.725	$(4^+)\rightarrow 4^+$	-0.53±0.24	77.6±55	6.4±4.5	3.4×10^{-3}	0.032 ±0.011
	2.856	$(4^+)\rightarrow 2^+$	0	7.6±2.9	0.63±0.24		
4.287	2.879	$(0^+)\rightarrow 2^+$	0	51.5±14	4.3 ±1.2		
4.579	3.170	$2^{(+)}\rightarrow 2^+$	-0.105±0.09	$\geq$ 0.04	$\geq$ 0.003	$\geq 3.8\ 10^{-2}$	$\geq$ 0.057
	4.579	$2^{(+)}\rightarrow 0^+$	0	$\geq$ 12	$\geq$ 1		
4.949	2.001	$4^{(+)}\rightarrow 6^+$	0	60.3±28	5.0±2.3		
	2.409	$4^{(+)}\rightarrow 4^+$	$-0.36\pm^{0.2}_{0.3}$	$15\pm^{24}_{12}$	$1.2\pm^{2.0}_{0.9}$	7.6×10^{-3}	0.026±0.01

Table V. Continued

Level	E_γ(MeV)	$J_i^\pi \rightarrow J_f^\pi$	δ(M2/E1)	BE1(e^2f^2)	BE1 (Weiskopf)
4.781	1.436	$3^- \rightarrow 3^+$	0	4.9×10^{-4}	$(5.3\pm2.3)\times10^{-4}$
	1.485	$3^- \rightarrow 4^+,3^+$	0	7.2×10^{-4}	$(7.8\pm3.1)\times10^{-4}$
	2.241	$3^- \rightarrow 4^+$	0	2.0×10^{-4}	$(2.1\pm0.9)\times10^{-4}$
	3.372	$3^- \rightarrow 2^+$	0	1.84×10^{-4}	$(1.99\pm0.7)\times10^{-4}$

(a) From Ref. 67.

the expected states of the $(f_{7/2})^2_J$ neutron configuration, two states having J = 0 and J = 2 occur at low excitation energy. A successful explanation has been given (Refs. 5,7) in terms of a low-lying deformed band of 4-particle-2-hole states which mix with the $(f_{7/2})^2_J$ states. Gerace and Green[5] show that this model is able to account for the rather remarkable E2-transition probabilities found in this nucleus.

Because of the similarities between ^{54}Fe and ^{42}Ca, it is of interest to compare the respective matrix elements between states for these nuclei. Table VI lists the presently known analogous transition probabilities for ^{42}Ca, ^{50}Ti, and ^{54}Fe. The level schemes of these nuclei are shown in Fig. 45.

In ^{42}Ca, it has been shown[5] that the enhancement of the $2^+_1 \rightarrow 0^+_1$ and $0^+_2 \rightarrow 2^+_1$ transitions is due to a constructive interference between the spherical (mostly $(f_{7/2})^2$) and deformed amplitudes, while the $2^+_2 \rightarrow 0^+_1$ transition is comparatively retarded due to destructive interference. The situation is quite different in ^{54}Fe where the $0^+_2 \rightarrow 2^+_1$ BE2, though only available as an upper limit, is definitely not as enhanced as it is in ^{42}Ca. Although the effect is not so pronounced, the $2^+_2 \rightarrow 0^+_1$ transition in ^{54}Fe is stronger than it is in ^{42}Ca. Gerace and Green predict a rather enhanced $2^+_2 \rightarrow 2^+_1$ E2; this is consistent with experiment in ^{42}Ca, but not in ^{54}Fe.

These observations indicate a situation at least roughly consistent with the fact that the "extra" 2^+ and 0^+ states of ^{54}Fe are at a higher excitation energy than those in ^{42}Ca. Thus the mixing between the two types of states should be less in ^{54}Fe, resulting in different E2

Table VI. Comparison of electromagnetic transition probabilities in ^{42}Ca, ^{50}Ti, and ^{54}Fe. The values of $B\sigma\lambda$ are in Weiskopf units.

Transition	$\sigma\lambda$	^{42}Ca	^{54}Fe	^{50}Ti
$2_1^+ \rightarrow 0_1^+$	E2	8.6 ± 2.0[a]	8.4 ± 0.8[b]	5.9 ± 1.5[c]
$0_2^+ \rightarrow 2_1^+$	E2	65 ± 4[d]	≤ 16	
$2_2^+ \rightarrow 0_1^+$	E2	1.2 ± 0.3[d]	2.25 ± 0.4	
$2_2^+ \rightarrow 2_1^+$	E2	$14.3 \pm^{35}_{8.5}$[d]	$0.47 \pm^{0.42}_{0.30}$	
$2_2^+ \rightarrow 2_1^+$	M1	0.091 ± 0.02[d]	0.048 ± 0.008	
$4_1^+ \rightarrow 2_1^+$	E2	1.0 ± 0.3[e]	≤ 12	

(a) Ref. 8 Value derived for the work of Metzger and Tandon.

(b) Ref. 67.

(c) Ref. 82.

(d) Ref. 8 Values derived from the work of Kossler et al.

(e) Ref. 10.

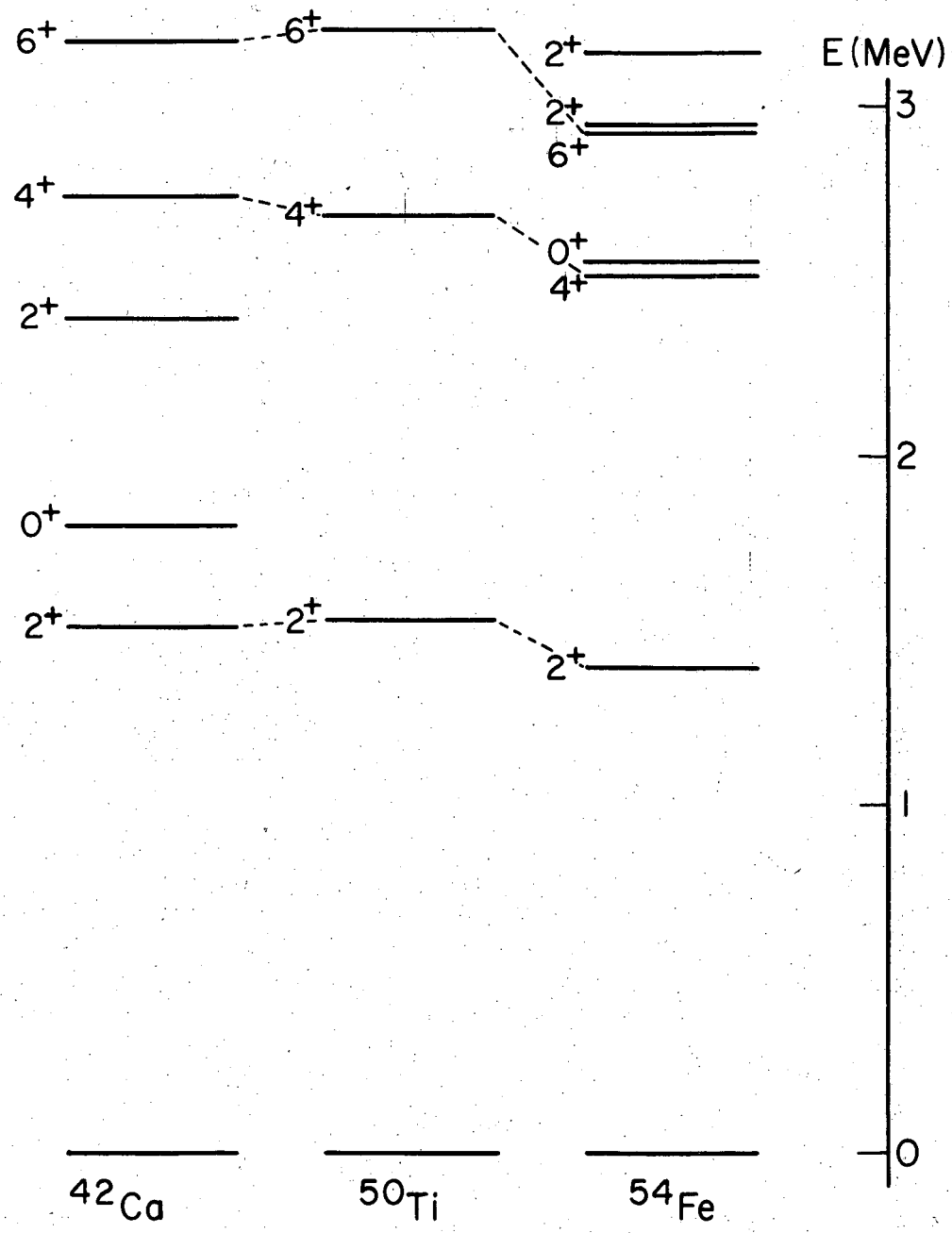

XBL693-2297

Fig. 45. Comparison of the low-lying states of ^{42}Ca, ^{50}Ti, and ^{54}Fe. The dotted lines show the states of the $(f_{7/2})^{\pm 2}_{J}$ configuration.

matrix elements. It is perhaps surprising, then, that the $2_1^+ \rightarrow 0_1^+$ BE2's are similar in ^{42}Ca, ^{50}Ti, and ^{54}Fe. However, core polarization is known to have a profound effect on $2_1^+ \rightarrow 0_1^+$ transition rates; it is possible that such phenomena contribute differently in ^{42}Ca than in ^{50}Ti or ^{54}Fe.

Among the more interesting features of the spectrum of ^{54}Fe below 4 MeV are the states at 3.296-MeV (3^+, 4^+) and 3.345-MeV (3^+). It is clear, on the basis of the present evidence, that these states are of quite a different nature than the states to which they decay. It is seen in Table V that the lifetime limits for the states of the doublet indicate transition strengths which are very retarded compared with the typical E2 and M1 rates observed in ^{54}Fe. Further evidence on the special nature of the 3.296 and 3.345-MeV states comes from the observation that they are favored as final states in the decay of several high-lying states. In these cases, either very retarded transitions or no transitions at all are observed to the assumed $f_{7/2}^2$ states; since the spins of the final states are no greater than 4, spin selection rules cannot be the explanation.

In constrast to the states of the doublet, the 3.838-MeV 4^+ state decays by a considerably enhanced E2 transition to the first 2^+ state. This 4^+ state is excited with a larger cross section than the 2.540-MeV 4^+ by inelastic proton scattering near 20 MeV.[11,13]

With regards to the high-lying levels (> 4 MeV), it will probably not be possible in the near future to relate the observed decay properties to a nuclear model. However, such information should be valuable for establishing systematics among levels in other nuclei in this mass region.

For example, a systematic study of the decay of the numerous known 3^- states[75] in the $f_{7/2}$ shell nuclei would be quite interesting. We believe that the experimental techniques employed here are suitable for the detailed investigations required.

For the more immediate problem of understanding the complex low-energy spectrum of ^{54}Fe, a theoretical study of the sophistication of that applied to ^{42}Ca would be valuable. Experimentally, of course, not all the facts are in. It would be of considerable interest to know the lifetimes of the 2.540, 2.564, 3.296, and 3.345-MeV states. A high resolution study of the $^{56}Fe(p,t)^{54}Fe$ reaction would provide additional complementary information on the nature of the ^{54}Fe excited states.

V. SPIN-FLIP: EXPERIMENT AND RESULTS

A. Data Collection

Coincidence spectra were taken, two angles simultaneously, in steps of roughly 10° from 45° to 148°, proton-counter lab-angle. Counting rates in the particle detectors ranged from about 3,000 cps at 145° to about 15,000 cps at 45°. The resolution was in the range 150-200 keV, being determined mostly by kinematic broadening. Figure 46 shows a typical proton singles spectrum. The gamma counting rate was about 20,000 cps; the observed resolution at this rate was 5 to 6 keV at 1 MeV. Counting time at each angle ranged from 2 to 6 hours, depending on the spin-flip cross section; it was possible to determine the number of real events obtained by periodically printing out the display field of the

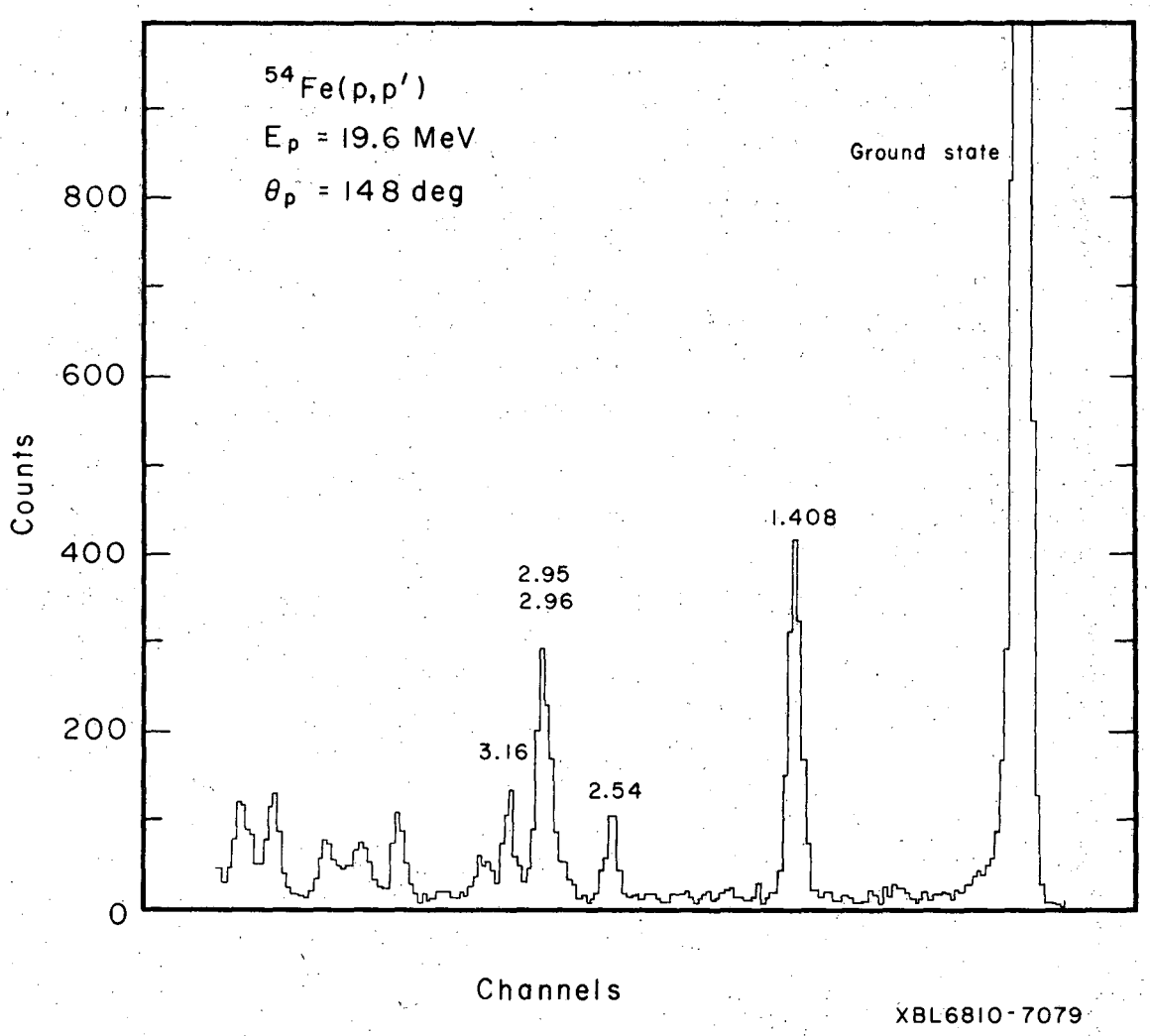

Fig. 46. Proton singles spectrum from the reaction $^{54}Fe(p,p')^{54}Fe$ at 19.6 MeV.

on-line PDP-5 computer. As a check of the consistency of the measurements, several angles were repeated; the angles 90° and 95° were measured with both particle detectors.

Singles elastic and inelastic cross sections were measured for ^{54}Fe and ^{56}Fe at 19.6 MeV with good resolution and geometry, using the experimental apparatus described in Sec. II.H. The total absolute error in extracting the cross section is estimated to be less than 10%; the largest uncertainty is due to measurement of the target thickness. Relative errors are less than 3%.

Besides its contribution as an integral part of the spin-flip, cross section, and asymmetry analysis, the cross-section data were necessary in order to properly normalize the measured spin-flip intensities to produce spin-flip probabilities.

B. Data Reduction and Results

The number of coincident counts, R', can be related to the spin-flip probability, $S(\theta)$, by the following expression in the limit of infinitesimal solid angles.[34]

$$S(\theta) = W\varepsilon_\gamma R'/N$$

where θ is the proton scattering angle, ε_γ is the gamma detection efficiency (including solid angle), W is a calculable geometrical factor which is equal to 5/2 for a point gamma detector at 90°, and N is the total number of counts in the particle counter arising from the excitation of the 2^+ state. In practice, this expression becomes:

$$S(\theta) = \frac{W\varepsilon_\gamma}{N} [R - C] - B(\theta)$$

where R is the measured number of coincidences and C is the number of chance coincidences as given by Eq. (III-11). The contribution due to non-spin-flip processes which arises from the finite solid angles used is labeled $B(\theta)$. The errors quoted are due to the evaluation of R' (e.g., R and C). The statistical errors in other measured quantities such as ε_γ or N are not significant; the errors were almost invariably dominated by the error in R'.

Two different procedures were used to evaluate the number of coincidence events, R or C. The first summed over a small region of the two-dimensional array that contained only the 2^+ proton peak and the full-energy gamma peak (FEP) (see Fig. 47). The efficiency of the gamma detector could be directly interpolated from our calibration curve. The second procedure included gamma counts in the FEP and Compton distribution down to, but not including, the annhilation peak at 511 keV. The efficiency for this method of summation was obtained in the following way. The total number of counts, R', in coincidence with the 2^+ proton peak was evaluated for both methods of summation. Then these quantities were summed over all angles in order to obtain the ratio of the total number of counts in the Compton + FEP region to those in the FEP alone. This results in a 5% statistical error in the overall normalization.

The full-spectrum summation increases the efficiency by a factor of 8.5 for the 1.409-MeV state of ^{54}Fe. The final results are obtained by this method. Comparison of the two methods for ^{54}Fe showed, within

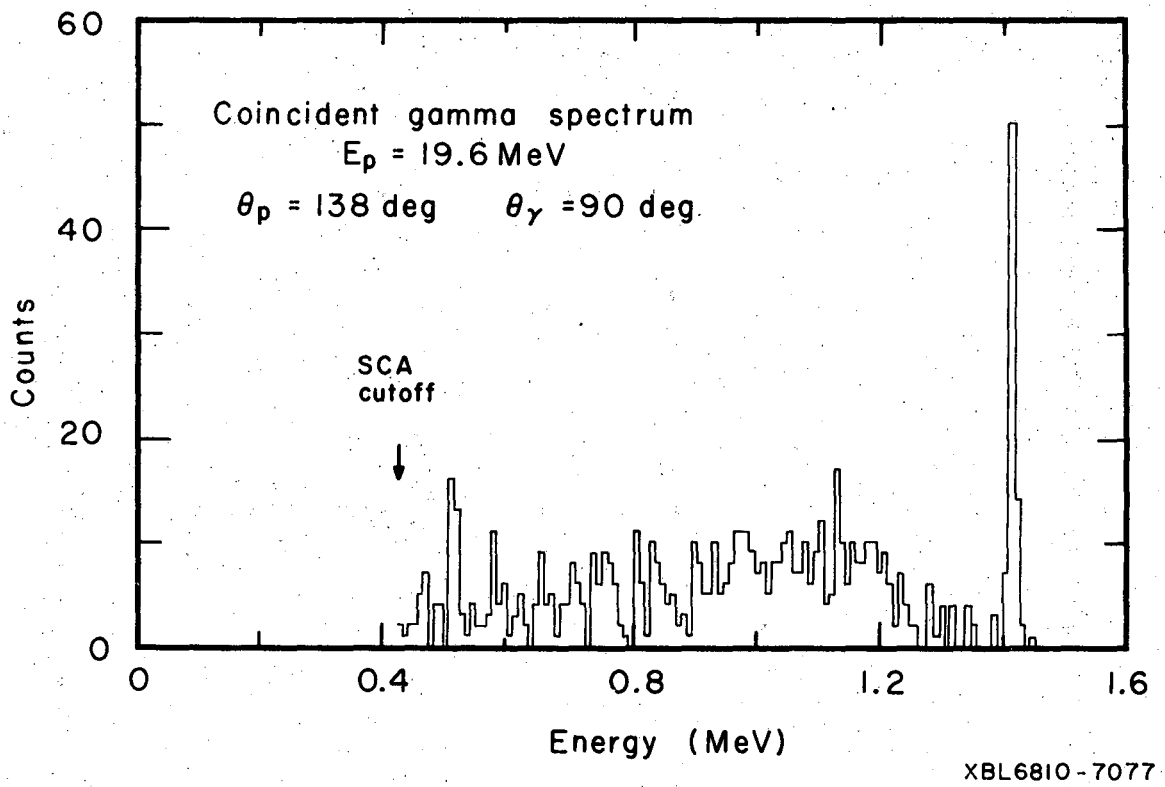

Fig. 47. Coincident gamma spectrum from the spin-flip experiment $^{54}Fe(p,p'\gamma)^{54}Fe$ at 19.6 MeV. Shown is the full-energy peak (1.409 MeV) and Compton distribution for the $2_1^+ \rightarrow 0_1^+$ transition.

errors, the same results. For ^{56}Fe, the summations were over only the FEP.

The singles proton spectra, scaled down to eliminate analyzer dead time effects, were recorded for both counters in all runs. At forward and backward angles, the number of singles events could be extracted directly from these spectra. At intermediate angles, the 2^+ peak was obscured by elastic events from carbon and oxygen target contaminants. At these angles, the ratio between inelastic and elastic events was determined from the previously measured cross sections by averaging over the angular acceptance of the proton counters. Where it was possible to check, this indirect method agreed with the direct determination to within 10%.

The admixture of the non-spin-flip contribution, $B(\theta)$, can be calculated to be generally about 0.02, if the reasonable assumption is made that all such amplitudes are equally probable and that coherent effects are small.[34] Maximum violation of these assumptions would change $B(\theta)$ by less than a factor of two. At two angles (45° and 95°) for ^{54}Fe, $B(\theta)$ was directly measured by both increasing and decreasing the gamma counter solid angle by a factor of two. These measurements are consistent within statistics with the calculation.

The $S(\theta)$ for the first 2^+ states of ^{54}Fe and ^{56}Fe are shown in Figs. 48 and 49, along with theoretical predictions which will be discussed later. It is apparent that the large differences between the asymmetries for the two states are not reflected in their $S(\theta)$'s. In addition to the large back-angle peak also seen in other work, both

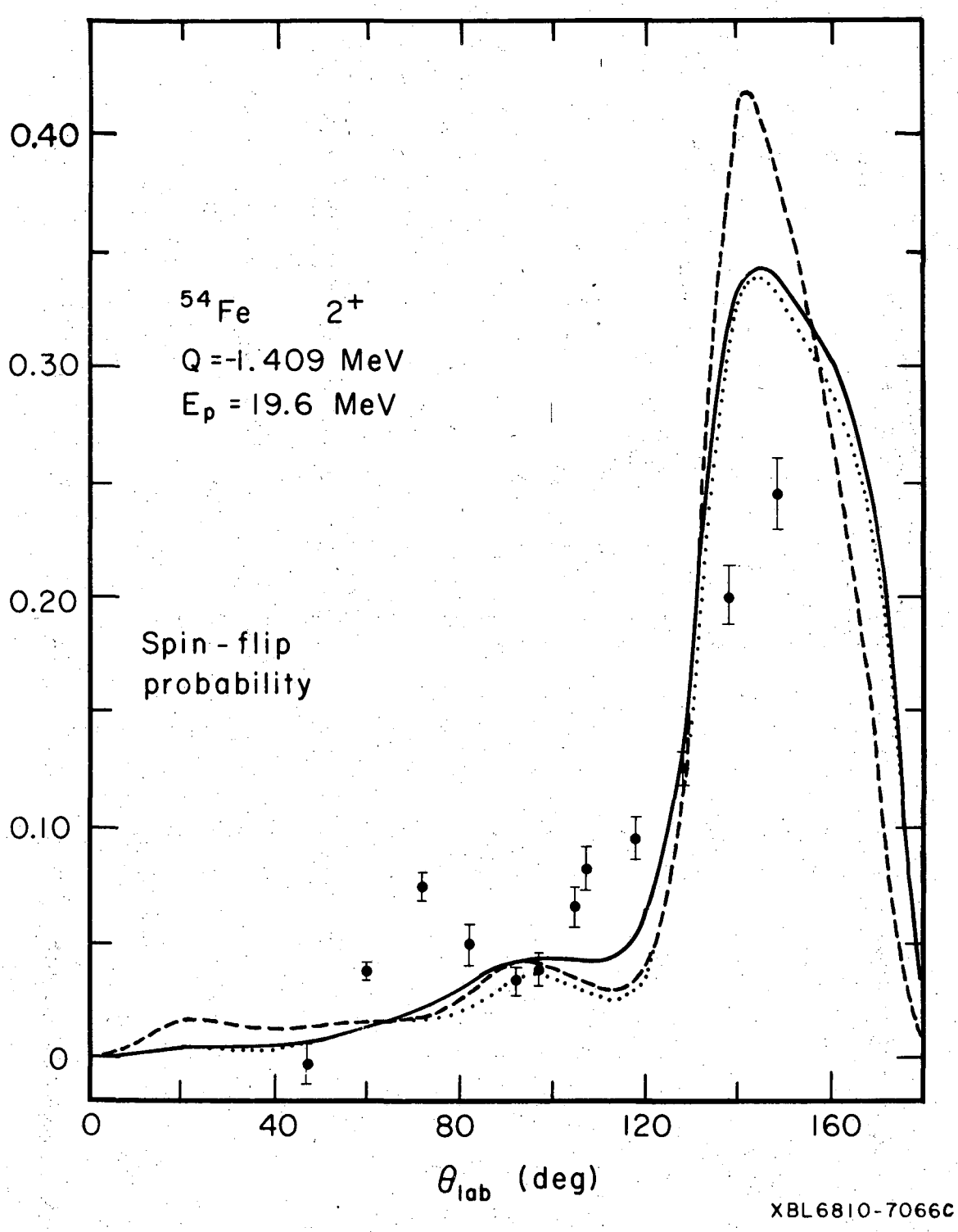

Fig. 48. Spin-flip probability S(θ) for ^{54}Fe. The curves are collective-model DWBA predictions with three types of deformed spin-orbit term: FT (solid), DSO (dotted), and NDSO (dashed).

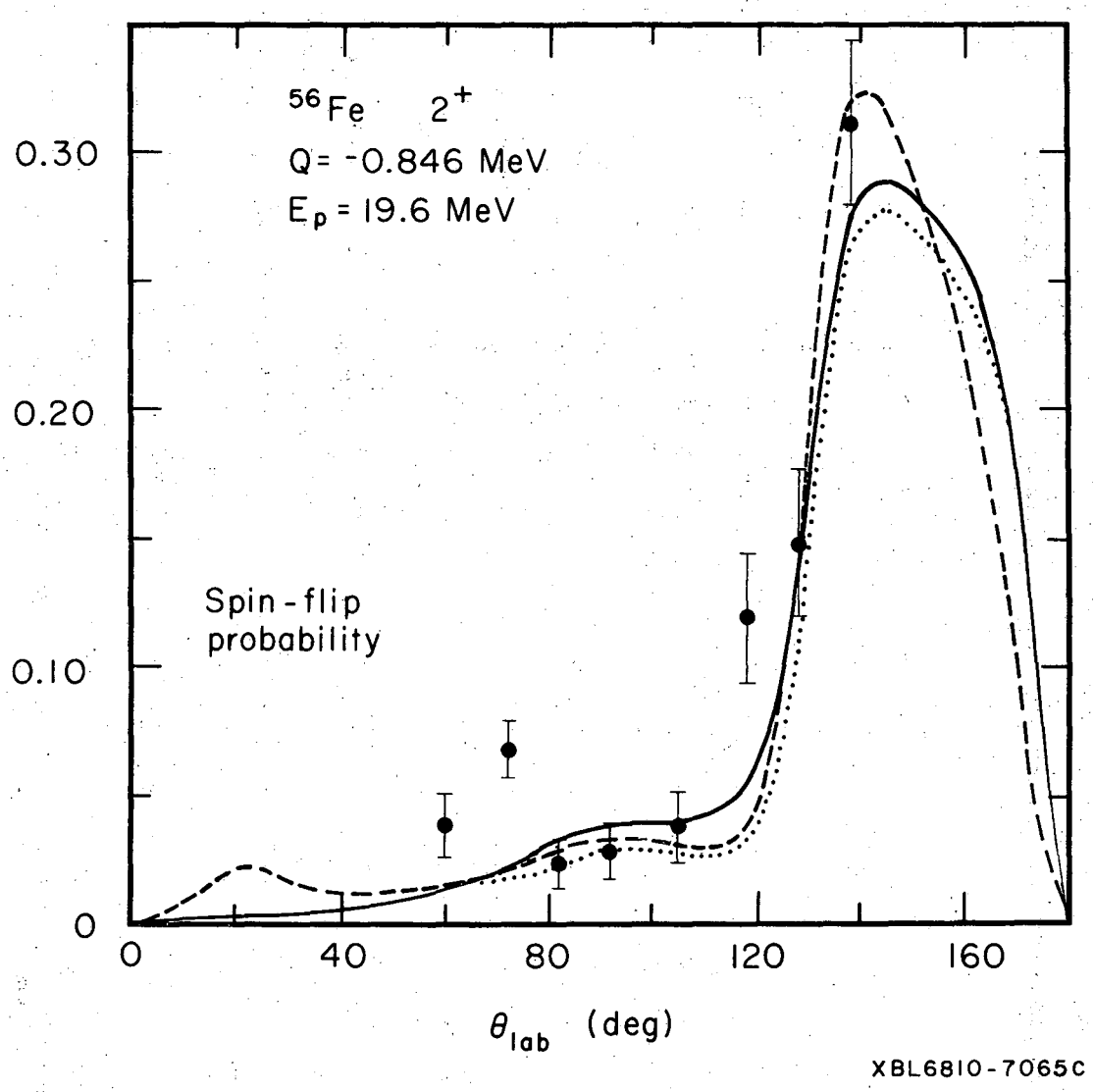

Fig. 49. Spin-flip probability S(θ) for ^{56}Fe. The curves are collective-model DWBA predictions as described for Fig. 48.

distributions show a maximum at 70°;[36,76] these features are more pronounced in ^{54}Fe where the statistical precision is better.

Figures 50 and 51 show the asymmetries for the first 2^+ states of ^{54}Fe and ^{56}Fe, respectively, obtained with 19.6-MeV polarized protons at Saclay.[1] These data are quite similar to those measured at 18.6 MeV,[30] suggesting that compound-nucleus contributions are not important. The small asymmetry at 30° and 90° for ^{56}Fe is found also for L = 2 transitions in the nickel isotopes, whereas large asymmetries at these angles were observed[30] for ^{52}Cr and ^{50}Ti.

Cross sections for the two states in ^{54}Fe and ^{56}Fe also have different shapes; they are shown in Figs. 52 and 53. The cross section for ^{54}Fe decreases less rapidly with increasing angle than does the ^{56}Fe cross section.

C. Analysis

1. Optical Model

The predictions of $S(\theta)$ in a collective-model analysis are quite sensitive to the optical parameters chosen; in particular, to the depth of the spin-orbit potential and to a lesser extent to the parameters of the imaginary potential. For this reason we have made a rather extensive search of parameter space to determine the degree to which the best-fit parameters are fixed, on the basis of χ^2. For both nuclei, cross-section and polarization data at 19.6 MeV were analyzed.

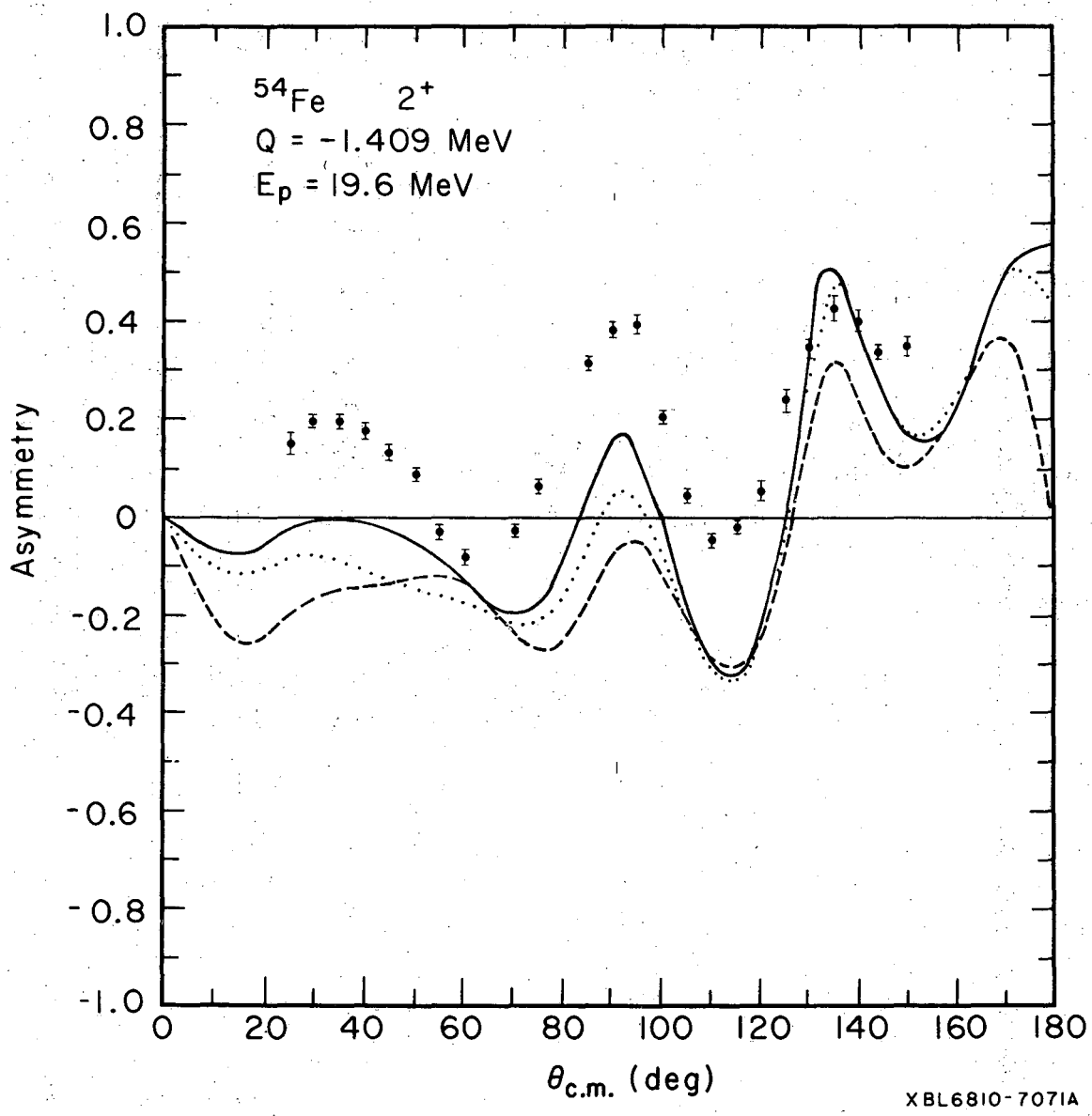

Fig. 50. Asymmetry for ^{54}Fe, measured at Saclay (Ref. 1). The curves are collective-model DWBA predictions as described for Fig. 48.

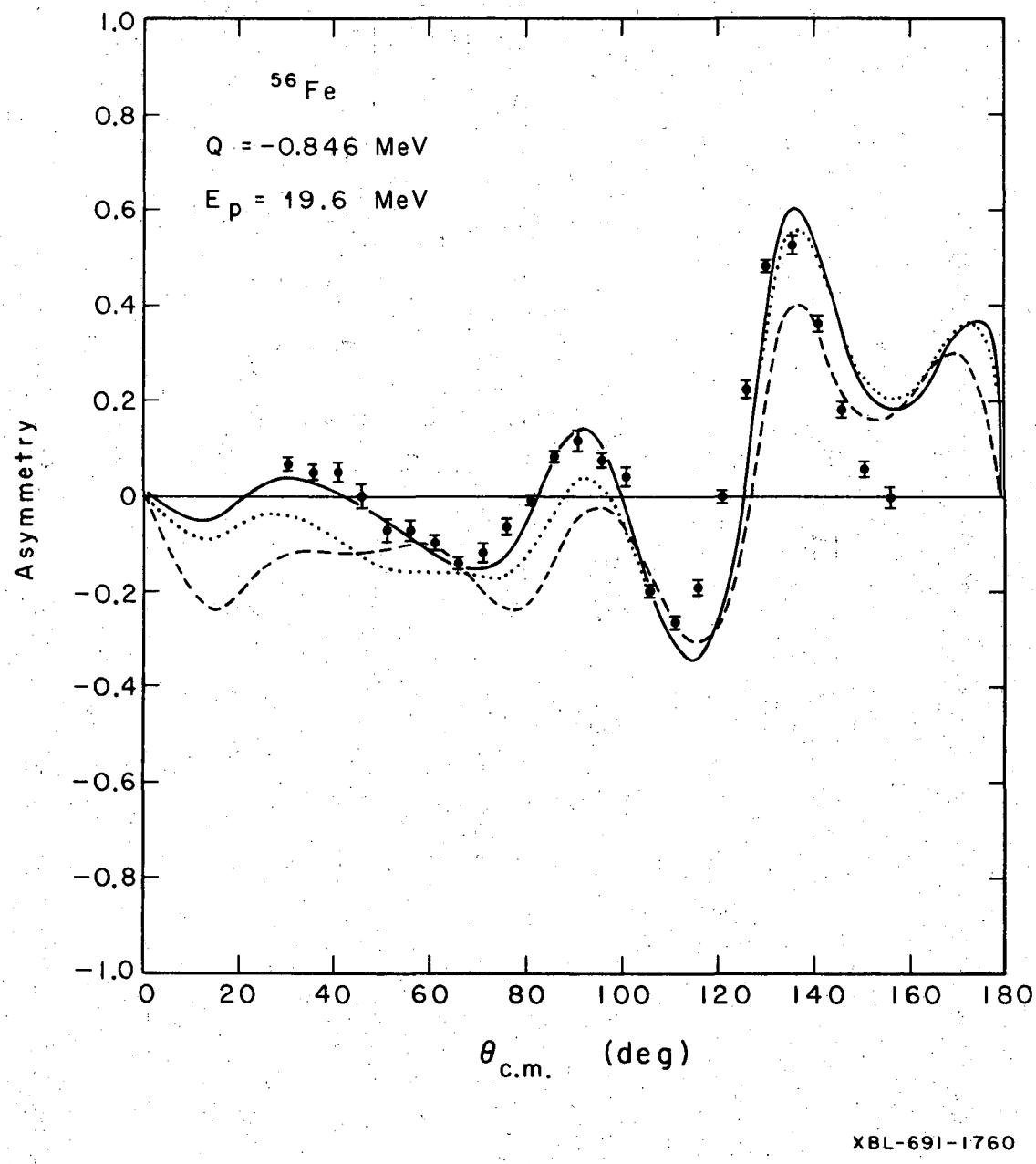

Fig. 51. Asymmetry for ^{56}Fe, measured at Saclay (Ref. 1). The curves are collective-model DWBA predictions as described for Fig. 48.

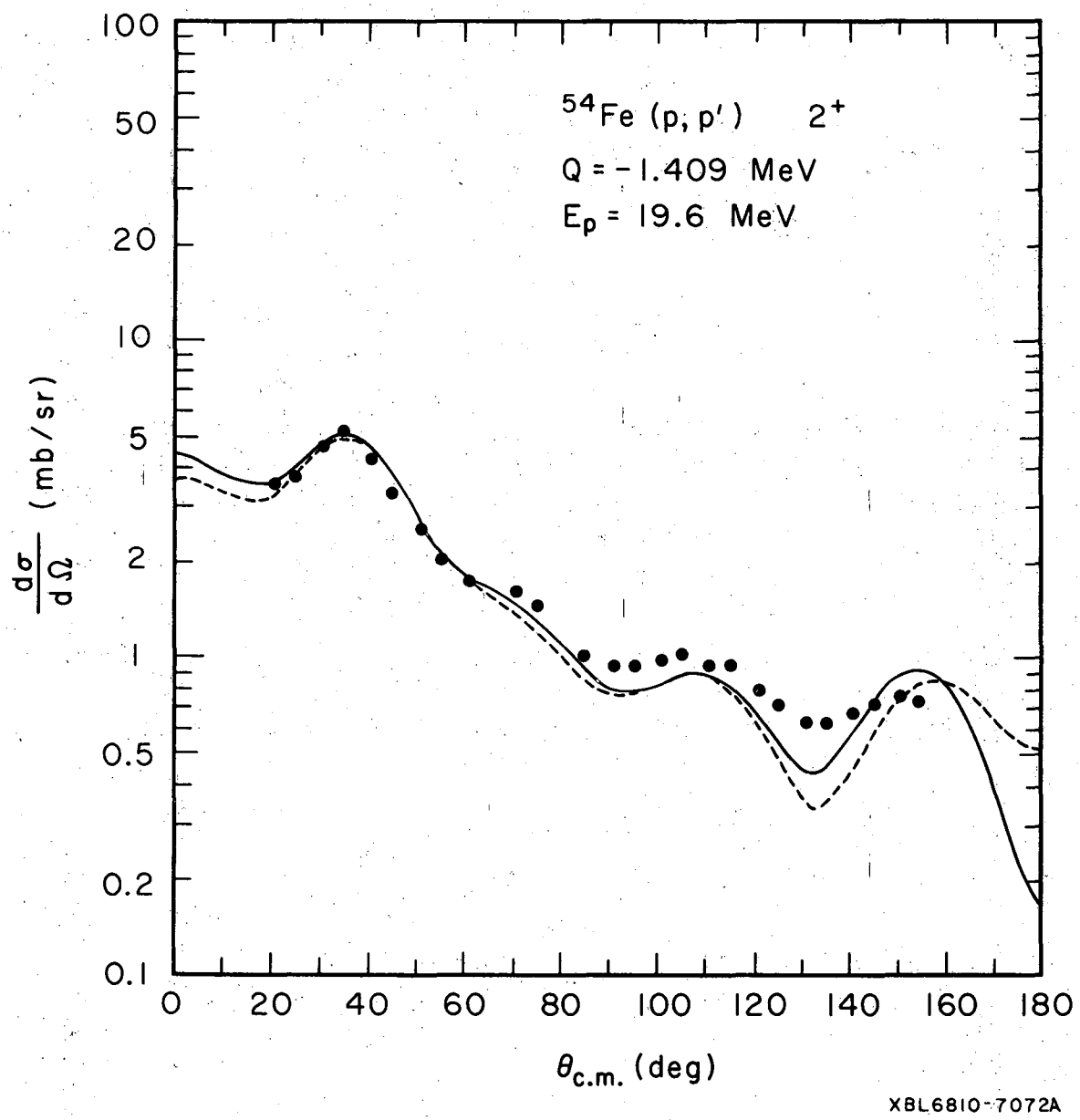

Fig. 52. Differential cross section for ^{54}Fe. The curves are collective-model DWBA predictions as described for Fig. 48.

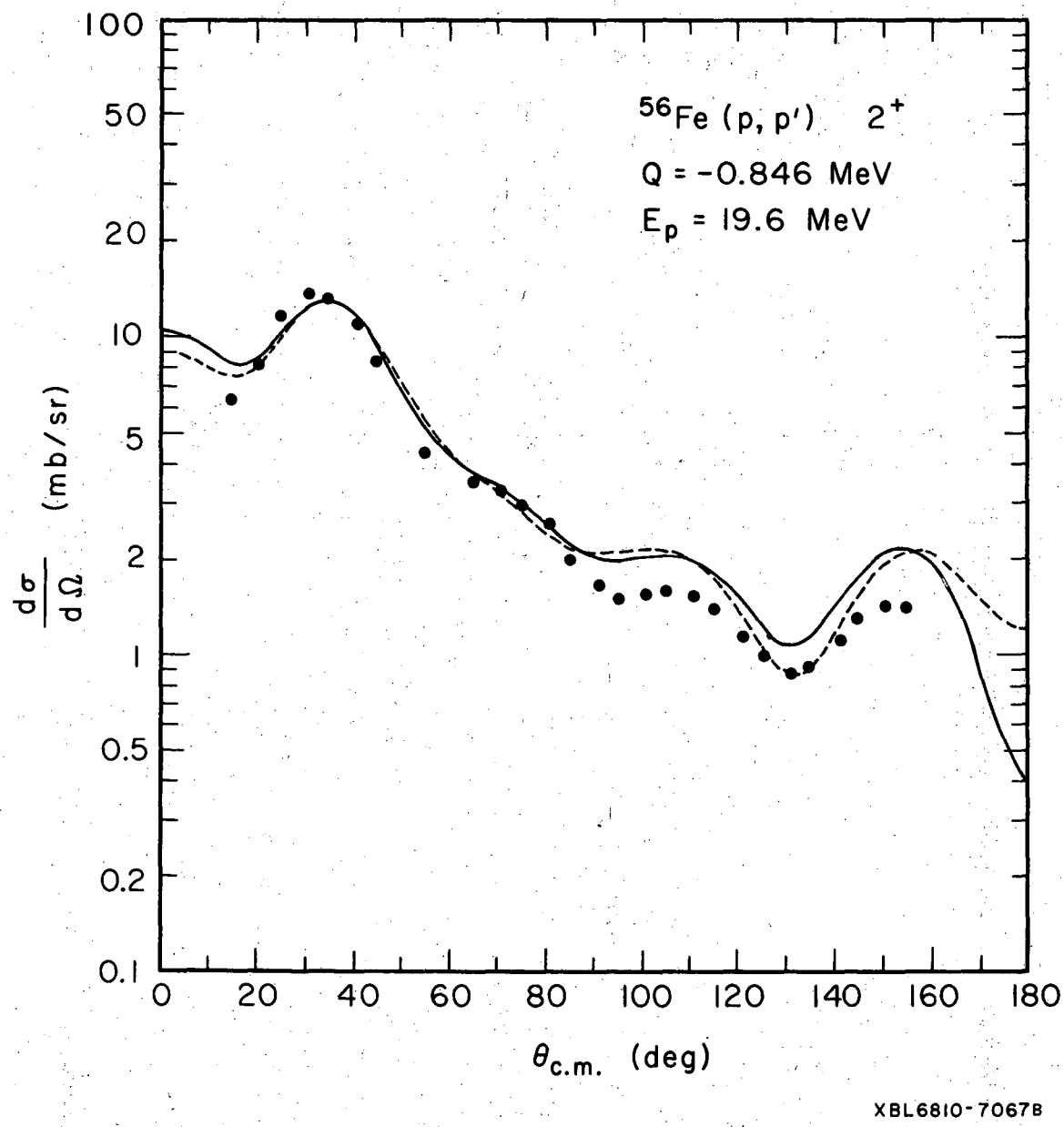

Fig. 53. Differential cross section for ^{56}Fe. The curves are collective-model DWBA predictions as described for Fig. 48.

The optical potential used had the standard form:

$$U(r) = -V\, f(r,r_r,a_r) - 4ia_i\, W_D \frac{d}{dr} f(r,r_i,a_i)$$
$$+ \left(\frac{h}{m_\pi c}\right)^2 V_{so}\, \underset{\sim}{\sigma}\cdot\underset{\sim}{\ell}\, r^{-1} \frac{d}{dr} f(r,r_{so},a_{so}).$$

The Coulomb potential of a uniformly charged sphere was added to U(r); the functions $f(r,r_r,a_r)$ are of the Wood-Saxon form. A modified version of the UCLA code SEEK[77] was used to minimize χ^2, which is defined as:

$$\chi^2 = \chi_P^2 + \chi_\sigma^2$$

$$\chi_\sigma^2 = \sum_i \frac{(\sigma_t^i - \sigma_{ex}^i)^2}{E_i^2}$$

$$\chi_P^2 = \sum_i \frac{(P_t^i - P_{ex}^i)^2}{E_i^2}$$

The subscripts t and ex refer to the values of the theoretical and experimental quantities, respectively, at each point i. The E_i are the experimental errors. Unless stated otherwise, we have taken the errors to be a constant percentage of the cross section at each angle (usually 3%); for the polarization, the quoted experimental errors were used (ranging from ± 0.01 at forward angles to ± 0.03 at backward angles).

In accordance with previous analyses in this energy region, we have generally used a pure surface-imaginary well and only a real spin-orbit well. The addition of a small volume term (1.5 MeV) improves the fit only slightly and has a negligible effect on the inelastic predictions.

The imaginary spin-orbit well was found to be close to zero in the analysis of 18.6 MeV elastic scattering;[78] we have found that this remains true at 19.6 MeV and have therefore omitted it in the analysis.

In addition to V, W_D, and V_{so}, the geometrical parameters of all three potentials were used as variables in the fit to the cross section and polarization data. The usual procedure was to use only a few parameters at a time as variables in order to more easily assess the improvement in the fit due to each.

Several parameters (all except r_{so},a_{so},V, a) were gridded over a sizable range, while χ^2 was minimized at each point. This allowed the explicit χ^2 dependence of the gridded parameter to be displayed and lessened the possibility of missing any local minima.

The results of this procedure indicated no significant difference in any of the geometrical parameters between ^{54}Fe and ^{56}Fe; thus, we adopted the average set given in Table VII. These are close to those used by Kossanyi-Demay and de Swiniarski[78] for the analysis of 18.6-MeV proton scattering. A real radius of 1.19 F seems quite adequate for both nuclei; any restrictions of this parameter to values smaller than 1.17 F or larger than 1.25 F results in a considerably poorer fit. The real diffuseness remains close to 0.7 F for a wide variety of parameter situations. An imaginary radius which is larger than the real radius results in a significant improvement in the fit; this is consistent with previous work.[78,79] For the present data, values of at least 1.3 F are required. The diffuseness of the imaginary well is found to consistently smaller than the real diffuseness. The spin-orbit radius was found to be

Table VII. Best fit optical model parameters for ^{54}Fe and ^{56}Fe.

	V (MeV)	W_D (MeV)	V_{so} (MeV)	r_r (F)	r_i (F)	r_{so} (F)	a_r (F)	a_i (F)	a_{so} (F)
^{54}Fe	50.51	7.94	5.06	1.19	1.31	1.075	0.70	0.55	0.40
^{56}Fe	50.48	8.83	5.12	1.19	1.31	1.075	0.70	0.55	0.40

consistently about 10% less than the real radius in a wide variety of parameter configurations; this, of course, has been observed before.[78,80] The spin-orbit diffuseness is rather poorly fixed between 0.35 and 0.5 F.

Using the average geometrical parameters and searching only on V, W_D, V_{so} we find significant differences between ^{54}Fe and ^{56}Fe only in the depth of the imaginary potential. The final parameters are given in Table VII; the corresponding fits are shown in Figs. 54-57. The polarization data are fitted quite well (especially for ^{54}Fe), while the cross section fits are only fair. It is of interest to note that in the back-angle region, where the fits are poor, there are considerable differences between the ^{54}Fe and ^{56}Fe cross sections. Thus, the similarity in optical potentials is somewhat misleading.

Attempts were made to improve the agreement with the back-angle cross section points by increasing their corresponding weighting factors. However, this decreases the quality of the fit generally and results in only a slight difference in optical parameters.

In parameter searches using only cross-section data, we found that it is possible to obtain quite good fits for both ^{54}Fe and ^{56}Fe if r_i is 1.4 F. This also requires that W_D be about 16 MeV, which is significantly larger than the values found in previous analyses; a_i was usually about 0.35 F. The polarization fits which are produced by such parameters are very poor and allow one to eliminate these solutions. We mention this only to illustrate the dangers of parameter searches using only differential cross-section data.

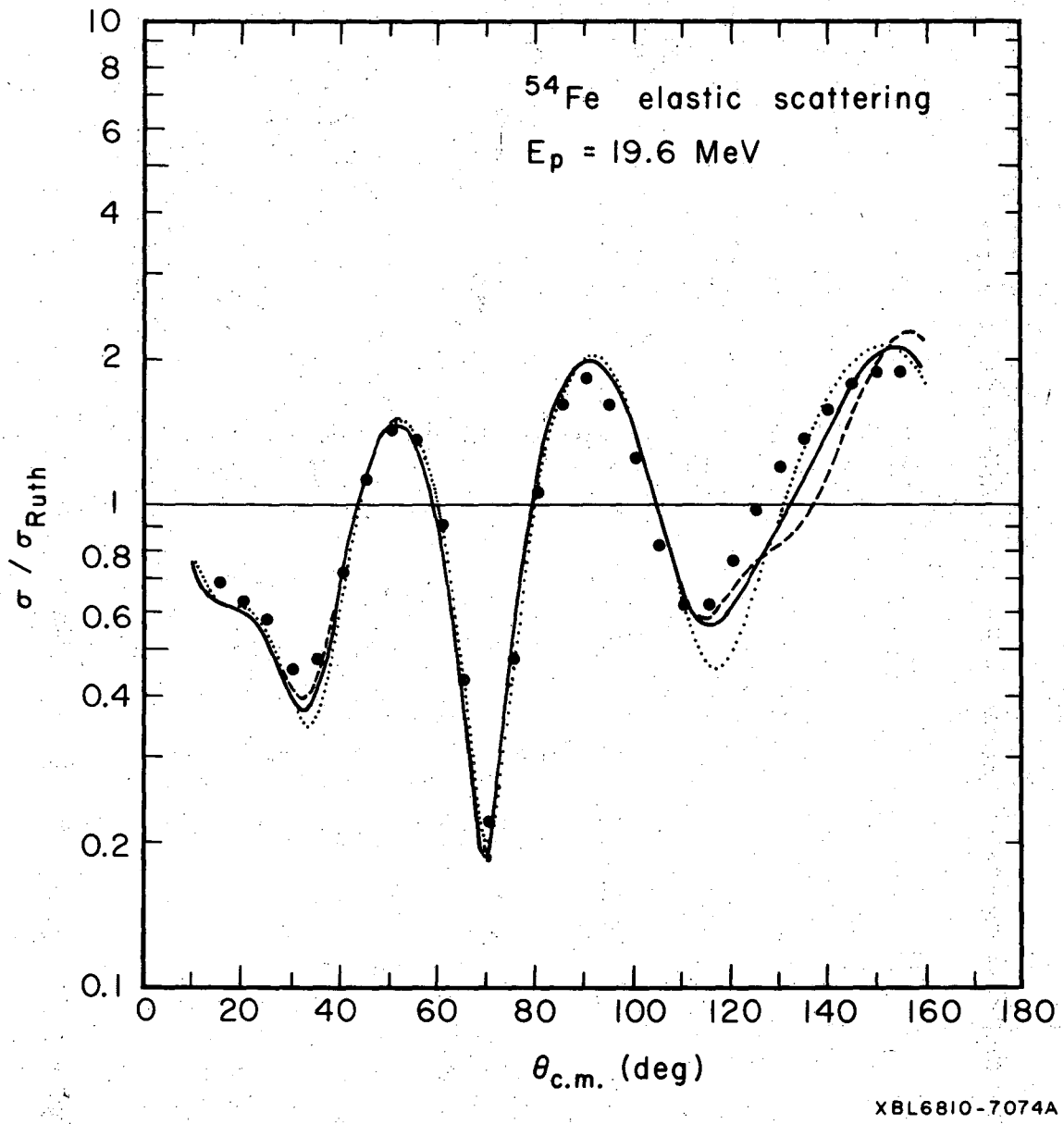

Fig. 54. The ratio of the elastic scattering cross section for ^{54}Fe to the Rutherford cross section. The solid curve is an optical-model fit using the best fit parameters of Table VII. The dotted and dashed curves are fits using the parameters of Table VIII, with V_{so} fixed at 4 MeV and 6 MeV, respectively.

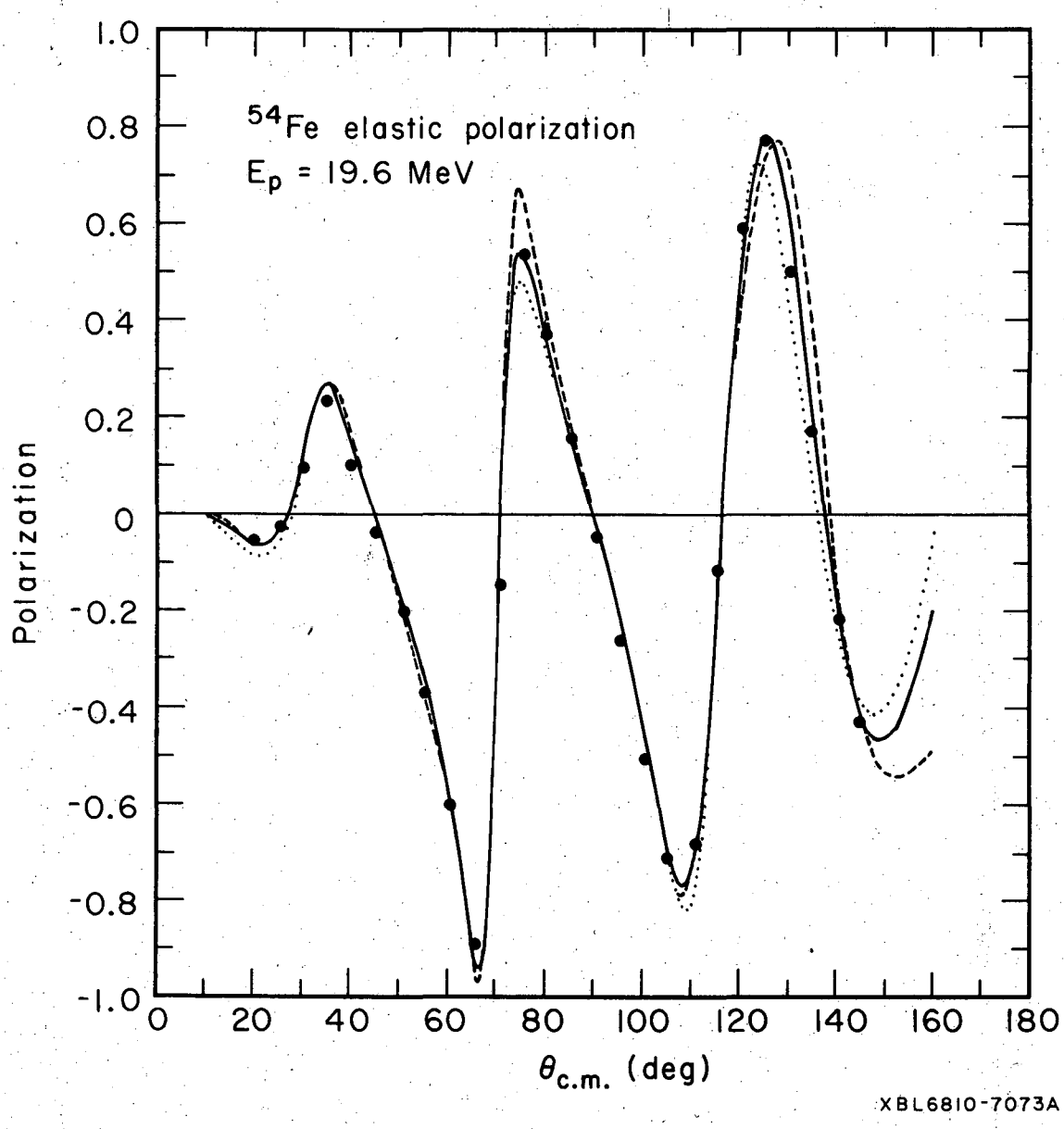

Fig. 55. The polarization in elastic scattering (Ref. 1) from ^{54}Fe. The curves are optical-model fits with the parameters of Tables VII and VIII. The curves are identified in Fig. 54.

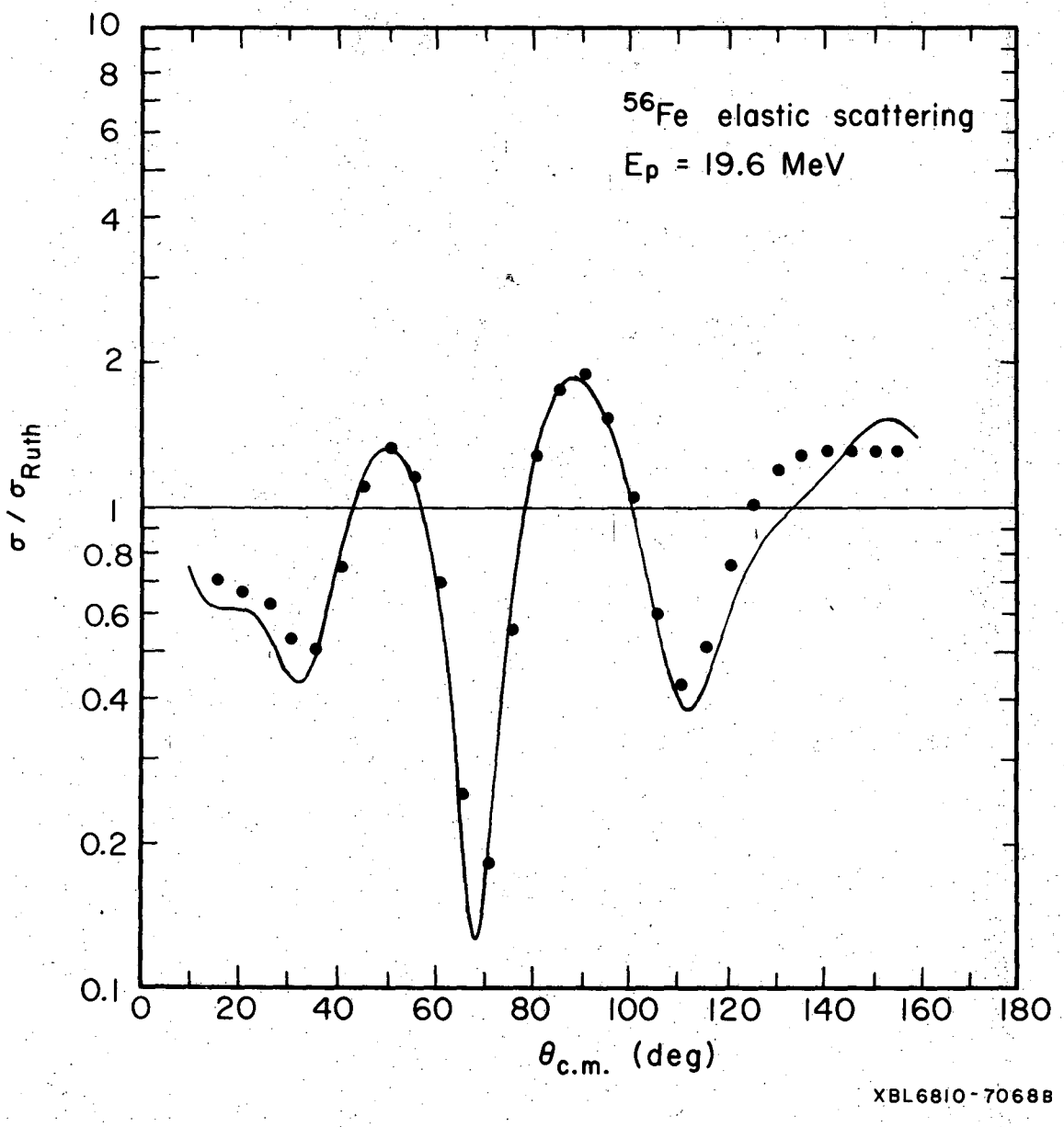

Fig. 56. The ratio of the elastic scattering cross section for ^{56}Fe to the Rutherford cross section. The curve is an optical-model fit with the parameters of Table VII.

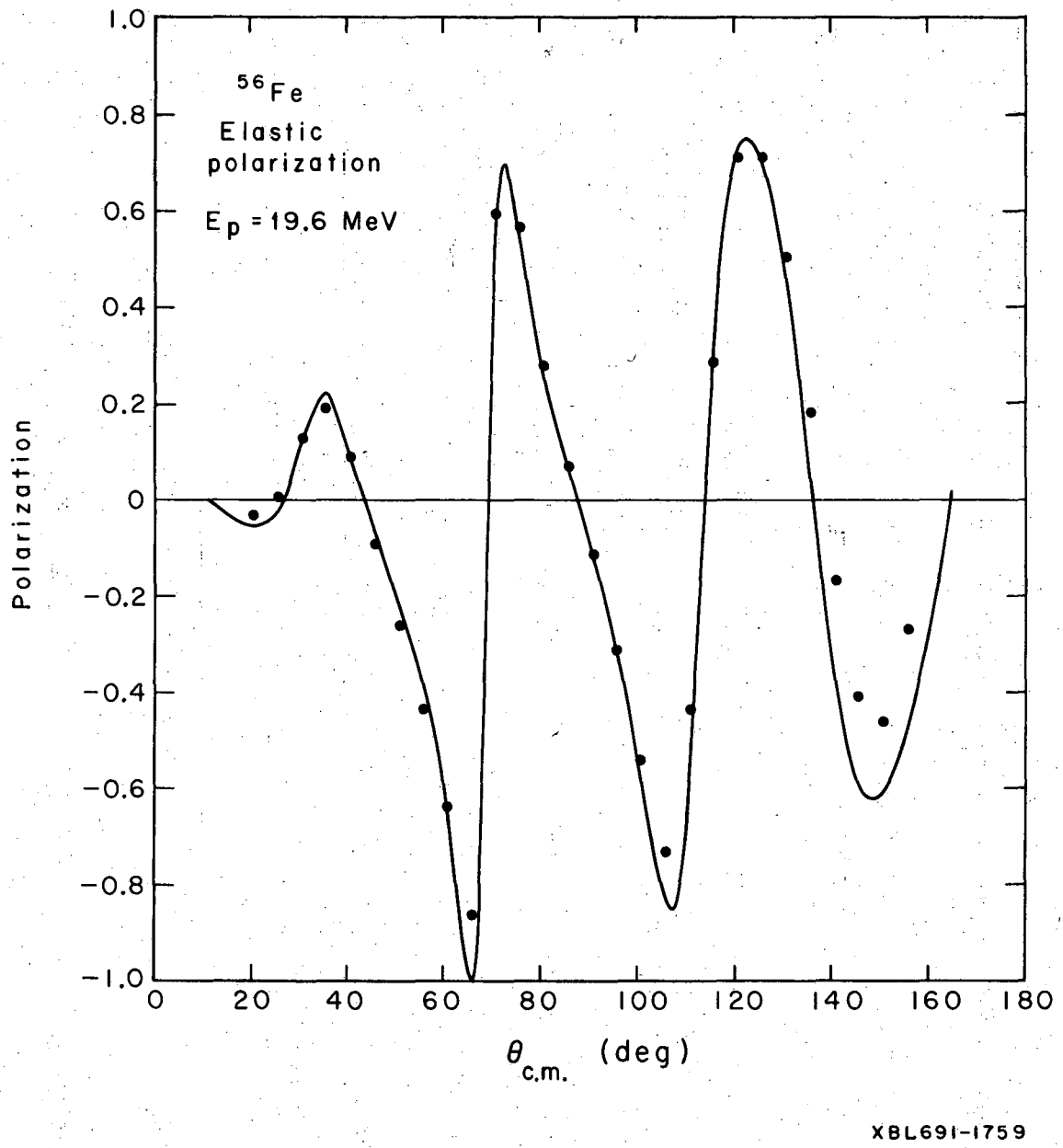

Fig. 57. The polarization in elastic scattering (Ref. 1) from ^{56}Fe. The curve is an optical-model fit with the parameters of Table VII.

As we have mentioned, the prediction of $S(\theta)$ in terms of a collective-model DWBA analysis is sensitive to the spin-orbit potential. To examine the extent to which these parameters are determined by the present analysis, we have fixed the well depth, V_{so}, for ^{54}Fe at 1 MeV on either side of the minimum and searched on all the other parameters. The parameters resulting from this procedure are given in Table VIII. The corresponding fits to the elastic data for the three spin-orbit well depths are shown in Figs. 54 and 55. The effect of such parameter adjustments on the predicted inelastic quantities will be discussed in the following section.

2. Collective Model

The collective model has long been used to interpret differential cross sections and polarizations for states assumed to be vibrational. The inelastic transition is considered to be caused by the deformation of the optical potential; deformations of both the real and imaginary potentials are included. It has also been found necessary, in the analysis of asymmetry data,[30,38] to include a deformed spin-orbit term in the interaction. The form of this term is not yet standard.[81]

The most extensive treatment of the spin-orbit deformation has been given by Sherif and Blair.[39] Starting with the Thomas form of the spin-orbit potential which can be derived from the impulse approximation, they show that the resulting deformed spin-orbit term can be written as follows:

Table VIII. Best fit parameters for ^{54}Fe with fixed V_{so}.

V (MeV)	W_D (MeV)	V_{so} (MeV)	r_r (F)	r_i (F)	r_s (F)	a_r (F)	a_i (F)	a_{so} (F)
49.89	8.83	4.00	1.19	1.34	1.06	0.73	0.50	0.22
50.51	7.94	5.06	1.19	1.31	1.075	0.70	0.55	0.40
48.82	8.04	6.00	1.22	1.30	1.13	0.66	0.54	0.45

$$U = U(1) + U(2)$$

where

$$U(1) = \left(\frac{h}{m_\pi c}\right)^2 V_{so}\, I(\theta,\phi)\, \frac{1}{r}\frac{\partial}{\partial r}\, \frac{\partial f}{\partial R_{so}}\, \underset{\sim}{\sigma}\cdot\underset{\sim}{\ell}$$

$$U(2) = \left(\frac{h}{m_\pi c}\right)^2 V_{so}\, \frac{\partial f}{\partial R_{so}}\, \underset{\sim}{\sigma}\cdot\left[\underset{\sim}{\nabla}\, I(\theta,\phi)\, \chi_i^{\frac{1}{}}\, \underset{\sim}{\nabla}\right].$$

R_{so} and $I(\theta,\phi)$ are parameters of the deformed spin-orbit potential:

$$R_{so}(\theta,\phi) = R_{so}^{o}\,(1 + I(\theta,\phi))$$

$$I(\theta,\phi) = \sum_{\lambda\mu} \alpha_{\lambda\mu}\, Y_{\lambda\mu}(\theta,\phi)$$

and

$$f = (1 + \exp(r - R_{so}/a_{so}))^{-1}.$$

The term U(2) contains non-radial components of the gradient operator and is quite complicated to evaluate. For this reason, earlier analyses[30,37] using a deformed spin-orbit potential neglected U(2). In the model of Sherif and Blair, the effects of both U(1) and U(2) are included; i.e., the full Thomas term is used.

For the analysis of the data, a computer program written by H. Sherif, which includes the effects of deformation of the entire optical potential, was used. For the spin-orbit deformation, options were available for using the full Thomas term (FT), U(1) deformation only U(1), or

a non-deformed spin-orbit potential (NDSO). Coulomb excitation was included in all calculations.

Figures 48 and 49 show the collective-model fits to $S(\theta)$ for the first 2^+ states of ^{54}Fe and ^{56}Fe, using the optical parameters in Table VII. For these data, no one of the three types of spin-orbit deformation is clearly preferred. For ^{54}Fe, all give a rather rough account of the data (i.e., they predict large $S(\theta)$ at back angles) but none fit well. There is some improvement in the predicted magnitude of the back-angle peak when one includes a deformed spin-orbit term. For ^{56}Fe the fit is somewhat better, particularly at back angles. For both nuclei, however, all predictions fail to account for an additional peak at 70°.

The fits to the asymmetries for these states are shown in Figs. 50 and 51. The fit to the ^{54}Fe data is poor; however, a substantial improvement is made by the inclusion of a deformed spin-orbit term, and even further improvement is obtained when the FT term is used. The three types of calculations for the ^{56}Fe asymmetry are nearly identical to those for ^{54}Fe. In this case, however, the measured asymmetries are smaller and the FT calculation produces a quite good fit. Similar results were obtained at 18.6 MeV[30] where the ^{54}Fe asymmetry was fitted poorly and the ^{56}Fe asymmetry was fitted rather well.

The fits to the differential cross sections are shown in Figs. 52 and 53. In general, these predictions show little sensitivity to the spin-orbit deformation. Again there is the problem of fitting experimental distributions which are rather different with theoretical curves which are quite similar. It is seen that the phase is predicted well but the decrease of the cross section with angle is fitted poorly in both cases.

In order to determine to what degree the collective-model predictions are made ambiguous by uncertainties in the spin-orbit potential, we show the inelastic predictions with the optical parameters of Table VIII in Figs. 58-60; these were calculated with the spin-orbit strength for ^{54}Fe fixed at 4, 5, and 6 MeV. The predicted $S(\theta)$ is very sensitive to V_{so}; this has been observed in previous work on ^{58}Ni.[36] The solution with V_{so} = 4 MeV agrees with the data at back angles but fails elsewhere. For the cross section and asymmetry predictions there is little difference among them.

The calculated values of $S(\theta)$ are less sensitive to the imaginary potential. Calculations for ^{54}Fe were performed with two sets of optical parameters with W_D fixed at 7 and 9 MeV, respectively. The chief difference between the two predictions is in the back angle maximum, which decreases from 0.36 to 0.32.

C. Microscopic Model

The simplified nucleon-nucleon interaction which has normally been used in microscopic-model calculations[40] includes a spin-dependent term which can induce transitions with $\Sigma = 1$. The interaction is written:

$$V(r_{ij}) = (-V_o \pm V_1 \sigma_i \cdot \sigma_j) \; g(|r_{ij}|).$$

In the present calculations, $g(|r_{ij}|)$ was assumed to be of Gaussian form with a range of 1.85 F. The sign and strength of V_1, in this effective interaction, are not well established. If it is large enough, and $\Sigma = 1$ transfer is important, the poor results of the collective-model treatment

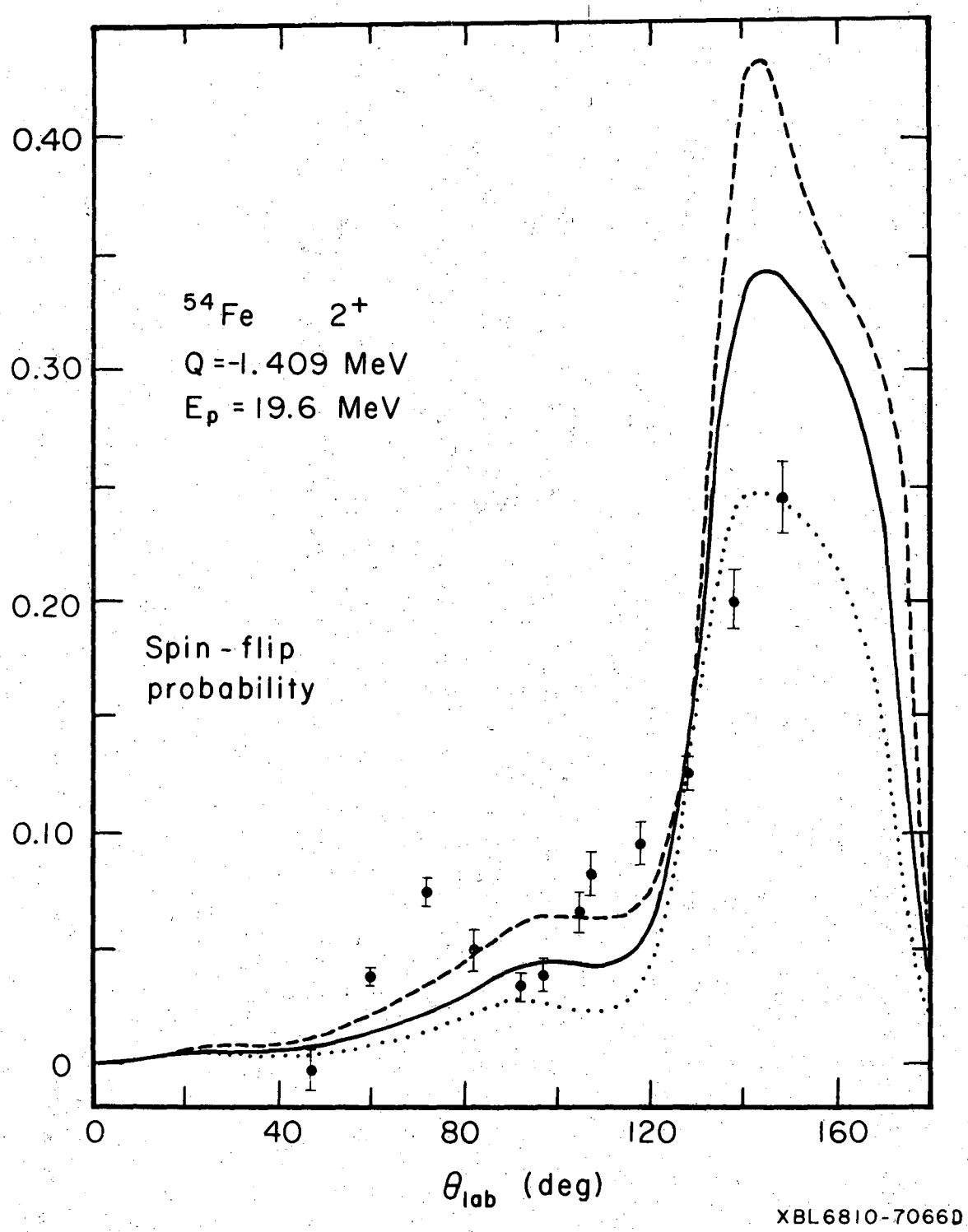

Fig. 58. Collective-model predictions of S(θ) with the optical parameters of Table VIII. These were obtained by fixing the spin-orbit well depth at 4 (dotted), 5 (solid), and 6 MeV (dashed).

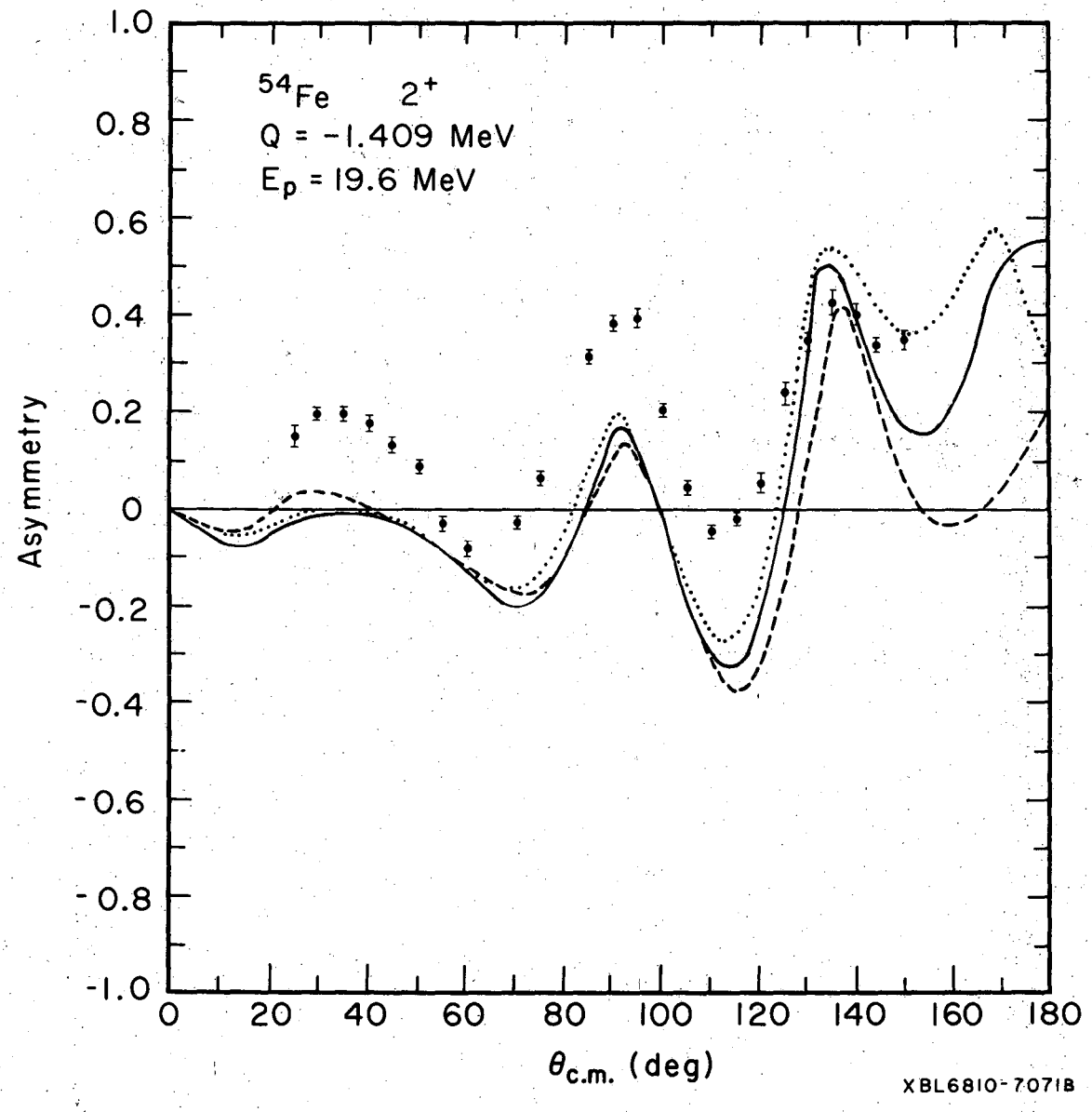

Fig. 59. Collective-model predictions of the asymmetry with the optical parameters of Table VIII. The curves are identified as in Fig. 58.

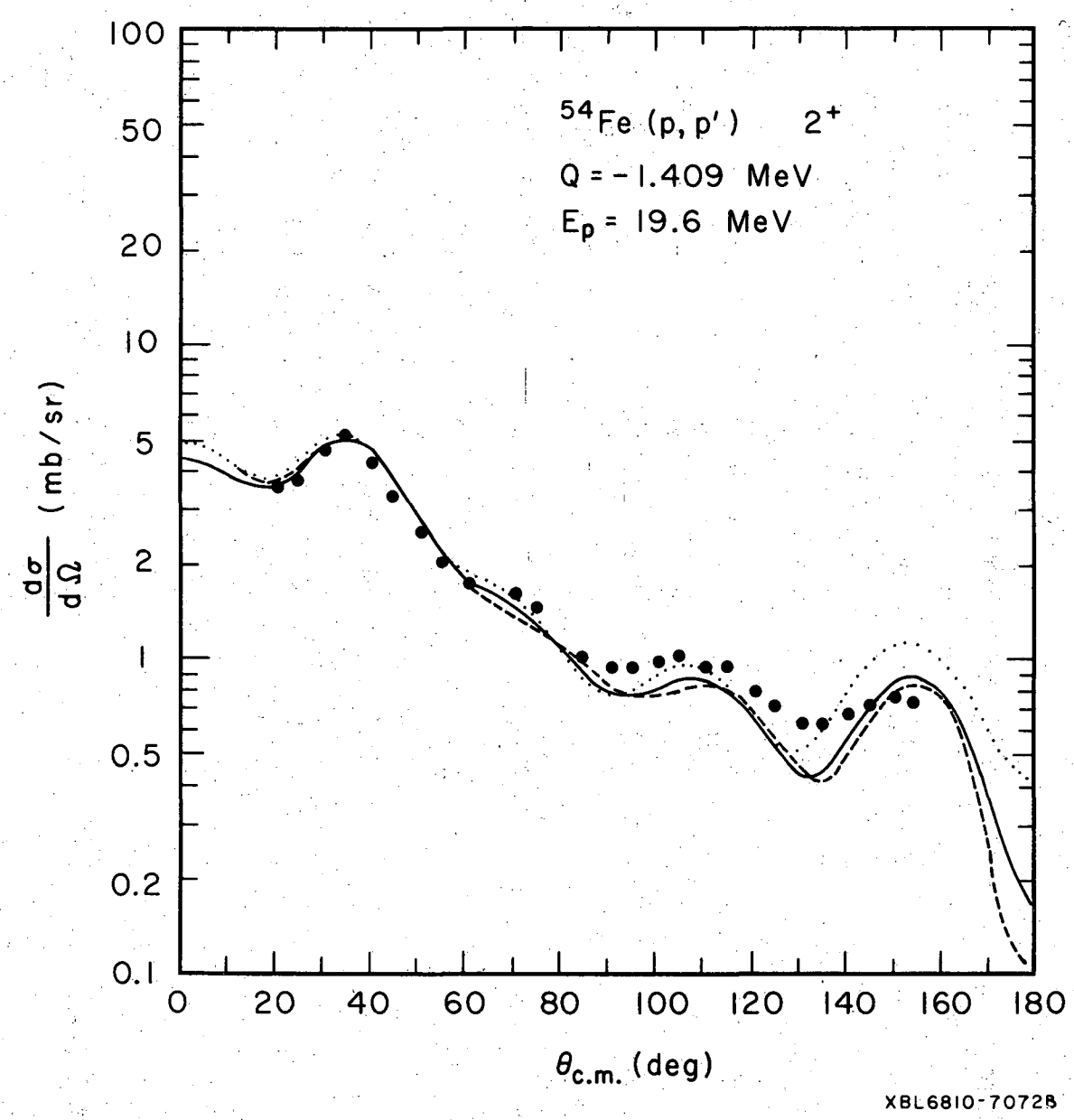

Fig. 60. Collective-model predictions of the differential cross section with the optical parameters of Table VIII. The curves are identified as in Fig. 58.

described above might be explained. If only $\Sigma = 0$ excitations are important, previous work indicates that this version of the microscopic model cannot explain the differences in asymmetries and cross sections for ^{54}Fe and ^{56}Fe. Because the wave functions of the two states are not known, however, only simple configurations were considered.[30]

The present microscopic analysis is hampered by the same difficulty. Since there are twenty-eight neutrons in ^{54}Fe, the predominant configuration of the first 2^+ state is presumably $(\pi f_{7/2})^{-2}_{2+}$; other configurations are sufficiently important, however, that the value[82] of BE2 is almost nine single-particle units. Since $\Sigma = 1$ transfer is forbidden in transitions which involve simply recoupling the angular momenta of two nucleons, contributions of $\Sigma = 1$ to the excitation of the 2^+ state in ^{54}Fe must come entirely from admixed configurations. These are probably many of the same configurations which predominate in the 2^+ state of ^{56}Fe. There the neutron shell is no longer closed, the energy of the first 2^+ state is lower, and B(E2) is about fourteen single-particle units.[82]

In order to estimate the possible effects of $\Sigma = 1$ transfer, calculations were first performed for simple particle transitions with V_o and V_1 both fixed at 65 MeV. They were carried out with the code of Glendenning; harmonic-oscillator wave functions were used for the bound state. Predictions of $S(\theta)$ for ^{54}Fe are shown in Fig. 61. The curve calculated for pure recoupling of $f_{7/2}$ particles resembles the collective-model fit. The other curves clearly show much larger probabilities at forward angles and vary markedly, depending on the configurations. It is

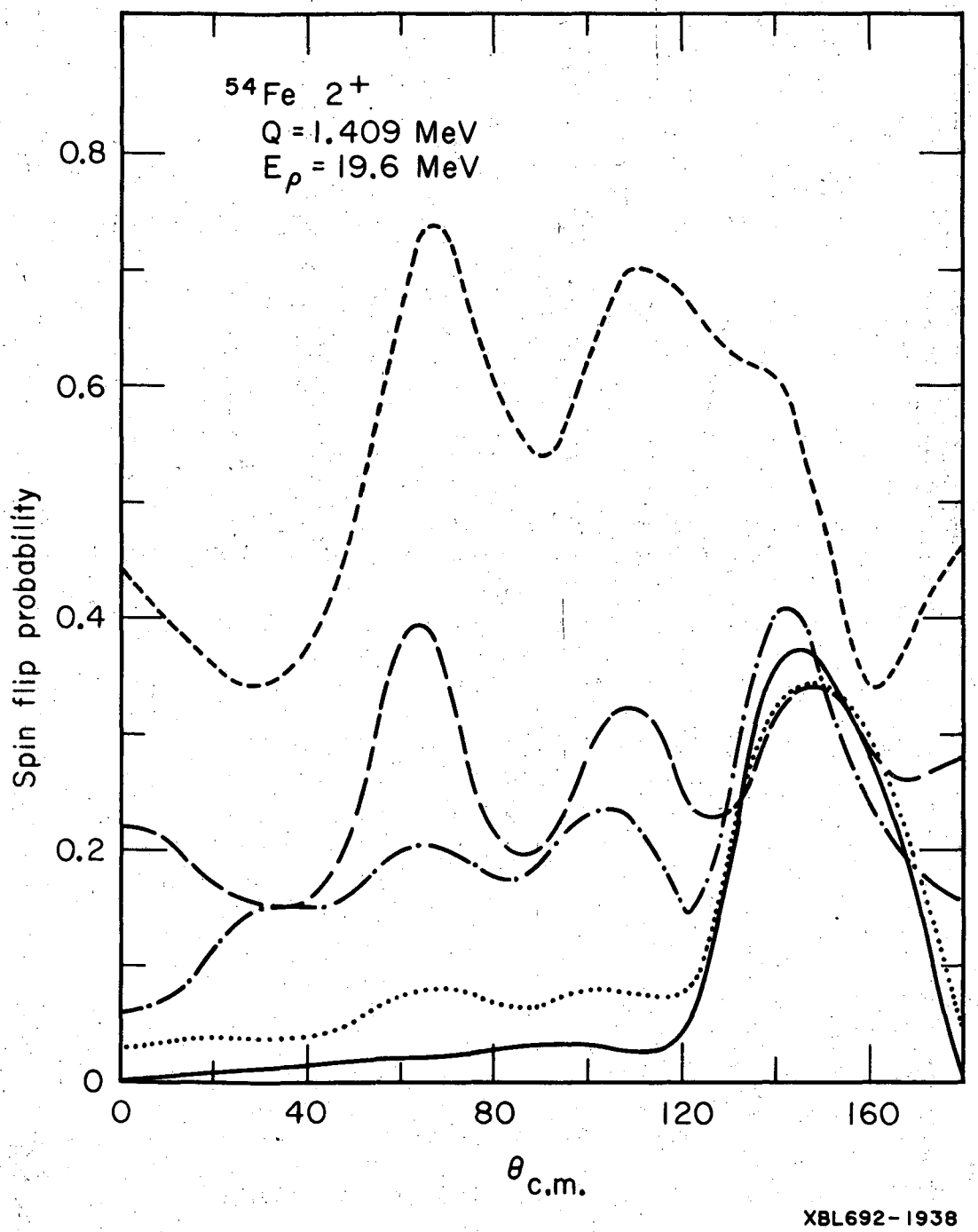

Fig. 61. Microscopic model predictions of S(θ) for ^{54}Fe. For all these curves, $V_o = V_1 = -65$ MeV. The ground state was assumed to be $(f_{7/2})^2_{0+}$. The 2^+ state was assumed to be: $(f_{7/2})^2_{2+}$ (——), $(f_{7/2},f_{5/2})_{2+}$ (-----), $(f_{7/2},p_{3/2})_{2+}$ (·····), $0.707\,(f_{7/2})^2_{2+}$ $-0.707\,(f_{7/2},p_{3/2})_{2+}$ (-·-·-).

interesting that peaks in $S(\theta)$ are generally predicted near 70° and 105°, the location of the small peaks in the measured $S(\theta)$. The predictions of the asymmetries and cross sections show a less marked, but still definite dependence on the configurations assumed and on the magnitude of V_1. Calculations of $S(\theta)$ for these same transitions with V_1 set to zero resemble the collective-model predictions and depend little on the configuration. In this case, the asymmetry and cross section are more configuration-dependent than $S(\theta)$.

Examples of calculations with V_1 set to the more typical value of 30 MeV are shown in Fig. 62. The 2^+ wave function here has been assumed to have components $0.707(f_{7/2})^2_{2+}$ and $0.707(f_{7/2},f_{5/2})_{2+}$. The ground state was pure $(f_{7/2})^2_{0+}$. Particle wave functions were used instead of hole wave functions for convenience. Calculations with admixtures of other configurations give similar results. The predicted values of $S(\theta)$ are now smaller at forward angles due to the reduction in strength of V_1. The four curves in Fig. 62 illustrate the effects of changing the relative sign of the two components of the wave function and the sign of V_1. The positive sign in the wave function increases the predicted value of $\sigma(\theta)$, i.e., this choice leads to collective enhancement. It corresponds to the two lower curves in Fig. 62. The smaller values of $S(\theta)$ reflect mainly the larger values of $\sigma(\theta)$, because most of the collective enhancement occurs in $\sigma_{++}(\theta)$ and $\sigma_{--}(\theta)$, the non-spin-flip terms. Although none of these choices provides a good fit to the asymmetry data, the choice of a positive V_1 and a positive relative sign in the wave function seems slightly favored. The cross section and asymmetry fits thus select the

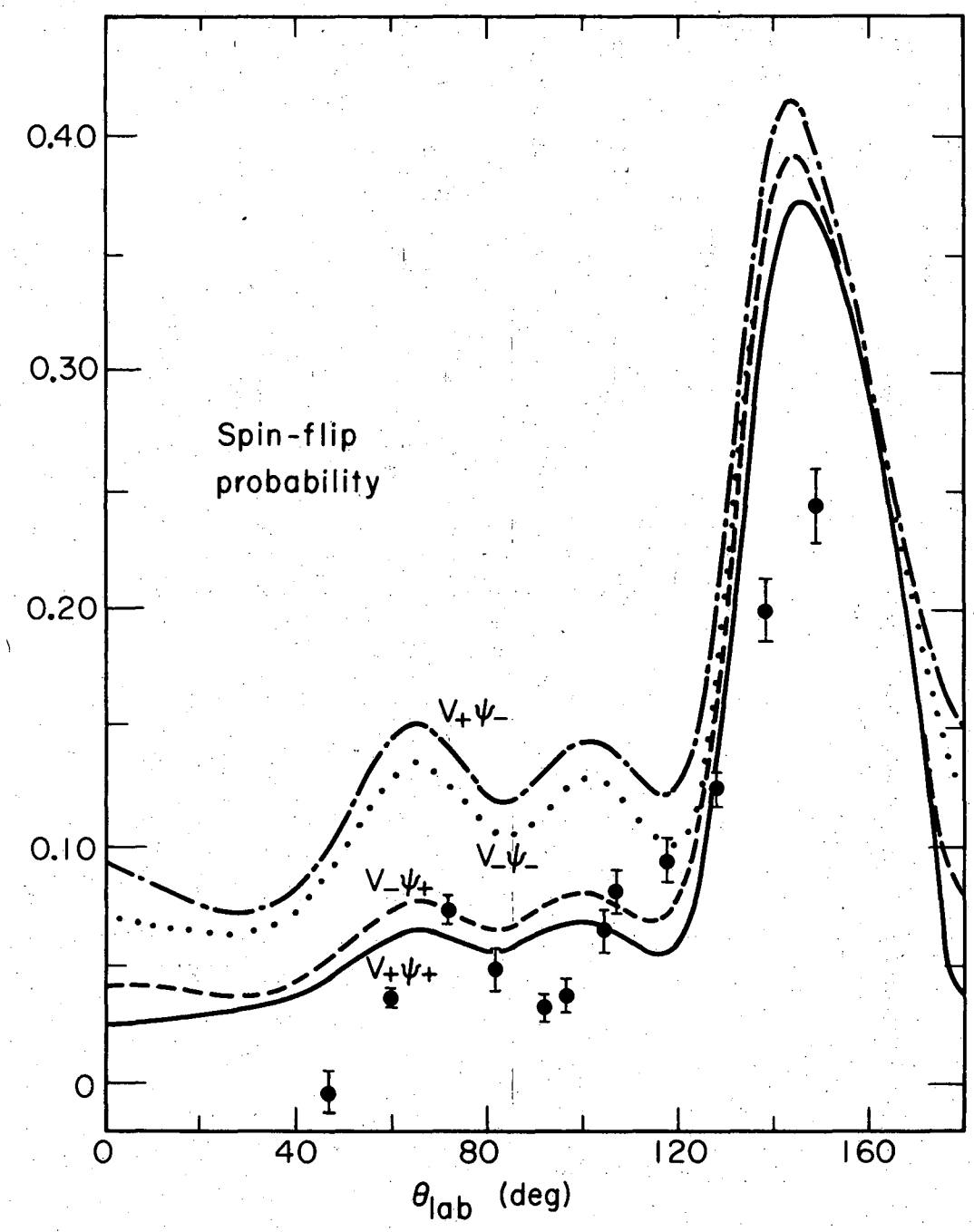

XBL 693-2296

Fig. 62. Microscopic model predictions of $S(\theta)$ for ^{54}Fe. For these curves, V_o is -65 MeV, V_1 is ± 30 MeV. The ground state was assumed to be $(f_{7/2})^2_{0+}$. The 2^+ state was assumed to be: $1/2(f_{7/2})^2_{2+} \pm 1/2(f_{7/2},f_{5/2})_{2+}$.

lowest $S(\theta)$ curve. Since realistic wave functions for ^{54}Fe are not available, it did not appear useful to attempt a detailed fit to the experimental $S(\theta)$ by adjusting parameters of the microscopic interaction. Nevertheless, Fig. 62 clearly shows the role of $\Sigma = 1$ terms in the forward-angle structure of $S(\theta)$.

The partial cross sections predicted with the above choice of signs are shown in Fig. 63. Inspection of this and several similar plots have led to several general conclusions. The fits to the experimental $\sigma(\theta)$, although slightly dependent on the details of the microscopic calculation, are not, in general, worse than those obtained with the collective model. The spin-flip cross section, not just the probability, is enhanced at back angles. Calculations which include only the $\Sigma = 0$ term reduce the spin-flip cross section at forward angles by a factor of 2 to 3, but leave the back-angle peak relatively unaffected. This peak disappears, however, when only $\Sigma = 1$ terms are included. The cross section is mostly due to the sum of $\sigma_{++}(\theta)$ and $\sigma_{--}(\theta)$ and the asymmetry is due mainly to the difference between these same two terms. Except for the back-angle peak where the spin-flip and non-spin-flip cross sections are of comparable magnitude, the spin-flip cross sections provide only minor modifications to $\sigma(\theta)$ and $A(\theta)$. Specifically, the inclusion of the $\Sigma = 1$ terms, although indicated by the small-angle spin-flip data, have no significant effect on $\sigma(\theta)$ and $A(\theta)$.

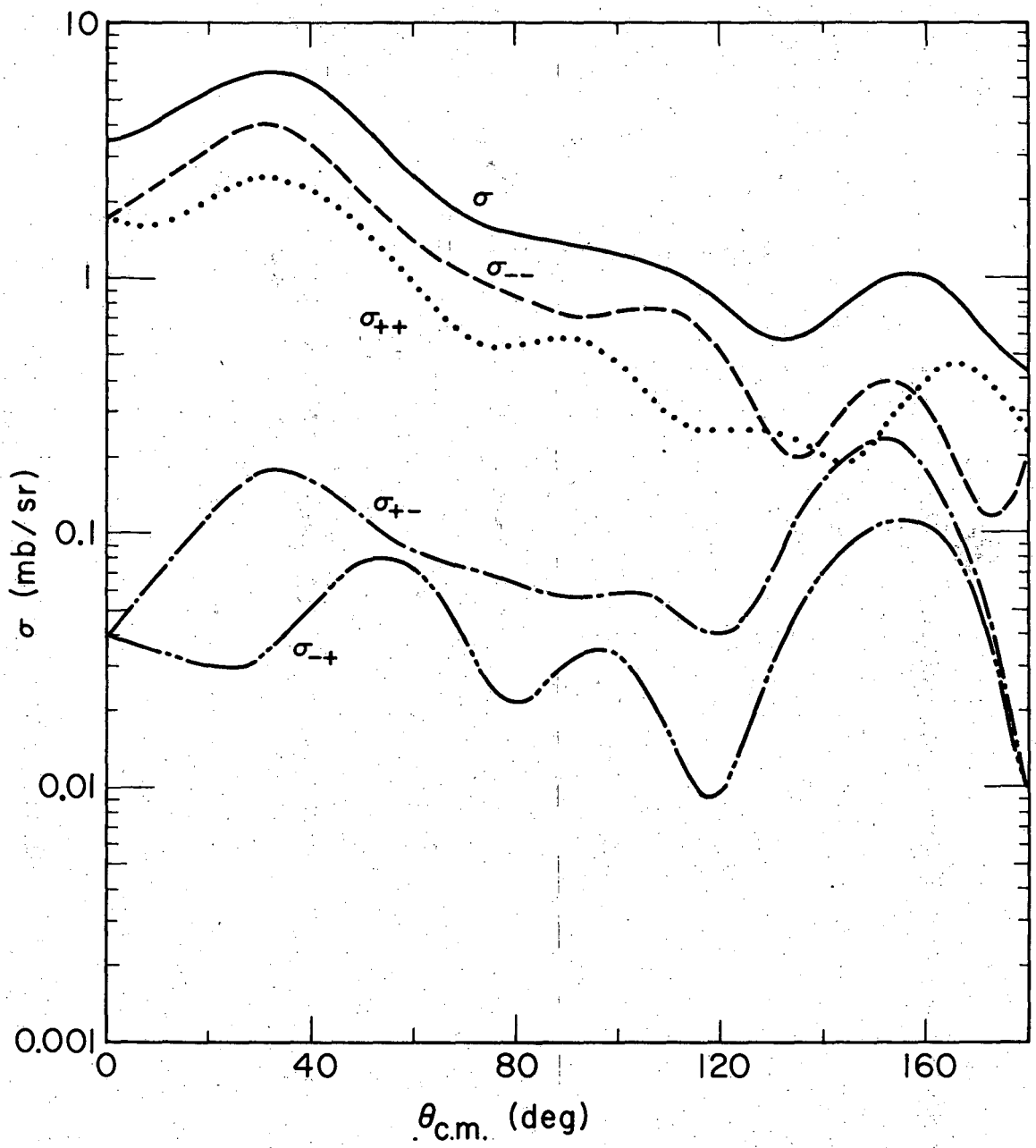

XBL693-2295

Fig. 63. Microscopic predictions of the partial cross sections for ^{54}Fe. For these calculations V_o is -65 MeV and V_1 is +30 MeV. The wave function is assumed to be: $1/2(f_{7/2})^2_{2+} + 1/2(f_{7/2}, f_{5/2})_{2+}$.

D. Summary

Spin-flip probabilities and cross sections for the excitation of the first 2^+ states in ^{54}Fe and ^{56}Fe have been measured for inelastic proton scattering at 19.6 MeV. These data and asymmetry data from Saclay have been analyzed with both macroscopic and microscopic DWBA models; neither gives a good account of all the data.

With the collective model, the fits to the differential cross sections are reasonably good; however, the slopes of the curves are different for the two states and these are not reproduced. The differences between the magnitudes of the asymmetries likewise are not reproduced. These failures are not surprising in view of the nature of the collective model. Differences would have to arise from very different optical parameters for the two nuclei, and there is no evidence for this in the present analysis. Other analyses[36,76] have shown that the back angle peak in the spin-flip probability for ^{58}Ni could be reproduced rather well by collective-model DWBA predictions with or without a deformed spin-orbit term. We also find this to be true; however, the ^{54}Fe back-angle peak it fitted less well than in the other nuclei. In addition, the structure of $S(\theta)$ is more complex than predicted by the collective analysis.

Since accurate wave functions for the two nuclei were not available, the microscopic analysis could only indicate the results which might be expected from a more complete calculation. If the admixtures of configurations other than $(f_{7/2})^{-2}_{+2}$ are significantly large, the calculations indicate that $S(\theta)$ at forward angles can be fit with a reasonable choice of V_1. The ratio of V_1/V_o must be proportionately larger than about 0.5

to have a significant effect of the predicted $S(\theta)$ if, as expected, the $(f_{7/2})^{-2}_{2+}$ configuration has a probability larger than about 0.5, which it had in our sample case. The shape of $S(\theta)$ depends only slightly on the particular configuration admixtures and on their relative phases when the $(\pi f_{7/2})^{-2}_{2+}$ configuration is predominant. However, if other configurations dominate, as would be expected for 2^+ states other than the lowest, and if V_1/V_o is large enough, then entirely different $S(\theta)$ patterns are predicted. The shapes, then, depend sensitivity on the relative amplitudes and phases of different configurations.

It remains puzzling that the spin-flip probabilities for ^{54}Fe and ^{56}Fe are quite similar, while the asymmetries and cross sections are different. Whatever reaction mechanism or coherence property of the wave functions is responsible for these differences must not affect $S(\theta)$. This might be possible if, for example, the spherical spin-orbit potential alone could account for the measured $S(\theta)$, but this is not indicated by our analysis. It is also possible, of course, that contributions due to nucleon-nucleon tensor and spin-orbit forces could bring about the required differences. Since these forces again affect mostly the σ_{+-} and σ_{-+} terms, our results suggest that they alone would not resolve the puzzle. Calculations which incorporate these forces, and which include space-exchange terms as well, have recently become possible.[83] A comparison of the predictions of such a code with the present results should prove interesting.

Acknowledgments

I take great pleasure in thanking:

Dr. Bernard Harvey and Dr. David Hendrie for the very able guidance of my research program, for numerous informative conversations and suggestions, and for emcouragement and assistance in many phases of my work as a graduate student.

My colleagues Dr. Heinz Brunnader, Dr. Mary Reed, Dr. Gordon Ball, Dr. Nolan Mangelson, Dr. Chi Chang Lu, Mr. Creve Maples, Mr. Joseph Sherman, Mr. John Esterl, and Mr. Richard Sextro for many interesting and informative conversations--both technical and non-technical.

My office mates, Mr. George Goth, Mr. Michael Zisman, and Mr. Gordon Wozniak for providing an inspriational atmosphere in which to work, and for an endless supply of useful suggestions and comments on all aspects of graduate student life.

Dr. Charles Glashausser and Dr. Jacques Thirion for participation in the experiments and for continued interest in my thesis work. Additionally, I want to thank these colleagues for suggesting one of the experiments and for many useful conversations regarding both experiments which comprise this thesis.

Mr. John Meneghetti, Mr. Don Fong, Mr. Don Stiver, Mr. Wayne Olthoff, and other members of the machine shop for their very fine work in constructing and repairing equipment involved in these experiments.

Mr. Roy Burton and Mr. Thomas Chan for designing the scattering chamber and for other help.

Dr. Richard Pehl and Mr. Robert Lothrop for providing the excellent detectors used in this work.

Mr. Don Landis and Dr. Fred Goulding for their excellent advice and assistance concerning the electronic equipment used.

Mr. John Bowen and the crew of the 88-inch cyclotron for very capably providing the necessary beams.

Dr. Alan Poletti and Dr. John Becker for providing computer programs and for several informative conversations, and Dr. E. K. Warburton for the use of a computer program.

Prof. Joe Cerny for suggestions and assistance regarding the completion of this work.

My wife Linda for very capably typing and punctuating the rough draft of this thesis and thus giving form to a mass of sloppy hand-written pages.

Finally I want to thank all of my family--Linda and my sons Eric and David for enduring with remarkably good humor the less than ideal life of a graduate student's family.

APPENDICES

Appendix A

1. General

With the formal and mathematical developments of recent years, it is now possible to derive expressions for angular correlations of considerable complexity (for excellent reviews of the subject, see Refs. 84 and 85). The most important tools are: Racah algebra, the density matrix formalism. and the group properties of the rotation matrices. The first two are used in the present development. No attempt is made to give a general derivation of the correlation function in terms of the detected protons and gamma rays; we view the problem simply as the gamma decay of an ensemble of aligned nuclei. Simple and physically rather obvious arguments are given to specify the original alignment.

It is possible within the density matrix formalism to include the effect of counter efficiencies and solid angles as efficiency matrices;[84,86] however, in the present derivation, the correlation function is first derived without reference to detection. Then solid-angle efficiency factors are included, following the derivation of Rose[87] (in Appendix B). It should be emphasized that no new methods are presented; the present derivation is included primarily to give insight into the application of this particular technique.

The notation used is that of Ferguson[86]--small letters refer to angular momenta and the corresponding Greek letters, to their projections on the z-axis.

2. Density Matrix Formalism

Consider a state $|a\alpha\rangle$ which is expanded in terms of eigenstates:

$$|n\rangle = \sum_{\alpha} |a\alpha\rangle\langle a\alpha|n\rangle$$

The expectation value of an operator, F, is then:

$$\langle n|F|n\rangle = \sum_{\alpha\alpha'} \langle n|a\alpha'\rangle \langle \alpha'|F|\alpha\rangle\langle a\alpha|n\rangle$$

When considering a number of possible states, $|n\rangle$, it is necessary to average over the entire ensemble. Thus:

$$\overline{F} = \sum_{n\alpha\alpha'} \langle a\alpha'|F|a\alpha\rangle\langle a\alpha|n\rangle g_n\langle n|a\alpha'\rangle$$

where g_n is the appropriate weighing factor for state $|n\rangle$. With the definition of the density matrix element:

$$\langle a\alpha|\rho|a\alpha'\rangle = \sum_{n} \langle a\alpha|n\rangle\ g_n\langle n|a\alpha'\rangle \qquad \text{(A-1)}$$

we find that

$$\overline{F} = \sum_{\alpha\alpha'} \langle a\alpha|\rho|a\alpha'\rangle\langle a\alpha'|F|a\alpha\rangle = \mathrm{Tr}(\rho F)$$

Tr denotes the trace of the matrix ρF. The density matrix is normalized so that $\mathrm{Tr}\rho = 1$.

Equation (A-1) can be viewed as the matrix element of the density operator:

$$\rho = \sum_n |n\rangle\, g_n \langle n|$$

A diagonal matrix element of this operator $\langle a\alpha|\rho|a\alpha\rangle$ is, then, the probability of finding a state of spin a in the substate α. Thus the density matrix constitutes a convenient description of the nuclear alignment. In a system in which there is no alignment, the density matrix is diagonal with:

$$\langle a\alpha|\rho|a\alpha'\rangle = 1/\hat{a}^2\delta_{\alpha\alpha'} \qquad \text{(A-2)}$$

where $\hat{a}$ is equal to $(2a + 1)^{1/2}$.

If state $|n\rangle$ is subject to an interaction, H, the density operator for the final state is:

$$\rho_b = H|n\rangle\, g_n \langle n|H^+$$

In terms of the original density matrix, then

$$\langle b\beta\ell\lambda|\rho_b|b\beta'\ell\lambda'\rangle = \sum_{\alpha\alpha'} \langle b\beta\ell\lambda|H|a\alpha\rangle\langle a\alpha|\rho_a|a\alpha'\rangle\langle a\alpha'|H^+|b\beta'\ell\lambda'\rangle$$

The matrix element of H may be reduced by the Wigner-Ekhart Theorem into:

$$\langle b\beta\ell\lambda|H|a\alpha\rangle = (b\beta,\ell\lambda|a\alpha)\langle b\|\ell\|a\rangle$$

3. <u>Nuclear Alignment</u>

With the aid of the previous considerations, we can now derive the general form for the alignment expected for states excited by particles scattered along the z-axis (beam axis). The density matrix for the

intermediate state formed when the particle is in or near the nucleus is:[21]

$$\langle b\beta|\rho|b'\beta\rangle = \sum_{\alpha\sigma_1}(a\alpha,s_1\sigma_1|S_1\beta)^2(S_1\beta,\ell_1 o|b\beta)(S_1\beta\ell_1' o|b'\beta)$$

$$\langle a\alpha|\rho_a|a\alpha\rangle\langle s_1\sigma_1|\rho_s|s_1\sigma_1\rangle\langle \ell_1 o|\rho_\ell|\ell_1' o\rangle \qquad \text{(A-3)}$$

$$\langle S\ell_1\|H\|b\rangle^*\langle S_1\ell_1'\|H\|b'\rangle$$

We have used the channel spin coupling scheme in which the particle spin, s, is coupled to the nuclear spin, a, to form S, which is then coupled to l_1, l_1'. The spins a and s are unpolarized, so their respective density matrix elements are given by Eq. (A-2). The matrix elements of the incoming plane wave may be found from the Raleigh expansion:

$$|\underset{\sim}{k}\rangle = \sum_\ell \hat{\ell} j_\ell(kr) i^\ell |\ell o\rangle$$

Then, from (A-1)

$$\langle \ell_1 o|\rho_\ell|\ell_1' o\rangle = \hat{\ell}\hat{\ell}'$$

From Eq. (A-3), it is seen that the largest term for the sum is given by $\beta = \alpha + \sigma_1$.

The density matrix element for the final state can be written as:

$$\langle c\gamma_1 s_2\sigma_2\ell_2 o|\rho|c\gamma s_2\sigma_2\ell' o\rangle = \langle c\gamma|\rho_c|c\gamma\rangle\langle s_2\sigma_2|\rho_s|s_2\sigma_2\rangle\langle \ell_2 o|\rho_\ell|\ell_2' o\rangle$$

$$= \sum (S_2\beta_2,\ell_2 o|b\beta)(S_2'\beta,\ell_2' o|b'\beta)(c\gamma,s_2\sigma_2|S_2\beta) \qquad \text{(A-4)}$$

$$(c\gamma_1,s_2\sigma_2|S_2\beta)\langle b\beta|\rho_b|b'\beta\rangle\langle s_2\ell_2\|H\|b\rangle\langle s_2'\ell_2'\|H\|b'\rangle^*$$

The summation is carried over b, b', S_2, S_2' because, in general, there is no unique intermediate state (b). The assumed zero projection of the outgoing orbital angular momentum is of course justified only if the particle is emitted at 0° or 180°. It is evident from (A-4) that the maximum obtainable γ is given by:

$$\gamma_{max} = \max(\alpha + \sigma_1 + \sigma_2) = a + s_1 + s_2$$

Thus, in the present case for proton scattering on a spin zero target, the possible values of γ are 0, ±1. In addition, because there is symmetry about the z-axis, the residual nucleus is aligned but not polarized, therefore:

$$P(1) = P(-1)$$

where

$$P(\pm 1) = \langle c \pm 1|\rho_c|c \pm 1\rangle$$

This symmetry also implies that the final density matrix is diagonal; this is also seen from Eq. (A-4). Because the reduced matrix elements of (A-3) and (A-4) are not generally known, there remains an undetermined parameter in the alignment of the residual nuclei for the reaction under

consideration. The unknown is either P(±1) or P(0), the remaining one being determined by the normalization condition.

4. Angular Correlation Function

This section is devoted to the derivation of the angular distribution function for gamma rays emitted from nuclei with the alignment described in the previous section. It is, therefore, the angular correlation function for the reaction $(p,p'\gamma)$ with the geometry discussed previously.

Considering a state $|a\alpha\rangle$ initially aligned and subsequently decaying to state $|b\beta\rangle$ by emission of a gamma ray with momentum $\underset{\sim}{k}$ and polarization $\underset{\sim}{\sigma}$, we can write:

$$\langle b\beta k\sigma|\rho_b|b\beta k\sigma\rangle = \sum_{\alpha=0,\pm1} \langle b\beta k\sigma|H|a\alpha\rangle\langle a\alpha|\rho_a|a\alpha\rangle\langle a\alpha|H^+|b\beta k\sigma\rangle \tag{A-5}$$

The correlation function is then:

$$W = \sum_{\sigma\beta} \langle b\beta k\sigma|\rho|b\beta k\sigma\rangle \tag{A-5b}$$

In Eq. (A-5), the final density matrix is expressed in terms of the measured quantity $\underset{\sim}{k}$ ($\underset{\sim}{\sigma}$ is not measured in the present experiment); however, in order to relate W to nuclear information, namely the angular momentum change, ℓ, the following transformation is required:

$$\langle b\beta k\sigma|H|a\alpha\rangle = \sum_{\ell\Lambda} \langle k\sigma|\ell\Lambda\rangle\langle b\beta\ell\Lambda|H|a\alpha\rangle \tag{A-6}$$

It is convenient to relate the coefficients $\langle k\sigma|\ell\Lambda\rangle$ to those of a plane wave propagating along the z-axis. Thus:

$$\langle k\sigma|\ell\Lambda\rangle = \sum_{\lambda} \langle o\sigma|\ell\lambda\rangle D^{\ell}_{\Lambda\lambda}(\underset{\sim}{Z} \rightarrow \underset{\sim}{k}) \tag{A-7}$$

Substituting (A-7) into (A-6), and applying the Wigner-Ekhart Theorem, we get:

$$\langle b\beta k\sigma|H|a\alpha\rangle = \sum_{\ell\Lambda\lambda} (b\beta,\ell\Lambda|a\alpha)\langle o\sigma|\ell\lambda\rangle\langle b\|\ell\|a\rangle D^{\ell}_{\Lambda\lambda}(\underset{\sim}{Z} \rightarrow \underset{\sim}{k})$$

Now, with the substitution of this expression, we obtain for the correlation function:

$$W = \sum \langle a\alpha|\ell_a|a\alpha\rangle (b\beta,\ell\Lambda|a\alpha)(b\beta,\ell'\Lambda'|a\alpha)(\ell\lambda,\ell'\lambda'|k\tau)$$

$$(\ell\Lambda,\ell'\Lambda'|kN)\langle b\|\ell\|a\rangle\langle b\|\ell'\|a\rangle\langle o\sigma|\ell\lambda\rangle\langle o\sigma|\ell'\lambda'\rangle D^{k}_{\lambda N} \tag{A-8}$$

The summation is over α, σ, β, ℓ, ℓ', Λ, Λ', λ, λ', k, τ, N; the indices k, τ, N appear due to the application of the Clebsch-Gordan Series.[88]

The set of summation indices may be considerably reduced with the application of Racah algebra.[89] Equation (A-8) then becomes:

$$W = \sum_{\alpha,\ell,\ell',k} \hat{b}^2\, C_{ko}(\ell\ell')(a\alpha,a-\alpha|ko)(-)^{b+\alpha-\ell-k-2a} W(aa\ell\ell';kb)$$

$$\langle b\|\ell\|a\rangle\langle b\|\ell'\|a\rangle P_k(\cos\theta) \tag{A-9}$$

In order to obtain Eq. (A-9), two additional simplifications were required:

1) The coefficients C_{ko} depend only on the properties of the radiation field and are thus called radiation parameters. For gamma radiation, they are, in general:

$$C_{k\tau}(\ell\ell') = S \sum_{\lambda\lambda'} (-)^{\ell'-\lambda'} (\ell\lambda,\ell'\lambda'|k\tau)\langle o\sigma|\ell\lambda\rangle^{*}\langle o\sigma|\ell'\lambda'\rangle \qquad \text{(A-10)}$$

The coefficients $\langle o\sigma|\ell\lambda\rangle$ are obtained from consideration of the multipole expansion of the electro-magnetic field. Since the polarization of the gamma ray is not detected, Eq. (A-10) may be simplified to:

$$C_{ko}(\ell\ell') = \frac{\hat{\ell}\hat{\ell}}{8\pi}(-)^{\ell'-1}(\ell 1,\ell -1|ko)$$

This corresponds to the phase convention of Ferguson.[21,86]

2) The more general form of Eq. (A-9) contains a factor $(a\alpha,a-\alpha|kN)$; this is simplified, for this case, by the fact that the initial density matrix is diagonal. We also note the substitution:

$$D^{k}_{oo}(\underset{\sim}{Z} \rightarrow \underset{\sim}{k}) = P_k(\cos\theta)$$

Finally, Eq. (A-9) can be written in the form:

$$W = \sum_{\alpha k\ell\ell'} (-)^{b-\alpha} P(\alpha)(a\alpha,a-\alpha|ko)\delta^{r} Z_1(\ell a,\ell' a;bk)P_k(\cos\theta) \qquad \text{(A-11)}$$

where $\delta = \langle b\|\ell\|a\rangle / \langle b\|\ell_{min}\|a\rangle$ is the multipole mixing ratio for the transition, ℓ_{min} is the minimum possible multipole consistent with parity and angular momentum conservation, and $\ell = \ell_{min} + 1$. The quantity r is

0, 1, or 2, respectively, for $\ell\ell' = (\ell,\ell)$, (ℓ,ℓ'), and (ℓ',ℓ'); here it is assumed that a maximum of two multipoles contribute to the transition. The definition of Z_1 is:

$$Z_1(\ell a,\ \ell' a;bk) = (-)^{k-\ell+\ell'-1}\hat{\ell}\hat{\ell}'\hat{a}^2(\ell 1,\ell'-1|ko)W(\ell a,\ell' a;bk)$$

The Z_1 coefficients are tabulated in Ref. 86.

Another convenient formulation of angular correlation function has been given by Poletti and Warburton.[22] Using their definitions, Eq. (A-11) can be written as:

$$W = \sum_k \rho_k(a)\ F_k(ab)P_k(\cos\theta) \qquad \text{(A-12)}$$

where

$$\rho_k(a) = \sum_\alpha \rho_k(a,\alpha)P(\alpha)$$

and

$$F_k = \frac{F_k(\ell\ell ba)-(-)^\sigma 2\delta F_k(\ell\ell' ba)+\delta^2 F_k(\ell'\ell' ba)}{1+\delta^2}$$

The coefficients $\rho_k(a)$ and $F_k(ab)$ are tabulated in Ref. 22 and are defined

$$\rho_k(a) = (2-\delta_{\alpha o})\ \frac{(a\alpha,a-\alpha|ko)}{(a\alpha,a-\alpha|oo)}$$

$$F_k(\ell\ell' ba) = (-)^{b-a-1}[\hat{\ell}\hat{\ell}'\hat{a}](\ell 1,\ell'-1|ko)W(aa\ell\ell';kb)$$

With the choice $\sigma = 0$ for an ML, EL + 1 mixture and $\sigma = 1$ for an EL, ML + 1 mixture, the mixing ratio, δ, is identical to that of Eq. (A-11). In the present work, we have taken $\sigma = 0$ for all cases. With the above definitions, the k = 0 term of Eq. (A-12) is unity.

A further case of interest is that of transition $a \xrightarrow{\gamma_1} b \xrightarrow{\gamma_2} c$, in which γ_1 is not observed. The density matrix of state b must then be determined in order to determine the correlation function for γ_2. The derivation is not given here; we quote only the result. W now is given by:

$$W(\theta_{\gamma_2}) = \sum_k \rho_k(a)\, U_k(ab) F_k(bc) P_k(\cos\theta_{\gamma_2}) \qquad \text{(A-13)}$$

where

$$U_k(ab) = (U_k(\ell ab) + \delta_1^2 U_k(\ell' ab))/(1+\delta_1^2)$$

The coefficients $U_k(ab)$ are tabulated in Ref. 22.

Appendix B

The angular correlation function derived in Appendix A is of the form $W(\theta') = \sum_k A_k P_k(\cos\theta')$. The measured experimental quantity is:[87]

$$\overline{W}(\theta) = \int d\Omega_\gamma d\Omega_p W(\theta')\varepsilon_\gamma \varepsilon_p \qquad \text{(B-1)}$$

The integral is computed over the solid angles of the counters, $\Omega_{\gamma,p}$ where $\Omega_{\gamma,p}$ are referred to the axes of symmetry of the counters. The ε's are the counter efficiencies as a function of angle.

With the substitution of the explicity form of $W(\theta')$, the integrals to be evaluated are of the form:

$$I = \int d\Omega_\gamma d\Omega_p \varepsilon_\gamma \varepsilon_p P_k(\cos\theta') \qquad \text{(B-2)}$$

The evaluation is accomplished by applying the spherical harmonic addition theorem to the spherical triangles $(\theta',\phi,\beta_\gamma)$ and (ϕ,θ,β_p), illustrated in Fig. 64. Because both detectors are spherically symmetric, the general form of the theorem

$$P_k(\cos\theta') = (4\pi/2\ell+1) \sum_{-k}^{k} Y_k^{m*}(\beta_\gamma) Y_k^m(\phi)$$

can be reduced to:

$$P_k(\cos\theta') = P_k(\cos\beta_\gamma) P_k(\cos\phi)$$

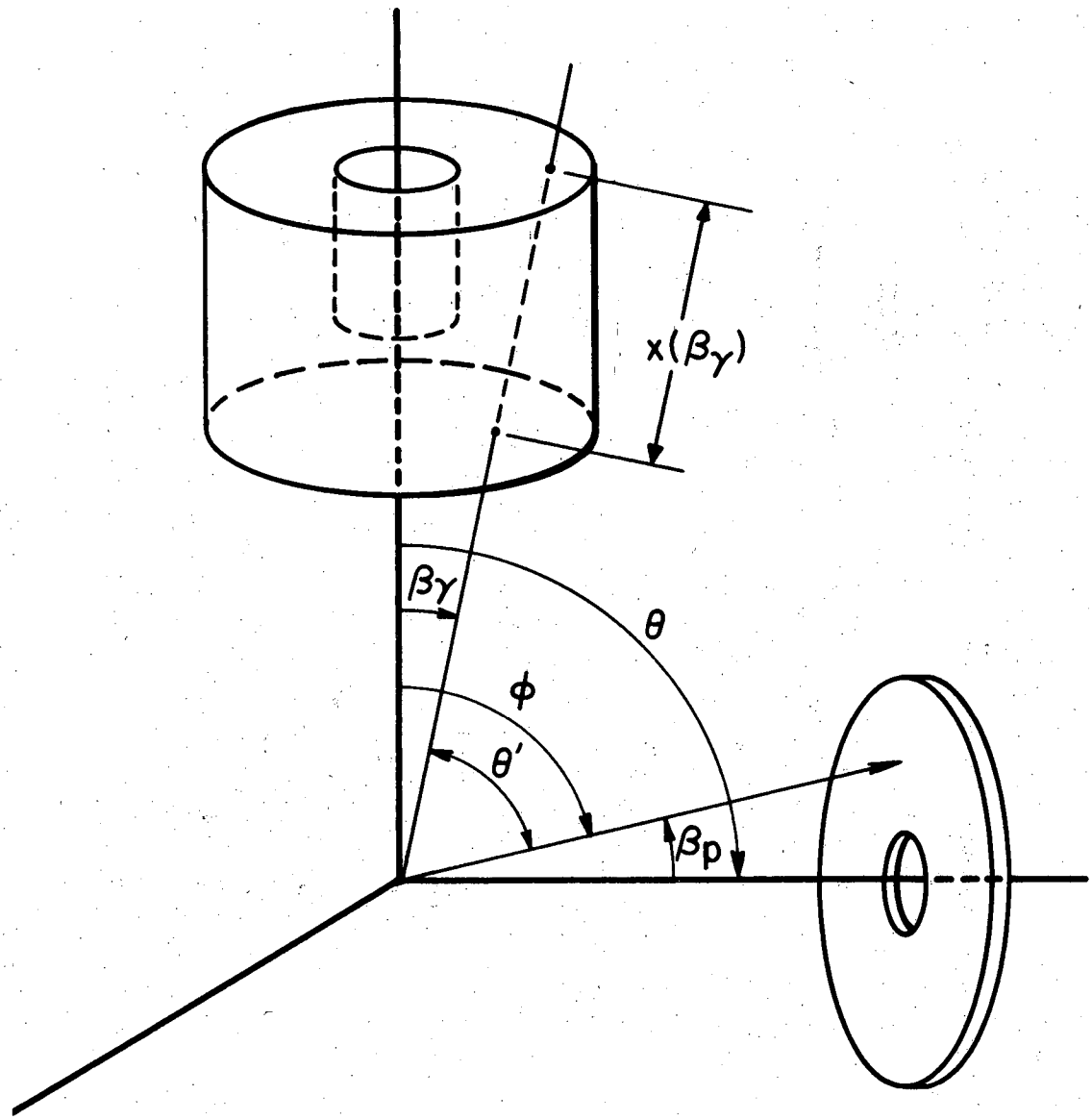

XBL693-2232

Fig. 64. Geometry used for the evaluation of the attenuation coefficients of Table IX.

Now, applying the theorem to (ϕ,θ,β_p), we obtain:

$$P_k(\cos\theta') = P_k(\cos\theta)P_k(\cos\beta_\gamma)P_k(\cos\beta_p)$$

Substitution of this expression into (B-2) yields:

$$I = 4\pi^2 P_k(\cos\theta)J_k(\gamma)J_k(P)$$

where

$$J_k = \int_{\beta_{min}}^{\beta_{max}} P_k(\cos\beta)\varepsilon(\beta)\sin\beta d\beta \qquad \text{(B-3)}$$

For the particle detector, ε_p is constant over the entire acceptance angle. For the gamma detector, we have assumed the form:

$$\varepsilon_\gamma(\beta) = 1-e^{-\tau x(\beta)}$$

where τ is the total absorption coefficient for gamma rays of a given energy in germanium, $x(\beta)$ is the path length illustrated in Fig. 64. The integrals of Eq. (B-3) have been evaluated for the geometries of the present experiment for several gamma-ray energies and are listed in Table IX. The coefficients given are of the form $Q_k = J_k/J_o$. The theoretical correlation function, to be fitted to the experimental data, then has the form:

$$W(\theta') = \sum_k A_k Q_k P_k(\cos\theta')$$

With the definition of $W(\theta')$ given in Eq. (A-12) (Appendix A), the $k = 0$ term is unity.

Table IX. Attenuation coefficients for the 40 cm^3 coaxial Ge(Li) detector. Detector to source distance = 9.6 cm^3.

Gamma energy (keV)	Absorption coefficient	Q_2	Q_4
100	2.98	0.9796	0.9332
150	1.34	0.9807	0.9365
200	0.893	0.9813	0.9387
300	0.605	0.9820	0.9409
400	0.498	0.9823	0.9418
500	0.438	0.9825	0.9425
600	0.397	0.9826	0.9429
800	0.342	0.9828	0.9435
1000	0.305	0.9830	0.9439
1500	0.248	0.9832	0.9446
2000	0.218	0.9833	0.9450
3000	0.188	0.9834	0.9454

FOOTNOTES AND REFERENCES

1. B. Mayer and J. Thirion (C.E.N., Saclay, France) private communication.

2. The term "alignment" refers to cases in which there is equal population of the magnetic substates -m and m. When this criterion is not met, the ensemble is said to be polarized.

3. J. D. McCullen, F. B. Bayman, and L. Zamick, Phys. Rev. 134, B515 (1964).

4. George F. Bertsch, Nucl. Phys. 89, 673 (1966).

5. W. J. Gerace and A. M. Green, Nucl. Phys. A93, 110 (1967).

6. P. Federman, Phys. Letters 20, 174 (1966).

7. B. H. Flowers and L. D. Skouras, Nucl. Phys. A116, 529 (1968).

8. W. J. Kossler, J. Winkler, and C. D. Kavaloski, Phys. Rev. 177, 1725 (1969), and references contained therein.

9. J. C. Bane, J. J. Kraushaar, B. W. Ridley, and M. M. Stautberg, Nucl. Phys. A116, 580 (1968).

10. R. R. Hartmann, K. P. Lieb, and H. Röpke, Nucl. Phys. A123, 437 (1969).

11. H. O. Funsten, N. R. Roberson, and E. Rost, Phys. Rev. 134, B117 (1964).

12. T. Stovall and N. M. Hintz, Phys. Rev. 135, B330 (1964).

13. W. S. Gray, R. A. Kenefick, and J. J. Kraushaar, Nucl. Phys. 67, 565 (1965).

14. S. F. Eccles, H. F. Lutz, and V. A. Madsen, Phys. Rev. 141, 1067 (1966).

15. R. J. Peterson, Ph.D. Thesis, University of Washington, 1966 (unpublished).

16. M. F. Thomas, A. R. Poletti, and M. A. Grace, Nucl. Phys. 78, 561 (1966).

17. The reduction from nine to five unknown substate populations occurs because of the alignment condition. One other parameter may be eliminated because the normalization of the measured angular correlation is arbitrary.

18. R. M. Diamond, E. Matthias, J. O. Newton, and F. S. Stephens, Phys. Rev. Letters 16, 1205 (1966).

19. J. G. Cramer and W. W. Eidson, Nucl. Phys. 55, 593 (1964).

20. J. M. Lacambra, D. R. Tilley, and N. R. Roberson, Nucl. Phys. A92, 30 (1967).

21. A. E. Litherland and A. J. Ferguson, Can. J. Phys. 39, 788 (1961).

22. A. R. Poletti and E. K. Warburton, Phys. Rev. 137B, 595 (1965).

23. For aligned nuclei ($P_m = P_{-m}$) the index k takes on even integer values from 0 to 2a, where a is the spin of the initial state. In practice, it is not usually possible to experimentally measure any terms with $k > 4$.

24. E. K. Warburton, D. E. Alburger, and D. H. Wilkinson, Phys. Rev. 129, 2180 (1963).

25. A. E. Blaugrund, Nucl. Phys. 88, 501 (1966).

26. R. E. Pixley and W. Beneson, Nucl. Phys. A91, 177 (1967).

27. P. Paul, J. B. Thomas, and S. S. Hanna, Phys. Rev. 147, 774 (1966).

28. J. Lindhard, M. Scharff, and H. E. Schiøtt, Kgl. Danske Videnskab. Selskab, Mat.-Fys. Medd. 33, No. 14 (1963).

29. The definitions of polarization and asymmetry may be more clearly understood by considering the way in which they are measured. To determine the asymmetry in inelastic scattering one measures the difference in intensity between the left and right scattering of an initially polarized beam. The same quantity is obtained using one detector by measuring the difference in intensity between the scattering of positive and negatively polarized beams. Polarization is measured by determining the polarization of the outgoing particles after scattering of an initially unpolarized beam.

30. C. Glashausser, R. de Swiniarski, J. Thirion, and A. D. Hill, Phys. Rev. 164, 1437 (1967).

31. A. G. Blair, C. Glashausser, J. Goudergues, R. M. Lombard, B. Mayer, R. de Swiniarski, J. Thirion, and P. Vagonov, Proc. Int. Nucl. Phys. Conference, Tokyo, 1967; A. G. Blair, C. Glashausser, J. Goudergues, R. M. Lombard, B. Mayer, R. de Swiniarski, and J. Thirion, Phys. Rev. (to be published).

32. R. Ballini, N. Cindro, J. Delaunay, J. Fouan, M. Loret, and J. P. Passerieux, Nucl. Phys. A97, 561 (1967).

33. F. G. Perey, Proceedings of the Second International Symposium on Polarization Phenomena of Nucleons, Karlsruhe, 1965, ed. by P. Huber and H. Schopper, (Birkhäuser Verlag, Bassel, 1966), p. 200.

34. F. H. Schmidt, Ronald E. Brown, J. B. Gerhart, and Wojiech A. Kolasinski, Nucl. Phys. 52, 353 (1964).

35. W. A. Kolasinski, Ph.D. Thesis, University of Washington, (1967), (unpublished); W. A. Kolasinski, J. Eenmaa, F. H. Schmidt, H. Sherif, and J. R. Tesmer, (to be published).

36. J. Eenmaa, F. H. Schmidt, and J. R. Tesmer, (to be published).

37. A. Bohr, Nucl. Phys. 10, 486 (1959).

38. M. P. Fricke, E. E. Gros, and A. Zucker, Phys. Rev. 163, 1153 (1967).

39. H. Sherif and J. S. Blair, Phys. Letters 26B, 489 (1968); H. Sherif, Ph.D. Thesis, University of Washington, 1967 (unpublished).

40. N. K. Glendenning and M. Veneroni, Phys. Rev. 144, 839 (1966); G. R. Satchler, Nucl. Phys. 77, 481 (1966).

41. It is important to be able to reach small angles because the Legendre polynomials have their maxima at 0°.

42. The distance chosen was a compromise between high detection efficiency and the elimination of the simple alignment condition. For discussions of the importance of each, see Sections III.B-2 and IV.C-1.

43. F. S. Goulding, Nucl. Instr. Methods 43, 1 (1966).

44. R. H. Pehl, private communication.

45. Sources obtained from the International Atomic Energy Agency.

46. F. S. Goulding, D. A. Landis, and R. H. Pehl, University of California Lawrence Radiation Laboratory Report UCRL-17560, (unpublished).

47. Modification was done by D. A. Landis.

48. L. B. Robinson, F. Gin, and F. S. Goulding, Nucl. Instr. Methods 62, 237 (1968).

49. R. E. Hintz, F. B. Selph, W. S. Flood, B. G. Harvey, F. G. Resmini, and E. A. McClatchie, University of California Lawrence Radiation Laboratory Report UCRL-18383 , (unpublished).

50. D. L. Hendrie, Ph.D. Thesis, University of Washington, 1964, (unpublished).

51. D. M. Drake, Ph.D. Thesis, University of Washington, 1962, (unpublished).

52. F. H. Schmidt, H. Fauska, and J. W. Orth, Nuclear Electronics III (IAEA, Vienna, 1962), p. 381.

53. R. L. Graham, I. K. McKenzie, and G. T. Ewan, IEEE Trans. Nucl. Sci. 13, No. 1, 72 (1966); G. T. Ewan, R. L. Graham, and I. K. McKenzie, IEEE Trans. Nucl. Sci. 13, No. 3, 297 (1966).

54. M. G. Strauss, R. N. Larsen, and L. L. Siften, Nucl. Instr. Methods 46, 45 (1967).

55. J. P. Fouan and J. P. Passerieux, Nucl. Instr. Methods 62, 327 (1968).

56. J. M. Jaklevic, F. M. Bernthal, J. O. Radeloff, and D. A. Landis, Nucl. Instr. Methods (to be published).

57. D. J. Church, R. N. Horoshko, and G. E. Mitchell, Phys. Rev. 160, 894 (1967).

58. G. J. Nijgh, A. H. Wapstra, and R. van Lieshout, Nuclear Spectroscopy Tables, (North-Holland Publishing Company, Amsterdam, 1959).

59. L. C. Northcliffe, Ann. Rev. Nucl. Sci. 13, 67 (1963).

60. M. A. Eswaren, H. E. Gove, A. E. Litherland, and C. Broude, Nucl. Phys. 66, 401 (1965).

61. Palmer G. Steward and Roger Wallace, University of California Lawrence Radiation Laboratory Report UCRL-17314, (unpublished).

62. A. Aspinall, G. Brown, and S. E. Warren, Nucl. Phys. 46, 33 (1963).

63. A. Sperduto and W. W. Buechner, Phys. Rev. 134B, 142 (1964).

64. O. Hansen, T. A. Belote, and W. E. Dorenbusch, Nucl. Phys. A118, 41 (1968).

65. Dietrich Wegener, Z. Physik 198, 251 (1967).

66. D. H. Wilkinson, Nuclear Spectroscopy Part B, ed. by Fay Ajzenberg-Selove, (Academic Press Inc., New York, 1960), p. 852.

67. J. J. Simpson, J. A. Cookson, D. Eccleshall, and M. J. L. Yates, Nucl. Phys. 62, 385 (1965).

68. J. Bellicard and P. Barreau, Nucl. Phys. 36, 476 (1962).

69. D. C. Sutton, H. A. Hill, and R. Sherr, Bull. Am. Phys. Soc. 4, 278 (1959).

70. T. A. Belote, W. E. Dorenbusch, and O. Hansen, Nuclear Spin-Parity Assignments, ed. by N. B. Gove (Academic Press, Inc., New York, 1966), p. 350.

71. The definition of δ in Ref. 16 is opposite to that used here.

72. C. F. Perdrisat, Rev. Mod. Phys. 38, 41 (1966).

73. R. W. Benjamin and I. L. Morgan, Phys. Rev. 163, 1252 (1967).

74. This is the apparent Doppler shift due to recoils which escape the target.

75. Aron M. Bernstein, Advances in Nuclear Physics, Vol. III, ed. by M. Baranger and E. Vogt, (to be published).

76. R. O. Ginaven, E. E. Gross, J. J. Malanify, and A. Zucker, Phys. Rev. Letters 21, 552 (1968).

77. M. A. Melkanoff, J. Raynal, and T. Sawada, UCLA Report No. 66-10, January 1966, (unpublished).

78. P. Kossanyi-Demay, R. de Swiniarski, and C. Glashausser, Nucl. Phys. A94, 513 (1967); P. Kossanyi-Demay and R. de Swiniarski, Nucl. Phys. A108, 577 (1967).

79. G. R. Satchler, Nucl. Phys. A92, 273 (1967).

80. D. J. Baugh, J. A. R. Griffith, and S. Roman, Nucl. Phys. 83, 481 (1966).

81. C. Glashausser and J. Thirion, Advances in Nuclear Physics, Vol. II, ed. by M. Baranger and E. Vogt, (Plenum Press, New York, 1969), p. 79.

82. P. H. Stelson and L. Grodzins, Nuclear Data Tables, Vol. IA, p. 21.

83. J. Hocquengham, private communication.

84. S. Devons and L. J. B. Goldfarb, Handbuch der Physik, Vol. 42, ed. by S. Flügge (Springer-Verlag, Berlin, 1957), p. 362.

85. H. Frauenfelder and R. M. Steffen, Alpha-, Beta-, and Gamma-Ray Spectroscopy, Vol. 2, ed. by Kai Siegbahn, (North-Holland Publishing Co., Amsterdam, 1965), p. 997.

86. A. J. Ferguson, Angular Correlation Methods in Gamma-Ray Spectroscopy, (North-Holland Publishing Co., Amsterdam, 1965).

87. M. E. Rose, Phys. Rev. 91, 610 (1953).

88. M. E. Rose, Elementary Theory of Angular Momentum, (John Wiley and Sons, Inc., New York, 1957) p. 57.

89. This step is similar to that taken in Ref. 83, p. 383.

LEGAL NOTICE

This report was prepared as an account of Government sponsored work. Neither the United States, nor the Commission, nor any person acting on behalf of the Commission:

A. Makes any warranty or representation, expressed or implied, with respect to the accuracy, completeness, or usefulness of the information contained in this report, or that the use of any information, apparatus, method, or process disclosed in this report may not infringe privately owned rights; or

B. Assumes any liabilities with respect to the use of, or for damages resulting from the use of any information, apparatus, method, or process disclosed in this report.

As used in the above, "person acting on behalf of the Commission" includes any employee or contractor of the Commission, or employee of such contractor, to the extent that such employee or contractor of the Commission, or employee of such contractor prepares, disseminates, or provides access to, any information pursuant to his employment or contract with the Commission, or his employment with such contractor.

TECHNICAL INFORMATION DIVISION
LAWRENCE RADIATION LABORATORY
UNIVERSITY OF CALIFORNIA
BERKELEY, CALIFORNIA 94720